# NOTE TO USERS

# Evaluation of CadPlan for electron beam treatment planning

**Deborah Hodefi**

**Medical Physics Unit, McGill University, Montreal**

**February 2004**

A thesis submitted to McGill University in partial fulfillment of the requirements of the degree of M.Sc.

*Your file Votre référence*
*ISBN: 0-612-98658-6*
*Our file Notre référence*
*ISBN: 0-612-98658-6*

**Abstract**

The electron pencil beam algorithm particular to the CadPlan treatment planning system (Varian) was evaluated for energies and field sizes spanning the clinical range. Calculated distributions were compared to measured data from an Elekta SL 25 linear accelerator. Excellent accordance was achieved between measured and calculated distributions for all energies and field sizes in cases of a uniform medium with a flat surface, perpendicular beam incidence and the standard source to surface distance (SSD) of 100 cm. CadPlan was also proficient at producing accurate distributions involving varied SSDs within the range typically employed in the clinic, 98-102 cm. However, when beam incidence was non-orthogonal to the surface, calculated distributions differed from measurement by up to 2.5 mm or 7 %. The most severe discrepancies were observed for larger gantry angles. Calculated percent depth dose (PDD) curves in cases of simple slab heterogeneities were found to deviate from measured curves by at most 1.5 mm. Discontinuities appeared in all CadPlan-predicted curves, worsening in instances of non-standard conditions. Many errors stemming from such discontinuity problems could be eliminated by interpolating between values of fitting parameters tabulated in CadPlan and by offering more pencil beam and calculation grid sizes. As CadPlan has no means of accounting for scattered radiation specific to the jaws and applicator, it is unable to predict output factors with any accuracy.

**Résumé**

L'algorithme de planification de traitement CadPlan (Varian) pour des faisceaux d'électrons était évalué à travers la gamme clinique des énergies et des tailles du champ. Les distributions de dose calculées par l'algorithme étaient comparées avec celles qui étaient mesurées à partir des faisceaux provenant d'un accélérateur linéaire de modèle Elekta SL 25. Un accord très satisfaisant était noté pour toutes énergies et tailles de champ en cas d'un milieu uniforme à surface plate, à la distance source-surface (DSS) typique de 100 cm, et en instance d'incidence perpendiculaire du faisceau. De plus, CadPlan, était également compétent en calculant des distributions de dose pour des cas caractérisés par des DSS entre 98 et 102 cm. Cependant, quand l'angle du statif était différent de zéro, impliquant une incidence de faisceau non perpendiculaire, les distributions calculées affichaient des désaccords avec les plans mesurés jusqu'à 2.5 mm ou 7 %. Ces pires divergences se manifestaient pour les angles du statifs les plus larges. Les rendements en profondeur particuliers aux cas incluant des simples hétérogénéités montraient un désaccord maximum de 1.5 mm entre les courbes mesurées et celles qui étaient calculées par CadPlan. Globalement, chaque courbe prédite par CadPlan affichait des discontinuités, les plus graves en cas caractérisés par des conditions non standards. Plusieurs écarts ayant ces discontinuités comme l'origine peuvent être fort probablement éliminées en interpolant entre les valeurs tabulées des paramètres utilisées par l'algorithme dans ses calculs. De plus, un choix plus vaste de tailles des pinceaux et des tailles des matrices de calcul est une manière possible de diminuer les écarts. Comme CadPlan n'a aucun moyen de tenir compte de la radiation diffusée provenant des mâchoires et de l'applicateur, l'algorithme est incapable de prédire les facteurs relatifs avec une précision tolérable dans la clinique.

**Acknowledgements**

First and foremost, I would like to express my sincerest gratitude to my supervisor, Dr. Noël Blais, for his teachings and moreover, for being so phenomenally generous with his time. Next, I would like to thank Dr. Ervin Podgorsak, Director of the Medical Physics Unit at the McGill University Health Centre, for allowing me to perform the research for this project at Hôpital Maisonneuve-Rosemont (HMR). Of course, I would also like to express much thankfulness and appreciation to Dr. Wieslaw Wierzbicki for so warmly welcoming me into the Physics department at HMR. Carrying out my research project in the midst of a real clinical environment was incredibly instructive and this experience would have not nearly been so valuable and enjoyable without the help and encouragement of the rest Physics team at HMR: Maryse Mondat, Patrice Munger, Richard Plourde, Étienne Roussin, Marie-Laure Camborde and Marylène Brodeur. They always took the time to share their vast knowledge and kindly answer all of my questions. I would also like to extend many thanks to Jean-René Tremblay, machinist, Simon Goulet, electronics, and Louis Surprenant, mould room technician, for taking time out of their busy schedules to generously provide me with pieces and insight that very much aided me. The entire staff of the Radiation Oncology department at HMR has been nothing but welcoming and supportive throughout my time at HMR and for this I express heartfelt thanks. I also owe much gratitude to the Quebec government for providing me with a much appreciated bursary as well as an agreement of employment in conjunction with the HMR Human Resources department to whose members I am also very thankful. Finally, I would like to thank my friends, Aolani Harrison, who provided much entertainment via the telephone during long, overnight measuring sessions and Matthew McEvoy, with whom I had many helpful discussions concerning this work.

TABLE OF CONTENTS

## Introduction

Electron beams are a commonly employed cancer treatment modality. Nevertheless, electron beam algorithms are still not as developed as their photon counterparts and still do not constitute an integral part of clinical treatment planning. The CadPlan treatment planning system, produced by Varian, is widely used for its photon planning capabilities. This work aims to evaluate its electron pencil beam algorithm in order to determine if it is fit for routine clinical use.

The first chapter introduces the clinical electron beam; how it is produced as well as its clinically relevant features. The first section of the chapter is comprised of fairly detailed descriptions of the main components of the linear accelerator: the electron gun, the microwave RF power system, the accelerating waveguide, the bending magnets, the scattering foils and finally beam collimation devices. In this work, electron beams were produced by the Elekta SL 25 accelerator, therefore some descriptions concentrate on the particulars of this type of machine. The second section of Chapter 1 focuses on the physical characteristics of the electron beam. A comprehensive description of the electron beam percent depth dose (PDD) curve is provided. Furthermore, Chapter 1 relates how electron beam PDD curves vary with all pertinent parameters: energy, field size, source to surface distance (SSD), and angle of beam incidence. Isodose distributions, penumbra and electron beam uniformity are also discussed.

Chapter 2 is dedicated to the basic theory required to understand the behaviour of electron beams in a medium. Firstly, the ways in which a single incident electron may interact with an absorber atom are reviewed, classified in terms of the incoming electron's distance from the nucleus. Next, the chapter discusses multiple scattering theory, which leads to the concept of scattering power. While scattering power deals with how electrons are scattered over a given thickness of medium, stopping power expresses electron energy loss over some thickness. This latter parameter is subject of the next section of the chapter. Finally, Chapter 2 concludes with a description of Fermi-Eyges theory, essentially a solution of the Boltzmann transport equation for electron pencil beams, and the cornerstone of electron pencil beam algorithms.

The third chapter in this work relates how the CadPlan electron beam algorithm functions to predict dose distributions. More specifically, Chapter 3 centres about the CadPlan formula used to calculate dose to a point, explaining the significance of each parameter. The computer implementation of the algorithm is also described.

Experimental methods are the subject of Chapter 4. Numerous measurements were required in order to investigate the efficacy of CadPlan electron beam treatment planning. The outset of this chapter is devoted to instrumentation, while the second section reports the methods used in this work to convert ionization data to dose data. The third section describes each set of measurements performed in a water tank: measurements to reveal which detector type would be most suitable to the demands of this work, measurements designed to verify CadPlan's aptitude at calculating dose distributions in a homogeneous phantom, measurement of the virtual source distance and measurement of output factors. Measurements executed in a solid, epoxy-based tissue substitute constitute the topic the following section. These included measurements involving simple heterogeneities as well as build-up region measurements. The next section of Chapter 4 explains how CadPlan was configured to simulate beams like those created by the linear accelerator used in this work. The chapter wraps up with a discussion of acceptance criteria and evaluation methods.

The process of selecting an apposite detector to execute the many measurements required to evaluate CadPlan electron beam planning is the subject of Chapter 5. Two air ionization chambers, a thimble chamber and a parallel-plate chamber, as well as a p-type silicon diode constituted the candidate detectors. The chapter commences by providing the characteristics of each detector, highlighting their respective strengths and weaknesses. The second section of the chapter reports the results of the central axis PDD curve and profile measurements performed. The conclusion of the chapter summarizes the rationale for choosing the thimble chamber to perform the necessary measurements.

Chapter 6 relates the results of all experiments carried out and accordingly discusses and assesses CadPlan's aptitude for electron beam treatment planning. It begins by presenting the values selected for each input parameter set by the user. The

ramifications caused by variation of each of these parameters on a given CadPlan-calculated distribution were observed. The following three sections of the chapter report results defining CadPlan's ability to predict dose distributions in a homogeneous medium, in cases of varied beam energy, field size, SSD and angle of beam incidence. Next, results portraying CadPlan's capacity to predict central axis PDD curves in the presence of simple slab inhomogeneities are discussed. CadPlan-predicted output factors for cases of homogeneous media are presented in the succeeding section and compared to measured data. After that, CadPlan electron beam planning is evaluated in terms of a real clinical case.

Chapter 7 concludes this work with a summary of the results and discussion presented for each set of data, suggests possible improvements to the CadPlan algorithm and makes an overall pronouncement on the accuracy and utility of CadPlan electron beam treatment planning in the clinic.

# Chapter 1

## Electron Beams

With the advent of the linear accelerator and thus the clinical introduction to high energy beams, modern radiotherapy has advanced into a highly specialized modality. Photon beams (orthovoltage x-rays and Cobalt-60 beams) constituted traditional treatment options. Scientific and technological advancements in the high energy domain not only allowed for more efficient photon therapy for deep-seated tumours, but paved the way for an exciting new clinical modality: electron beams. This chapter relates how electron beams in the radiation therapy range are produced and then goes on to discuss electron beam characteristics and their clinical impact.

### 1.1 Production of High Energy Electron Beams: The Linear Accelerator

High energy electron beams designated for therapeutic purposes are created by a linear accelerator (linac). Essentially, an electron gun injects electrons into a waveguide, where the electrons' kinetic energy is greatly increased with the aid of power furnished by a microwave power source, either a klystron or a magnetron. RF pulses and electrons are injected into the waveguide, allowing the electrons to be captured by the RF wave which is then exploited to accomplish electron acceleration. Focusing and steering coils surround the waveguide, minimizing beam divergence and forcing the electrons to stick to a straight path. Upon emerging from the waveguide, the electron stream is directed by a bending magnet to pass through the electron window. The waveguide exit window is constructed of a low atomic number material in order to minimize bremsstrahlung production. In the production of high energy photons, on the other hand, the bending magnet aims the electrons to strike a thick tungsten target, creating bremsstrahlung photons. The presence or absence of the thick target is determined when the linac user selects either photons or electrons on the console. When an electron beam is desired by the linac user, the beam current at the exit window will be on the order of one thousandth of the value required to achieve a clinical photon beam[1]. While a beam current of 100 μA at the exit window is typically

used to create a 6 MV photon beam, an average beam current of about 100 nA is necessary to produce a 6 MeV electron beam. Lower beam currents are needed to generate higher energy electron beams. For example, the production of an 18 MeV beam typically requires a beam current of about 40 nA at the exit window. The electron beams that traverse the waveguide exit window form a thin jet. However, beams of much broader dimensions are required for treating patients. Scattering foils achieve widening of the initially narrow stream of electrons. A collimating system then realizes the beam size and shape dictated by the user. Electrons are heavily influenced by scattering in air; therefore, an applicator must be attached to the base of the linac head to ensure collimation close to the patient surface. The following sections will describe each component of the linac in greater detail. The experiments performed in this work employed an Elekta SL 25 linac, thus descriptions will focus on the types of parts found in that machine. Figure 1-1 provides a general overview of the components particular to the linac employed in this work, the Elekta SL 25.

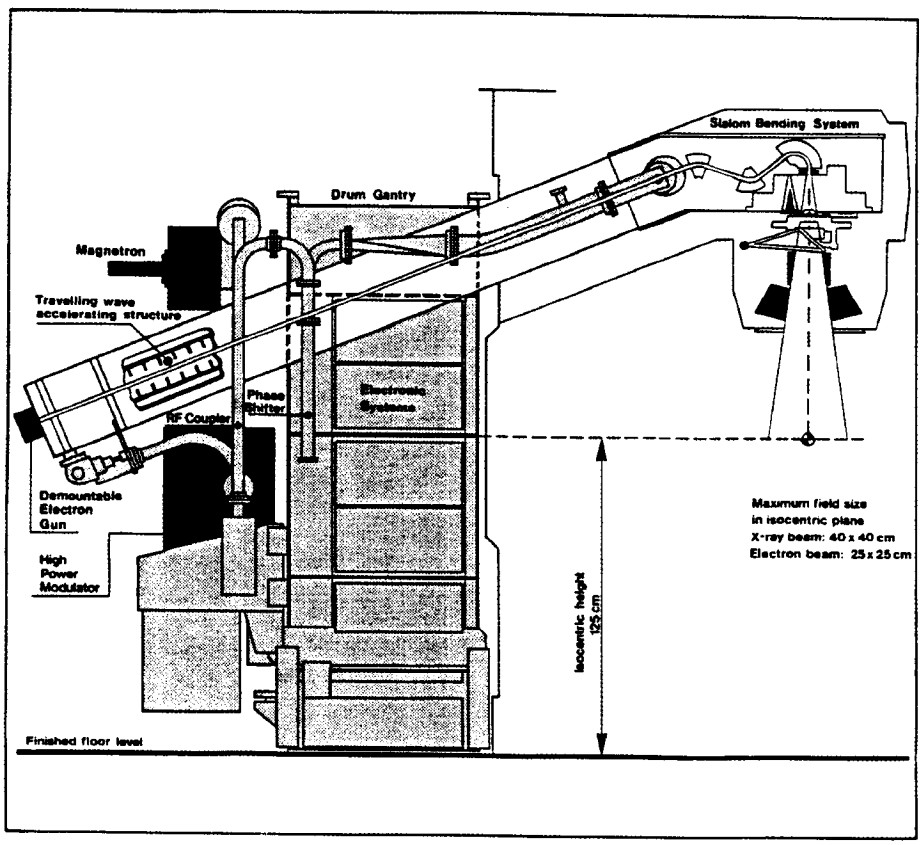


**Figure 1-1:** Overview of the principal systems governing the operation of the Elekta SL-25 linear accelerator. Diagram courtesy of Elekta.

### 1.1.1 The Electron Gun

The chief components of the electron gun are a negatively charged cathode, typically a tungsten filament, and an anode held at ground[1]. This system resides in a glass container under vacuum to prevent traveling electrons from undergoing atomic collisions. When an electric current is applied to the cathode, heating it, electrons are boiled off and cloud around the surface of the filament. A positive potential attracts free electrons in a vacuum, directing the flow of electrons from cathode to anode. A hole in the centre of the anode allows electrons to travel into the waveguide. A potential difference of 50 kV, typical of the Elekta SL series of linacs, causes the electrons to accelerate to $0.4c$, where $c$ is the speed of light, and attain a kinetic energy of 50 keV[2].

Diode electron guns consist solely of a grounded anode and a cathode that receives negative pulses. If several different treatment energies are desired, however, considerable variation of the gun beam current is necessary[1]. A grid may thus be added between cathode and anode, forming a triode, and allowing for current variation without a change in potential difference. In the case of the triode design, a constant negative potential is applied to the cathode[3]. The magnitude of the grid voltage is generally a small fraction of the potential difference that exists between cathode and anode[1]. It controls the magnitude of the injection energy by varying from negative to positive, permitting a larger and larger beam current as it becomes more and more positive[3]. Elekta linacs, however, do not use a triode design and simply control gun beam current by heating the tungsten filament cathode with an adjustable current power supply[2]. A high beam current results in a greater number of electrons sharing the same RF power supplied by the magnetron. Thus, each electron will acquire a lower energy, leading to smaller net beam energy.

### 1.1.2 The Microwave RF Power System

Electrons become high energy as they ride along microwaves in the accelerating waveguide. These microwaves may be produced by either a magnetron, used in the Elekta SL series, or by a klystron. The latter essentially amplifies RF power produced by an RF oscillator while the former directly generates high power

RF fields. Both operate by boiling electrons off a cathode followed by their acceleration towards an anode. Nevertheless, the designs of the magnetron and the klystron are exceedingly different[3]. Magnetrons are usually employed in lower energy linacs while klystrons are found most frequently in higher energy machines. Klystrons are more proficient in the production of the very high peak RF pulses demanded in the operation of higher energy accelerators[1]. As the Elekta SL 25 uses a magnetron as its RF power source, this device will be examined in further detail.

The principal components of a magnetron are a cathode of cylindrical structure encircled by an anode comprised of coupled resonant cavities[3]. This arrangement is housed in glass and is held under vacuum. A permanent magnet generates an intense magnetic field perpendicular to the cross-sectional plane of the resonators[4]. In addition, a pulsed DC electric field incites thermionic emission from the cathode and acceleration towards the anode. The concurrent magnetic and electric fields induce the electrons to undergo intricate corkscrew trajectories as they move out towards the resonant cavities of the anode[1]. As the electrons travel around the hollows of the anode, they interact with the electric fields established across those cavities. The resonators gain energy in this way, the outward-moving electrons radiating energy in the form of RF power and producing high frequency RF oscillations[4]. A special conduit in one of the resonant cavities allows the RF power to travel to a rectangular waveguide which in turn leads to the accelerating waveguide.

The Elekta SL 25 magnetron operates at a nominal frequency of 2856 MHz and the RF power is delivered in pulses with an approximate duration of 3 $\mu s$[2]. The maximum power deliverable by this device is 5 MW. However, this output level is reserved for superior electron energies. The magnetron provides a peak power of 3 MW when energies inferior to 15 MeV have been requested.

### 1.1.3 The Accelerating Waveguide

The aim of the accelerating waveguide is to allow electrons to achieve high kinetic energies. In order for this goal to be accomplished, electrons must be captured by a microwave which they then make use of to gain in velocity and relativistic mass. Therefore, an obvious requirement is that the electron velocity matches the phase

velocity of the wave. A constraint then exists concerning waveguide design. Simple uniform waveguides, such as a hollow metal cylinder, induce phase velocities that surpass $c$, the speed of light[3]. Evidently, such a design would prove fruitless for particle acceleration, since particle velocity cannot attain $c$. A viable design for an accelerating waveguide must thus include obstructions that adequately diminish the phase velocity. 'Loaded' waveguides maintain a phase velocity that is smaller than $c$ with the aid of metal discs inserted along the length of the waveguide, creating a suite of cavities. Each disc is pierced at the centre to allow passage from one cell to the next.

Accelerating waveguides may be either traveling or standing wave systems. In the case of the traveling wave system, electrons surf down the length of the waveguide on the peak of an RF wave. Electrons moving through a standing wave system are passed from one crest of the RF wave to next. The Elekta SL series employs traveling wave accelerators; therefore this type of system will be the subject of a more detailed discussion.

A traveling waveguide is composed of two regions: the bunching section and the relativistic section. Specifically, the Elekta SL series waveguide design includes a total of 74 cells in series. The input mode transformer, also the first cell in the waveguide, retards the phase velocity of the RF wave to $0.4c$, coherent with the velocity of electrons arriving from the electron gun. This action enables the electrons, which are drawn to the positive crests of the RF wave, to be carried by the wave. As the wave accelerates, the electrons are then compelled to follow along. Acceleration is at a maximum in the bunching section of the waveguide, over which the electrons experience a boost in velocity from $0.4c$ to $0.95c$. Six cells constitute the bunching section of the Elekta SL waveguide[2]. The length of these cells increases progressively in order to produce the necessary climb in the phase velocity of the RF wave. In the relativistic section of the waveguide, the electrons see their velocity rise to $0.995c$ but they also experience an increase in relativistic mass. This latter effect is chiefly responsible for the energy gain achieved in the relativistic section of the waveguide.

### 1.1.4 The Bending Magnets

If a treatment beam energy greater than 6 MeV is desired, a fairly long accelerating waveguide is required. It then becomes impossible to mount the waveguide vertically[3]. Therefore, the electron beam must be bent upon emerging from the waveguide. The Elekta SL 25 employs a slalom bending magnet system, comprised of two 45° magnets, opposed in direction, followed by a 112.5° magnet[2]. The slalom system is advantageous over other bending magnet systems as it requires minimal space and boasts an achromatic design which refocuses the spectral spread and the directional spread of the electron beam[3]. Energy detectors are positioned after the first 45° magnet, where any energy spread would be most evident[2]. The slalom system of the Elekta SL 25 produces a focal spot of approximately 2 mm in diameter[5]. Figure 1-2 presents a more detailed view of some of the systems involved in the production of the initial electron beam, notably the accelerating waveguide and the bending magnet system.

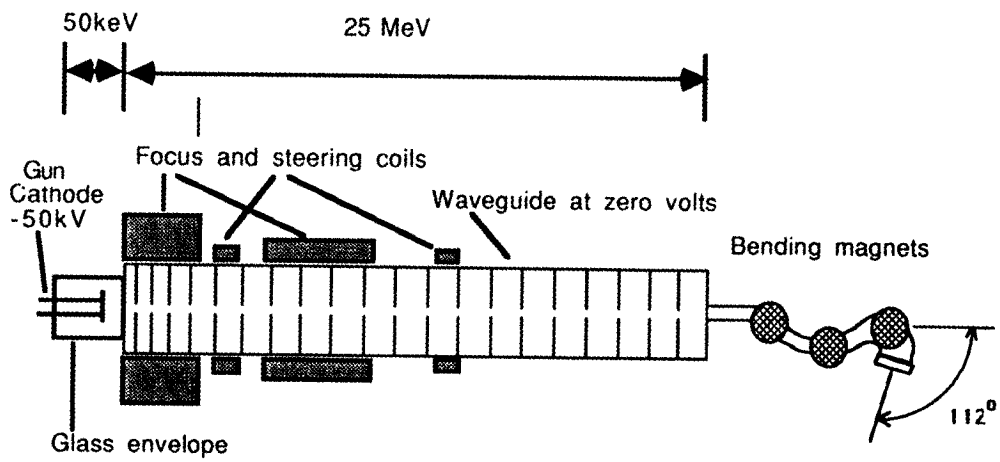


**Figure 1-2:** Accelerating waveguide structure and magnet systems. Diagram courtesy of Elekta.

### 1.1.5 The Scattering Foils

In order for electron beams to be applied therapeutically, they must cover a rather large area in a uniform fashion. Upon its exit from the electron window, the electron beam is only a few millimetres in diameter and exhibits a Gaussian profile[3]. To correct this, either scattering foils or pencil beam scanning is employed.

The latter technique utilizes magnets to deflect the beam[4,6]. Pencil beam scanning is infrequently used although it curtails energy spreading and energy loss and minimizes bremsstrahlung production. The chief drawbacks of such a system are that it may result in charge collection problems and that it is not as safe as scattering foils[4].

Scattering foils are most often used to expand pencil beams to treatment dimensions. A thicker scattering foil optimizes beam flatness but increases energy loss in the foil and boosts bremsstrahlung production. Hence, these conditions necessitate a compromise on scattering foil thickness[4]. The thickness of a thin scattering foil is approximately proportional to the square of the electron energy in the foil[1]. Therefore, different foil thicknesses are required for different beam energies.

The use of dual scattering foils minimizes scattering foil thickness while achieving a high degree of beam flatness[7,8]. The first scattering foil encountered by the electron beam in such a system is typically made of a high atomic number material[3]. A broad Gaussian intensity distribution is present after this first foil[1]. A low atomic number material is generally used for the second foil, which is situated a few centimetres from the first foil[3]. The second foil then flattens the beam profile by rescattering the central section of the Gaussian[1]. Additional enhancement of the dose distribution may be accomplished with a shaped second scattering foil, which offers a varying thickness across the beam[9].

The Elekta SL 25 employs dual scattering foils. This system offers six different tantalum primary scattering foils of varying thickness. A set of four aluminium scattering foils, also of different thicknesses, completes the system. Various combinations of primary and secondary scattering foils produce broad, flat and uniform beam profiles for the nine available electron energies[5].

### 1.1.6 Beam Collimation

The function of the collimating system of a linear accelerator is to provide a defined field size. A fixed primary collimator and diaphragm secondary collimators constitute a basic collimating system. Many contemporary linacs also feature a multi-leaf collimator (MLC), which allows for the production of irregular photon field shapes. Furthermore, this tool is largely responsible for the advent of intensity modulated radiation therapy. In the instance of electron beams, an additional collimating component is required; an applicator must be attached to the linac head such that the field size is defined close to the surface to be irradiated in order to reduce scattering. Figure 1-3 outlines the elements of the Elekta SL 25 collimating system.

The primary collimator lies between the primary scattering foil and the secondary scattering foil. Essentially a conical cut-out in a thick tungsten shielding block, the primary collimator is a fixed structure[1]. In the instance of electron beams, this component does not play a major role in the collimation process. Upon emerging from the exit window, the electron beam is very narrow. After traversing the primary scattering foil, the beam is broadened and of an intensity distribution Gaussian in nature. This broader beam then passes effectively unchanged through the primary collimator. The presence of this structure is necessitated in photon beam collimation as the photon beam acquires width during its creation in the target.

The secondary collimators, or diaphragms, are positioned below the scattering foils. This collimation component is comprised of two pairs of movable jaws, constructed of a high atomic number material in order to maximize attenuation. Tungsten is the material of choice in the case of the Elekta SL 25[2]. One set of diaphragms is located above the other. The pairs of jaws are designated X and Y for control purposes. Formerly, linac jaws could only move in tandem. However, today's linacs offer independent jaws, allowing for asymmetric fields. Isocentric fields with sides that range from millimetres to 40 cm are typically permitted by secondary diaphragm collimators[3].

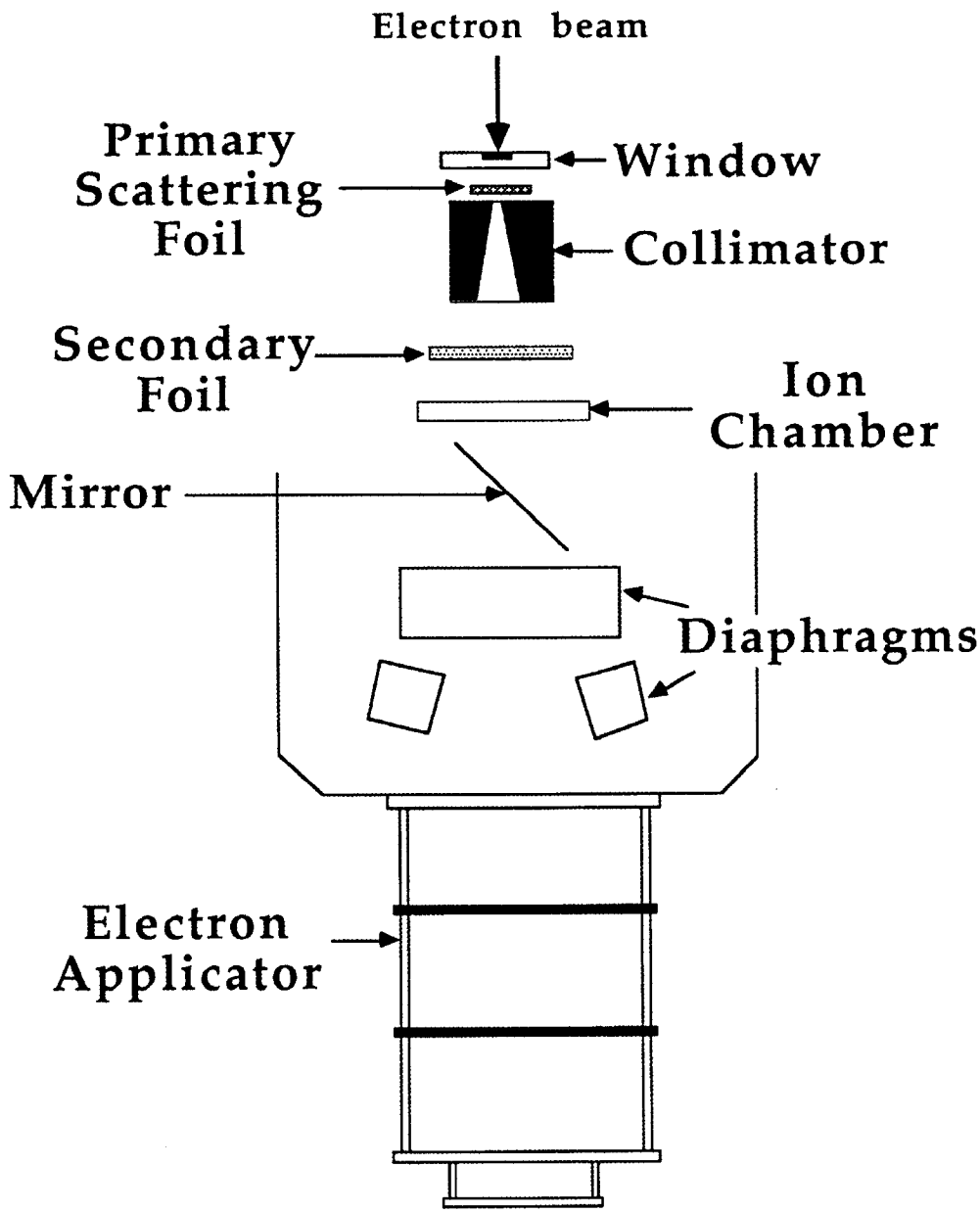


**Figure 1-3:** Overview of the collimation system of the Elekta SL 25 accelerator. Diagram courtesy of Elekta.

The MLC, typically constructed of tungsten, is composed of many small moving pieces that may be employed in the creation of irregular field shapes. The Elekta SL 25 MLC is comprised of eighty individual blocking elements[2]. MLCs are often offered as a collimation device that is supplemental to the primary and secondary collimators. In the case of the Elekta SL 25 fitted with an MLC, the X jaws are of thickness 7.8 cm while the Y jaws are made smaller, 3 cm thick, and essentially serve as a back-up for MLC leaves in order to diminish radiation leakage. MLC leaves are 7.5 cm thick. When an electron beam is requested, the leaves of the Elekta SL 25 MLC are always open to their full extent.

Electron beams are heavily influenced by in-air scattering[4], especially when considering energies below 15 MeV. Therefore, the electron beam must be collimated close to the surface of the patient. Furthermore, the electron beam must be significantly broader than the diaphragm collimator after leaving the secondary scattering foil. This condition ensures that the collimated beam maintains equilibrium between electrons scattered into and out of the beam. These requirements are met by the use of applicators, which are fitted to the accessories mount situated at base of the linac head. It is customary for a distance of 5 cm to remain between the base of the applicator and the patient surface. Discrete field sizes spanning 5x5 $cm^2$ to 25x25 $cm^2$ are typically provided by electron applicators[1]. Applicator design demonstrates much variation and is specific to linac type. Models range from solid conical structures to open tiered structures, like those particular to the Elekta SL 25. The frame of an Elekta SL 25 applicator is constructed of four aluminium bars, situated at the corners of the applicator. Three tiers with rectangular cut-outs intersect the frame orthogonally. The tiers are fabricated of lead and aluminium. The last tier includes a detachable mask which may be replaced by cerrobend cut-outs. The smallest applicator available for the Elekta SL 25 measures 6x6 $cm^2$. When a given applicator is fitted to the treatment head of the Elekta SL 25, the jaws automatically assume the most advantageous position for that applicator size and the selected beam energy[2].

## 1.2 Characteristics of Electron Beams Designated for Radiation Therapy

Although photons and electrons demonstrate equivalence in terms of biological effectiveness[4], electron beams occupy a distinct niche in radiation therapy. The strength of electron beams as a cancer treatment modality stems from their physical characteristics, in particular the shape of their percent depth dose (PDD) curves. Electron PDD curves are typified by a high surface dose leading to a slight build-up region followed by a sharp dose decline and finally a small bremsstrahlung tail. The shape of electron PDD curves suggests electron beams for treatment of subdermal tumours, allowing sparing of healthy tissue at greater depths. The electron beam distribution is also more uniform over the target volume in comparison with the superficial x-ray treatment technique. Examples of cases where electron beams may be employed are skin and lip cancers, nose and ear treatment, superficial lymphomas and sarcomas on the back of the hand or foot. Electrons are also frequently used to provide additional dosage in a photon treatment. For example, boost irradiation to lymph nodes. The typical range of energies employed in radiation therapy is 4-20 MeV. Beyond approximately 20 MeV, the abruptness of the dose fall-off region is considerably lessened, deteriorating the ability of the electron beam to spare underlying tissue. Hence, higher energy electron beams generally fail to demonstrate clinical usefulness. In addition to examining the features of the electron PDD curve, this chapter will explore electron beam profiles and isodose curves. Beam quality is a parameter that is very important to radiation dosimetry. Several formulae employing an assortment of parameters serve to define beam energy at various points of interest. This part of the chapter will investigate these expressions.

### 1.2.1 The Build-Up Region of Electron Beam PDD Curves

Electron beam PDD curves also have build-up regions akin to those seen for photon beams but with dramatic differences. Unlike photon beams, which boast low surface doses resulting in a skin-sparing effect, electron beams produce surface doses in the range of 80-90%[4]. Figure 1-4 compares electron and photon beam PDD curves.

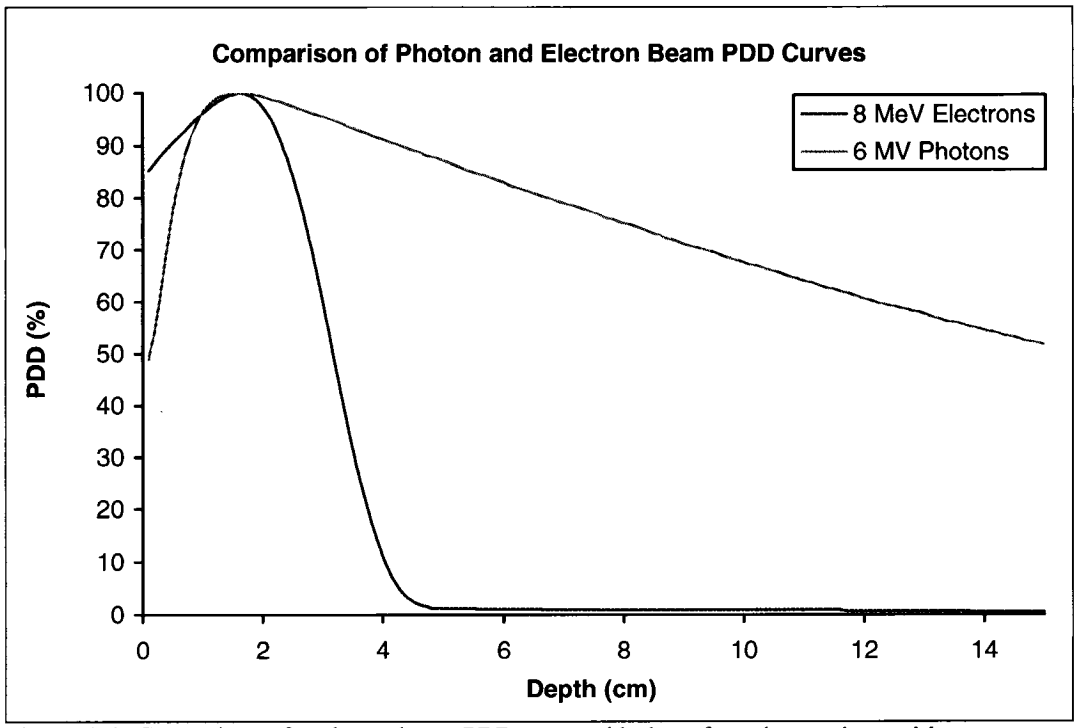


**Figure 1-4:** Comparison of a photon beam PDD curve with that of an electron beam. Measurement conditions for both curves included a 10x10 $cm^2$ field and an SSD of 100 cm.

This difference stems from the fact that photons beams must first create secondary electrons before energy absorption can occur. Thus, the build-up region in photon beams is due to an increase in the number of electrons present. For an electron beam, energy deposition may begin immediately at the point of beam entry into the medium, resulting in a large surface dose. In addition, a smaller portion of the surface dose stems from low energy electrons and photons produced in the accelerator head and the air. The chief cause for the build-up region of electron PDD curves is not any increase in the number of electrons present but is due to scattering[4]. At the point of entry on the surface, the electron beam may be considered as a parallel beam[10]. However, as electrons penetrate deeper into the medium, their paths become more oblique due to multiple scattering[4]. Hence, as path obliquity is increased, electron fluence and thus energy deposited per unit depth are augmented as well. Figure 1-5 illustrates how electron fluence per unit depth is amplified as electron paths become more oblique.

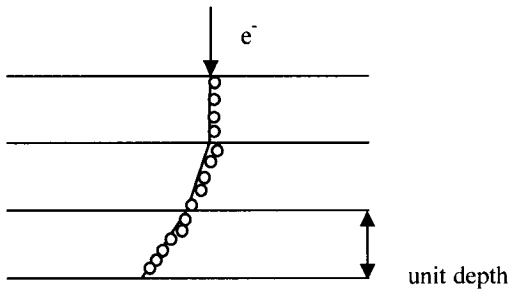


**Figure 1-5:** Increase of fluence per unit depth due to scattering.

These conditions are responsible for the rising portion of the electron PDD curve. The peak occurs when the initially parallel beam becomes completely diffused[7]. The build-up region, we may note, is less pronounced for higher energies due to the fact that scattering is reduced as energy is increased. A lower energy electron PDD curve is characterized by a more pronounced build-up region with lower surface dose and a shallower depth of dose maximum ($d_{max}$). Higher energy beams are less easily scattered and therefore maintain relatively straight tracks upon penetration into the medium, which consequently situates $d_{max}$ at a more profound depth[4].

### 1.2.2 Characterization of Electron Beam PDD Curves

In 1976, Brahme and Svensson denounced the practice of characterizing central axis percent depth dose curves with only one parameter, the practical range, $R_p$[11]. They stipulated that six additional parameters were required, as $R_p$ provides little information pertaining to the clinically relevant portion of the PDD. Therefore, in addition to $R_p$, range parameters occurring along the therapeutically useful sections of the electron PDD curve were recommended. These included the depth of dose maximum, $d_{max}$, a parameter representing the therapeutic range, $d_{85}$, and the depth at which the dose has fallen to 50 % of its peak value, $d_{50}$. Two other parameters are doses; the entrance or surface dose, discussed previously and the exit or bremsstrahlung dose. The final parameter is the dose gradient of the fall-off portion of the PDD curve, which is related to tissue sparing behind the tumour.

#### 1.2.2.1 The Surface Dose

It is commonly accepted that surface dose actually be measured at a depth of 0.5 mm[4]. The most superficial layers of the skin are quite insensitive to radiation, rendering a measure of dose at the true skin surface insignificant. The first radiosensitive skin layer lies at a depth of approximately 0.1 mm. More importantly, the tools of radiation measurement, such as ionization chambers with relatively thick windows and finite volumes, make it unfeasible to obtain dose at the exact surface of a phantom. Acquiring a dose measurement at a depth of 0.5 mm, however, is a realistic task for many detectors[11].

#### 1.2.2.2 The Bremsstrahlung Dose

The dose delivered by an electron beam incorporates a photon component. In electron mode, no special target intercepts the electron beam with the purpose of generating bremsstrahlung photons. Nevertheless, the waveguide exit, scattering foils, monitor chamber, collimating system, air gap and the irradiated medium itself all behave as targets and are responsible for the bremsstrahlung dose, $D_x$. The greatest contribution to $D_x$ is derived from the scattering foils[12]. Hence, this component should be designed to be as thin as possible while still achieving the desired spread of the beam. $D_x$ may be valued as the dose corresponding to the depth at which the bremsstrahlung tail becomes absolutely straight[13]. At this point, the electrons have been completely exhausted and only photons remain. The magnitude of $D_x$ rises with beam energy[14]. Over the scope of energies employed in radiation therapy, $D_x$ is typically less than 1 % where lower electron energies are concerned and does not exceed 8 % in the case of higher electron energies[13]. $D_x$ also varies with field size and the thickness of the air gap[14].

#### 1.2.2.3 The Practical Range

The intersection of the sharpest tangent to the fall-off region with the extrapolation of the photon background defines the practical range, $R_p$[11]. This parameter is empirically linked to the most probable energy at the surface, $E_{p,0}$. Electrons passing through a given thickness of material will emerge with a spectrum

of energies. This phenomenon is known as straggling. $E_{p,0}$, therefore, corresponds to the peak of the energy spectrum at surface of the phantom. The energy spread apparent at the surface was thus created in the scattering foils, as well as in other components and materials that obstructed the initial electron beam. The most probable energy at the surface demonstrates an empirical dependency on the practical range, applicable to a broad electron beam orthogonally incident to a semi-infinite water phantom[14]:

$$E_{p,0} = C_1 + C_2 R_p + C_3 R_p^2, \tag{1-1}$$

where $C_1$, $C_2$ and $C_3$ are constants of respective values 0.22 MeV, 1.98 MeVcm$^{-1}$ and 0.0025 MeVcm$^{-2}$. Berger and Seltzer established from Monte Carlo data that the above relationship is accurate to within $\pm$ 1 % for energies ranging from 1 to 60 MeV[7]. A host of experimenters have demonstrated the validity of Eq. (1-1) over the same scope of energies by comparison with measured data[7,14]. Although Eq. (1-1) was initially formulated for beams characterized by only a minor energy spread, it is nonetheless functional for electron beams with a broad straggling energy distribution, like that particular to a linac[14]. The most probable energy at depth in a water phantom, $E_p(z)$, may be obtained via the empirically derived Harder relationship[7]:

$$E_p(z) = E_{p,0}\left(1 - \frac{z}{R_p}\right) \quad , \tag{1-2}$$

where $z$ represents depth. Eq. (1-2) expresses a linear decline of the most probable energy with an increase in the thickness of material traversed. Dosimetric calculations often demand the mean energy at depth, $\overline{E}(z)$. $E_p(z)$ may serve as an approximation of $\overline{E}(z)$[14]. However, the mean energy decreases more rapidly with depth than the most probable energy[7], as implied by the skewed shape of the energy spectrum at a given depth, characterized by a long tail on the lower energy side of the peak.

### 1.2.2.4 The Depth of 50 % Dose

Another depth parameter, $d_{50}$, may also be used for determining beam energy. $d_{50}$ is localized at the depth reached when the dose is reduced to half of its maximum value[11]. The following empirical formula may be employed to determine the mean energy of an electron beam at the surface of a water phantom, $\overline{E_0}$[7]:

$$\overline{E_0} = C_4 d_{50}, \tag{1-3}$$

where $C_4$ is a constant. In 1983, the American Association of Physicists in Medicine (AAPM) recommended a value of 2.33 $MeVcm^{-1}$ for $C_4$. However, this value has been the subject of much debate. The Hospital Physicists Association specified a value of 2.4 $MeVcm^{-1}$ to be employed as the constant in Eq. (1-3). A value of 2.38 $MeVcm^{-1}$ for $C_4$ was proposed by Wu et al, particular for use with depth-ionization curves[15]. Another formula, mostly employed in European institutions, also describes the mean energy at the surface as a function of $d_{50}$[16], where $d_{50}$ is expressed in centimetres and $\overline{E_0}$ is given in MeV:

$$\overline{E_0} = 2.04 d_{50} + 1.30. \tag{1-4}$$

### 1.2.2.5 The Depth of Dose Maximum

The depth at which the maximum dose value is achieved, $d_{max}$, also serves to characterize PDD curves. The location of this parameter for a given combination of nominal beam energy, field size and source to surface distance (SSD) is fairly variable for beams produced by different accelerator types[14]. This phenomenon is rooted in $d_{max}$'s dependence on the most probable energy and the shape of the energy distribution. Variation in $d_{max}$ is particularly apparent for higher energy electron beams, for which surface doses are elevated and the build-up region is wide and flat. Hence, the reliability of $d_{max}$ as a means of characterizing PDD curves is problematic.

### 1.2.2.6 The Therapeutic Depth

Brahme and Svensson suggested that a depth parameter that matches the limits of the target volume be included in the set that describes PDD curves[11]. More explicitly, the tumour volume should preferably be situated between the surface and this therapeutic depth. The inclusion of such a parameter would be advantageous due to its intimate association with the location of the target. Ideally, dosage to the target volume should demonstrate great uniformity. A committee working for the International Commission on Radiation Units and Measurements (ICRU) is currently compiling a report concerning prescription for electron beam therapy, in which the question of target volume dose uniformity is sure to be addressed. A similar report was published particular to photon beam therapy[17], stipulating allowable margins of +7 % and -5 % over the target volume. Where electron beam therapy is concerned, dose variations of even 10 % within the target zone have been shown to introduce significant disparity in the proportion of patients cured and the number of ensuing complications[11]. Accordingly, the electron energy must be selected such that the boundaries of the target volume lie between the surface and the depth of 90 % dose beyond $d_{max}$[4]. Although a choice of higher electron energy ensures a flatter build-up region, therefore enhanced dose uniformity, a larger irradiated volume is consequential. Hence, a compromise between dose uniformity over the target volume and safeguarding neighbouring healthy tissues must be established. This goal may be achieved by extending the therapeutic range to a depth that corresponds to a dose level between 80 % and 90 %[4,11]. Obviously, the separation between the 80 % and 90 % dose levels varies with electron energy. The shape of this section of the PDD curve, where dose has begun to gently decrease, also demonstrates a dependence on the design of the accelerator head[11]. A thinner scattering foil establishes a sharper dose gradient but instigates decreased uniformity. The parameter recommended by Brahme and Svensson was the depth corresponding to the point where the dose has dropped to 85 % of its peak value, $d_{85}$. Some centres do, however, characterize the region situated after $d_{max}$ and before the abrupt dose fall-off by depths corresponding to either 90 % or 80 % of dose maximum.

### 1.2.2.7 The Dose Gradient

One of the most attractive features of the electron PDD curve is the dose fall-off region, which proves eminently helpful in sparing healthy tissue beyond the tumour. It is useful to evaluate this section of the PDD curve in terms of steepness. A sharper dose decline results in enhanced tissue sparing. The normalized dose gradient, $G$, serves to describe the dose fall-off region. Brahme and Svensson defined the dose gradient as[11]:

$$G = \frac{R_p}{D_{\max} - D_x}\left(\frac{dD}{dz}\right)_{\max}, \tag{1-5}$$

where $D_{\max}$ is the peak dose, $D_x$ and $R_p$ are respectively the bremsstrahlung dose and practical range, as discussed previously. The difference $D_{\max} - D_x$ represents the maximum dose due to electrons. $\left(\frac{dD}{dz}\right)_{\max}$ is the maximum dose gradient. The unitless parameter $G$ may be determined in a practical manner by the formula[11]:

$$G = \frac{R_p}{R_p - R_q}, \tag{1-6}$$

where $R_q$ is defined as the point at which the steepest tangent to the fall-off region crosses the 100 % dose level[12]. The value of $G$ lies between 2 and 3 over the pertinent energy range. The lower limit for $G$ recommended by the ICRU is 2.3[7]. A higher value of $G$ indicates a lower electron energy beam, with a more dramatic dose fall-off region. Conversely, a lower value of $G$ implies a higher energy beam.

### 1.2.3 Variation of PDD Curves

Now that the parameters characterizing PDD curves have been explored, the variation of these curves with energy, field size, source to surface distance (SSD) and angle of incidence may be considered.

### 1.2.3.1 Variation with Energy

As beam energy is augmented, the surface dose becomes elevated, depth of dose maximum, $d_{max}$, becomes positioned deeper within the medium, the dose fall-off region becomes less abrupt and the bremsstrahlung dose, $D_x$, experiences an increase. These effects are depicted in Figure 1-7. After about 18 MeV, however, $d_{max}$ again becomes situated closer to the surface. Electron beams of energy superior to 18 MeV are still characterized, nonetheless, by broad plateaus around depth of dose maximum, where very little variation of dose is observed.

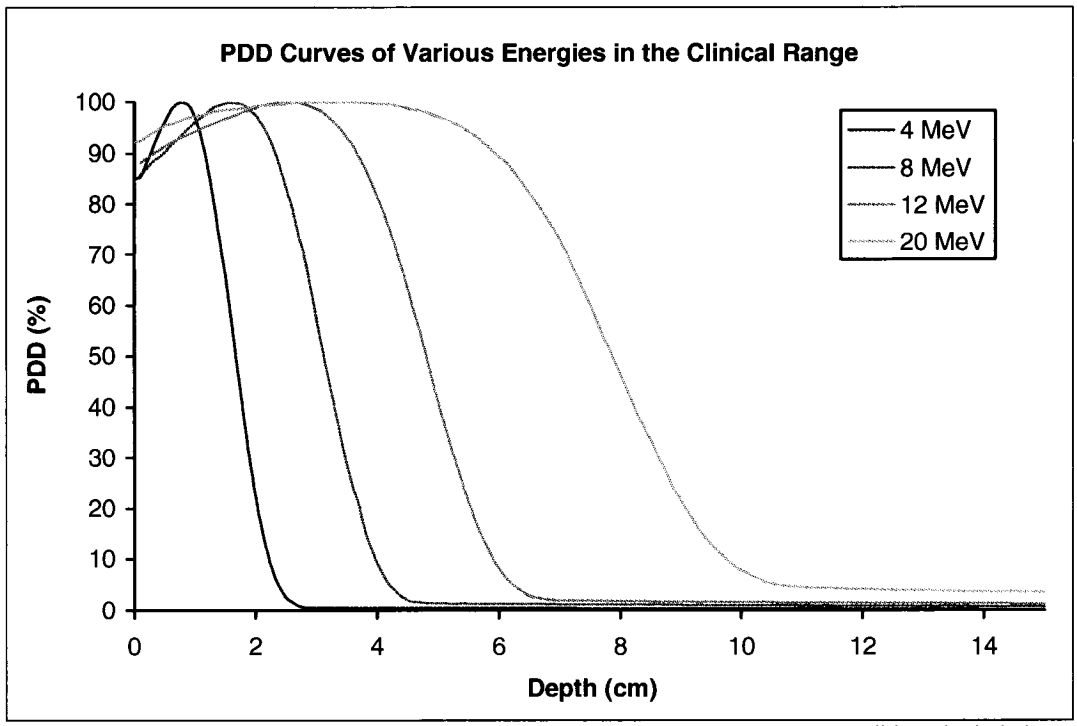


**Figure 1-7:** PDD curves of various energies in the clinical range. Measurement conditions included a field size of 20x20 $cm^2$ and an SSD of 100 cm.

### 1.2.3.2 Variation with Field Size

Over most of the clinical range of electron energies, PDD curves corresponding to field sizes superior to 6x6 $cm^2$ and a given energy and SSD combination are quite indistinguishable from one another. In the case of small field PDD curves, dramatic changes are observable. Lateral scattering is responsible for depth-dose dependence on field size. Furthermore, it has been demonstrated that

discernible differences between central axis PDD curves arise only if the field radius measures less than half of the electron range[14]. In addition, a collimation system design that generates a fair amount of scatter renders it difficult to predict how PDD curves will vary with field size[7].

Small field PDD curves are typically characterized by very high surface doses and consequentially very little build-up[4]. Under small beam conditions, regions adjacent to the central portion of the field are not irradiated and thus do not contribute scatter to the central axis. The lack of build-up effect is significant for beams of nominal energy 4-10 MeV and of diameter, in centimetres, less than $E_{p,0}/2.5$[4], where $E_{p,0}$ is the most probable energy at the surface, in MeV. Figure 1-8 presents PDD curves over a gamut of field sizes.

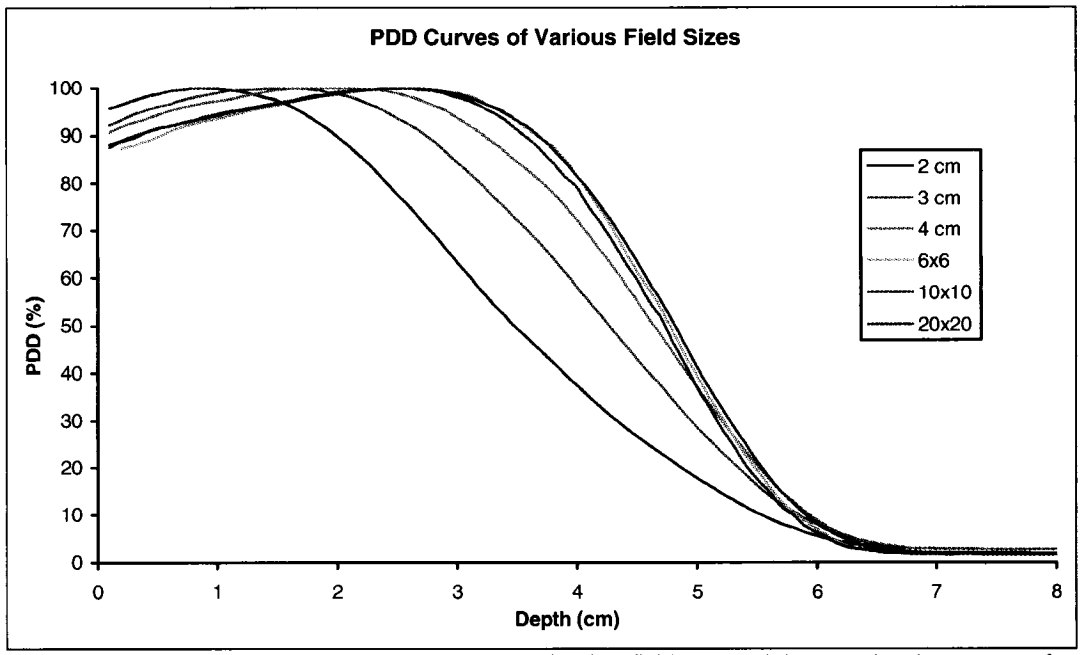


**Figure 1-8:** PDD curves of various field sizes: circular fields created by cerrobend cut-outs of diameters 2 cm, 3 cm and 4 cm inserted into a 10x10 $cm^2$ applicator and larger square fields created by applicators of dimensions 6x6 $cm^2$, 10x10 $cm^2$ and 20x20 $cm^2$. Other measurement conditions included a 12 MeV beam and an SSD of 100 cm.

### 1.2.4.3 Variation with Source to Surface Distance

The variation of PDD curves of given energy and field size with different SSDs is principally governed by geometric beam divergence[14]. Hence, the inverse

square law should suffice to achieve conformity of such curves with respect to one another[4]. The inverse square law assumes that the electron beam originates from a point source. In reality, this is not the case, as the broad electron beam is produced from a pencil beam with the aid of scattering foils, as described in the first section of this chapter. Nevertheless, as it *appears* that the beam stems from a virtual source, this assumption may be utilized in order to simplify dosimetric calculations. The virtual source distance (*VSD*) may be obtained by taking radiographs at varying distances of a wire grid or a metal plate punctured with pinholes and then performing backprojections[14]. A similar technique involves backprojections of field size magnifications with distance on film. Once the virtual source distance has been found, it may be used in the necessary inverse square law calculations. However, it has been demonstrated that inverse square corrections incorporating the *VSD* are only valid for large field sizes[13]. Therefore, Khan has proposed an effective SSD, $SSD_{eff}$, which, when employed in the inverse square formula, provides the correct relationship between PDD curves of assorted SSDs. Ionization is customarily measured at $d_{max}$ when determining the effective SSD, with all conditions constant with the exception of air gap size. The inverse square law stipulates that[13]:

$$\frac{I_0}{I_g} = \left( \frac{SSD_{eff} + d_{max} + g}{SSD_{eff} + d_{max}} \right)^2, \tag{1-7}$$

where $I_0$ is the ionization when no gap exists between the applicator and the phantom surface. $I_g$ is the ionization measured in the case of a given gap distance $g$. By taking the square root of both sides of Eq. (1-7), a linear function of air gap distance is obtained, the slope of which equals $\frac{1}{SSD_{eff} + d_{max}}$. Rearrangement of Eq. (1-7) demonstrates that the effective SSD may be computed as the difference between the reciprocal of the slope and $d_{max}$. Therefore, a plot $\sqrt{\frac{I_0}{I_g}}$ versus $g$ provides sufficient information to calculate the effective SSD. Ionization measured at a depth other than $d_{max}$ has no significant effect on the computed $SSD_{eff}$ for a given field size and energy combination. Therefore, the same effective SSD may be employed to adjust an entire percent depth dose curve.

When considering a relatively small change in SSD for a low energy beam, the difference between the PDD curves concerned is negligible[7] and no inverse square correction is required in order for the curves to coincide with one another. Generally, if the applicator walls contribute much scattered radiation, a lower surface dose and a more profound $d_{max}$ will be consequential to an augmented SSD. Especially large variations in SSD necessitate that changes in air absorption and scattering be considered.

#### 1.2.2.4 Variation with Angle of Incidence

The central axis depth-dose curve, as well as the dose distribution as a whole, of a beam of oblique incidence is markedly different from that of a similar beam of orthogonal incidence. Consider an electron beam which strikes the medium to be irradiated at an angle of incidence other than normal. Shallow points along the central axis are bombarded with scatter from neighbouring regions where greater amounts of medium have been traversed. Conversely, at more profound depths, a decrease in scatter to the central axis from adjacent regions is observed[18]. Therefore, a central axis PDD curve measured under the condition of oblique incidence will demonstrate higher doses at shallow depths and diminished doses deeper within the medium. Such variation in scatter renders inverse square corrections inadequate as means of predicting PDD curves of angled beams from measured beams of normal incidence. Entrance dose rises with angle of incidence and the beam demonstrates less power of penetration[4]. Scattering contributions become heavily altered when the angle of incidence surpasses 30° from the normal[18]. Increased angles of incidence result in percent depth dose curves that are progressively shifted towards the surface in comparison with a PDD curve pertaining to a beam of the same conditions but perpendicularly incident. Figure 1-9 demonstrates the effect of increased obliquity for given energy and field size combinations.

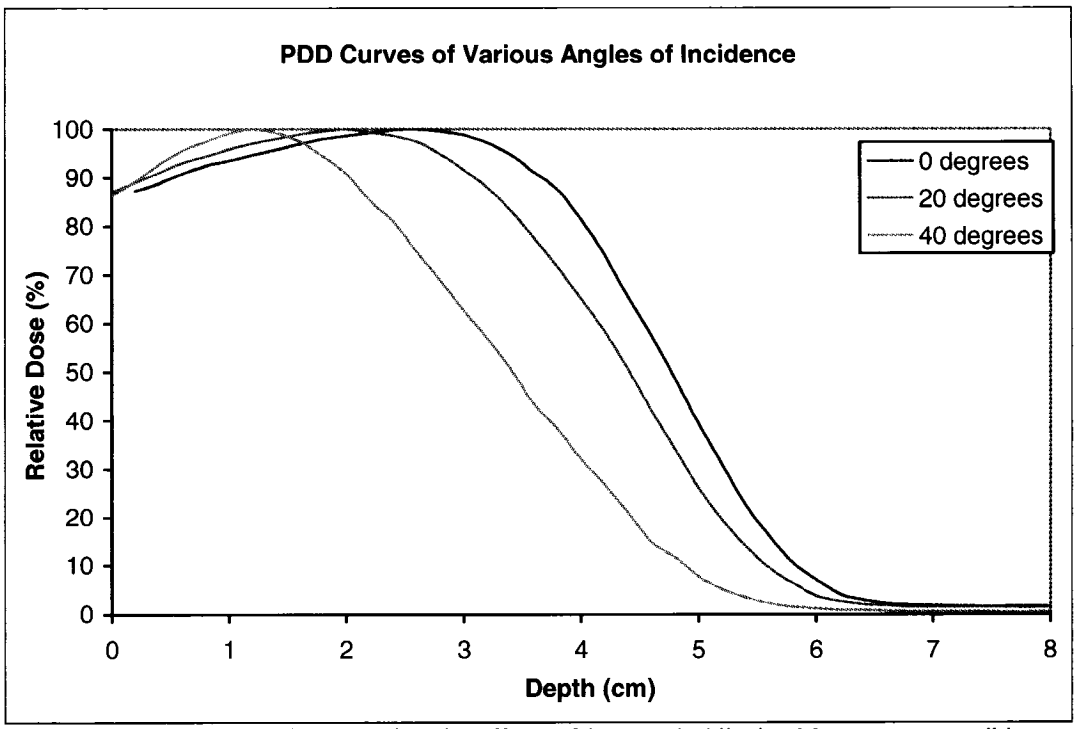


**Figure 1-8 :** PDD curves demonstrating the effects of increased obliquity. Measurement conditions included a 12 MeV beam and a field size of 6x6 $cm^2$ created with the standard applicator.

### 1.2.5 Isodose Distributions

Obviously, therapy electron beams target three dimensional volumes. Hence, a central axis PDD curve does not suffice to describe a given dose distribution. Isodose curves may supplement a PDD curve to ensure a more complete representation of the dose distribution. Isodose curves are lines of equal dose plotted on a two dimensional plane. In general, isodose lines are plotted at regular intervals and normalized to a reference point, usually $d_{max}$. When concerned with a low energy electron beam, all isodose lines will broaden with depth[13]. While the low value isodose lines expand considerably with depth in the case of high energy electron beams, the high value isodoses become somewhat constricted[4,14]. This effect is exacerbated for small field sizes. Figure 1-10 presents a set of isodose curves for a high energy electron beam.

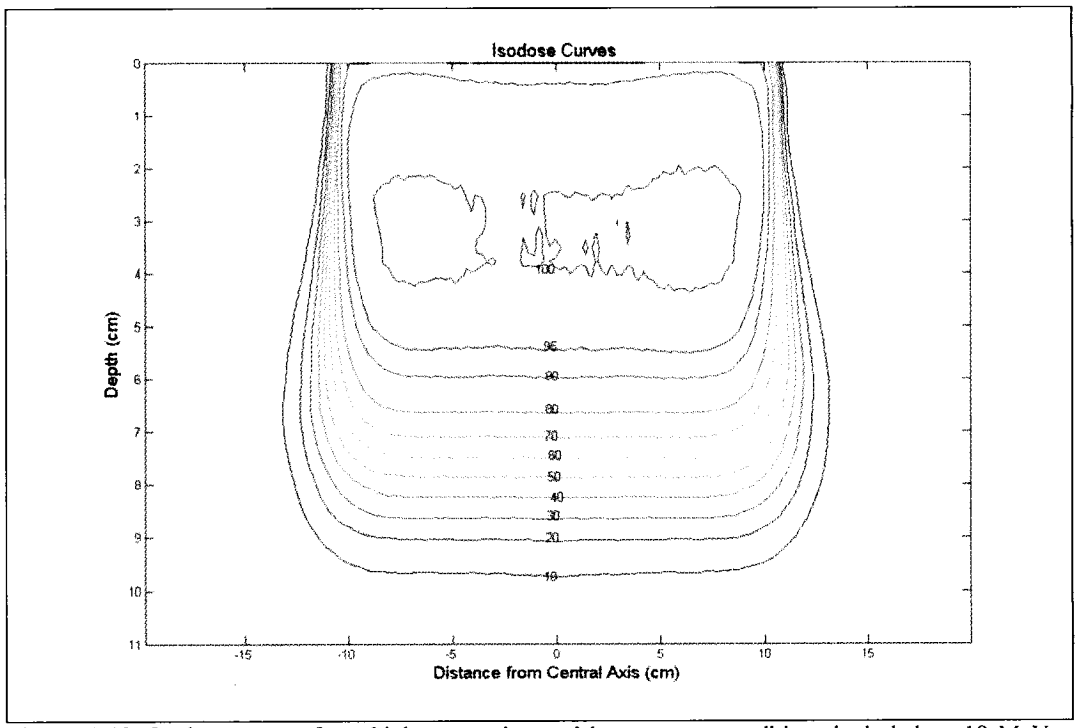


**Figure 1-10:** Isodose curves for a high energy beam. Measurement conditions included an 18 MeV beam, a field size of 20x20 $cm^2$ and an SSD of 100 cm.

### 1.2.6 Electron Beam Uniformity

Clinical electron beams must demonstrate uniformity across a given field. Beam profiles measured orthogonally to the central axis at a particular depth may be evaluated in terms of symmetry and flatness. Beam symmetry implies that points at equal and opposite distances from the central axis should correspond to the same dose value for a regular field. The AAPM recommends a tolerance of $\pm$ 2 % for this criterion at a reference plane[13]. The plane perpendicular to the depth axis at the 95 % dose level beyond the peak dose constitutes a favourable reference plane. Consider the area within lines drawn 2 cm within the geometric field edges for fields equal to or superior to 10x10 $cm^2$. Dose variation within this region should be minimal in order to satisfy beam flatness requirements. Fluctuations within $\pm$ 3 % are preferable and variations exceeding $\pm$ 5 % are intolerable[14].

### 1.2.7 Penumbra

Precision is demanded of the therapeutic electron beam not only in regions of reasonably constant dose but also in regions of dramatic dose elevation or decline. The general definition of the physical penumbra of an electron beam is the distance that lies between two particular isodose curves at a particular depth. Thus, a considerable dependence on depth is intrinsic to this definition. This parameter serves to provide information pertaining to regions of rapidly varying dose. Customarily, the distance between the 80 % and the 20 % dose levels is used as a measure of penumbra[13]. In order to make such a parameter clinically relevant, ICRU 35 suggests that the reference depth be taken as half the therapeutic range, where the centre of the tumour volume should lie[7]. For a 10 MeV beam of good geometry, the penumbra should measure approximately 2 mm. The limit of acceptability for this case is 4 mm. The penumbra is affected by the effective SSD, scattering stemming from the collimating system and the distance between the base of the collimator and the phantom surface.

## 1.3 References


1. Karzmark, C.J., Nunan, Craig S., Tanabe, Eiji, *Medical Electron Accelerators*, McGraw-Hill, Inc., New York, 1993.

2. Eleckta Users Manual 1994.

3. Van Dyk, Jacob, editor, *The Modern Technology of Radiation Oncology*, Chapter 11, Medical Physics Publishing, Madison, WI, 1999.

4. Klevenhagen, S.C., *Physics of Electron Beam Therapy*, Adam Hilger, Ltd., Bristol, 1985.

5. Jatinder, R., Palta, Inder K., Daftari, K., M. Ayyangar, N. Suntharalingham, *Electron beam characteristics on a Philips SL 25*, Med. Phys. 17(1), p.27-34, 1990.

6. Pfalzner, P.M., Clarke, H.C., *Radiation parameters of 6 to 20 MeV scanning electron beams from the Saturne linear accelerator*, Med. Phys. 9(1), p. 117-120, 1982.

7. International Commission on Radiation Units and Measurement (ICRU), Report No 35, *Radiation Dosimetry: Electron Beams with Energies Between 1 and 50 MeV*, 1984.

8. Taumann, L., *The treatment head design for medical linear accelerators*, IEEE trans. Nuc. Sci., NS-328, p.1893-1898, 1981.

9. Bjarngard, B.E., Piontek, R.W., Svensson, G.K., *Electron scattering and collimation system for a 12-MeV linear accelerator*, Med. Phys. 3(3), p. 153-158, 1976.

10. Brahme, Anders, *Geometric parameters of clinical electron beams*, Acta Radiol Suppl 364, p. 11-19, 1983.

11. Brahme, Anders, Svensson, Hans, *Specification of electron beam quality from the central-axis depth absorbed-dose distribution*, Med Phys 3(2), p. 95-102, 1976.

12. British Journal of Radiology (BJR), Supplement 25, *Central Axis Depth Dose Data for Use in Radiotherapy: 1996.*

13. Khan, Faiz M, *The Physics of Radiation Therapy*, Williams & Wilkins, Baltimore, 1994.

14. Khan, Faiz M. et al., *Clinical electron beam dosimetry: Report of the AAPM Radiation Therapy Committee Task Group No. 25*, Med Phys 18(1), p. 73-109, 1991.

15. Wu, A., Kalend, A., Zickler, R.D., Sternick, E.S., *Comments on the method of energy determination for electron beams in the TG-21 protocol*, Med Phys 11(6), p. 871-874, 1984.

16. Schmidt, R., *Medizinische Strahlenphysik V: Dosimetrie mit Ionisationskammern*, http://www.uke.uni-hamburg.de

17. International Commission on Radiation Units and Measurement (ICRU), Report No 50, *Prescribing, Recording, and Reporting Photon Beam Therapy*, 1993.

18. Ekstrand, K. E., Dixon, R.L., *The problem of obliquely incident beams in electron-beam treatment planning*, Med Phys 9(2), p. 276-278, 1982.

# Chapter 2

## Electron-Matter Interactions

This chapter is concerned with the manner in which electrons interact with matter. The atoms of a given medium subject any passing electrons to their Coulomb fields. Accordingly, interaction type may be classified in terms of the incident electron's distance from the atom. This distance may be described in terms of the impact parameter. The latter is defined as the distance between the incident particle and the atom at nearest approach. The first portion of the chapter discusses the various interaction types categorized in the fashion just described. The behaviour of electrons as they penetrate a material may be elucidated by considering the effects of scattering and energy loss. With regards to electron beam treatment planning, multiple Coulomb scattering is undoubtedly the most important scattering phenomenon. The second section of this chapter is dedicated to multiple scattering and scattering power, a powerful means of quantifying the effects of scattering events. Energy loss is expressed in terms of the fundamental parameter stopping power, which is the subject of the third part of the chapter. Finally, the chapter concludes with a summary of Fermi-Eyges theory which states that the generalized distribution for an electron pencil beam incident on a semi-infinite homogeneous phantom may be represented as a Gaussian. Description of the electron beam as Gaussian lies at the heart of CadPlan electron beam treatment planning.

### 2.1 Interaction Types

Electron interactions with matter may be grouped into three main classes. The distinction between these types is based on how the impact parameter, $b$, compares to the atomic radius, $r_a$, for a given interaction. Section 2.1.1 discusses interactions in which $b << r_a$, that is, when the incoming electron interacts with the nucleus. Hard collisions are the subject of section 2.1.2. This interaction class is so-named due to the large energy transfers particular to these interactions which occur between the incoming electron and a single orbital electron. In that instance, the impact parameter is on the order of the atomic radius. The remaining group of interactions is known as

soft collisions, occurring when $b >> r_a$. This interaction type involves the entire atom reacting as a unit to the incident electron and is described in section 2.1.3.

### 2.1.1 Electron Interaction with the Nucleus

When $b << r_a$, the incident electron engages in Coulombic interaction with the nuclear field. Over 97% of such encounters result in elastic scattering of the incoming electron. In the remaining few percent of cases, the incident electron suffers a radiative energy loss in the form of bremsstrahlung photons.

#### 2.1.1.1 Elastic Collisions

Consider scattering stemming from an elastic collision of an incident electron of a given velocity with the nucleus of an atom of the absorber. Mott[1] derived an expression that provides the differential scattering cross-section of an elastic electron-nucleus collision, $\left(\frac{d\sigma}{d\Omega}\right)_{e-n}$, in the case of an incident electron of spin ½:

$$\left(\frac{d\sigma}{d\Omega}\right)_{e-n} = \left(\frac{D_{e-n}}{4}\right)^2 \frac{1}{\sin^4\frac{\theta}{2}}\left\{1-\beta^2\sin^2\frac{\theta}{2}+\pi\alpha\beta\sin\frac{\theta}{2}\left(1-\sin\frac{\theta}{2}\right)\right\}, \qquad (2\text{-}1)$$

where $\theta$ is the angle at which the incoming particle is scattered to its initial direction of motion, $\alpha$ is the fine structure constant and $\beta$ is the ratio of the particle's speed to the speed of light. $D_{e\text{-}n}$ is the distance of closest approach and is defined as the distance between the incoming electron and the nucleus when the kinetic energy of the incident electron has been entirely converted to potential energy:

$$D_{e-n} = \frac{Ze^2}{4\pi\varepsilon_o}\frac{1}{m_e v^2/2}, \qquad (2\text{-}2)$$

where $Z$ is the atomic number of the absorber atom, $e$ is the electronic charge, $\varepsilon_o$ is the permittivity of free space, $m_e$ is the rest mass of the electron and $v$ is the velocity of the incoming electron.

Under the small angle approximation, Eq. (2-1) is reduced to:

$$\left(\frac{d\sigma}{d\Omega}\right)_{e-n} = \frac{D_{e-n}^2}{\theta^4}. \tag{2-3}$$

Williams and Massey and Corben derived expressions akin to Eq. (2-1) for particles of spin 0 and 1, respectively which also reduce to Eq. (2-3) under the small angle approximation[2]. These expressions, as well as the Mott description of the electron-nucleus scattering cross-section, Eq. (2-1), all assume the Born approximation, a point nucleus and do not consider screening effects.

In actuality, Eq. (2-3) is only valid for a select span of deflections, those which are unaffected by the finite size of the nucleus and orbital electron screening. From Eq. (2-3) it may readily be observed that a singularity occurs when $\theta$ is set to zero. This singularity may be avoided by accounting for screening of the nucleus by orbital electrons. A point nucleus is characterized by a potential that follows an inverse relationship with the distance between the nucleus and the incoming electron. However, in the presence of orbital electrons, the potential will diminish more briskly as the electron-nucleus distance is augmented. The Thomas-Fermi potential provides an approximate description of screening effects[3]:

$$V(r) = \frac{Ze^2}{4\pi\varepsilon_o}\frac{1}{r}e^{-r/r_a}, \tag{2-4}$$

where $r$ is the distance between the incident electron and the nucleus and $r_a$ is the atomic radius. This latter parameter may be computed as[2]:

$$r_a = 0.885 r_H Z^{-1/3}, \tag{2-5}$$

where $r_H$ is the radius of the hydrogen atom derived from the Bohr model.

With the aid of the Born approximation, the Thomas-Fermi potential may be utilized to solve the Schrödinger equation and ultimately obtain a new expression for the electron-nucleus scattering cross-section which considers screening by orbital electrons:

$$\left(\frac{d\sigma}{d\Omega}\right)_{e-n} = \left(\frac{D_{e-n}}{4}\right)^2 \frac{1}{\sin^4\frac{\theta}{2}} \left\{1 + \left(\frac{\lambda}{4\pi r_a \sin\frac{\theta}{2}}\right)^2\right\}^{-2}, \tag{2-6}$$

where $\lambda$ is the deBroglie wavelength of the incoming electron. The Heisenberg uncertainty principle allows a minimum scattering angle, $\theta_{\min}$, to be defined. When the uncertainty in position, $\Delta x$, is approximately set to $r_a$, then it follows that $\Delta p \geq h/2\pi r_a$. We may then define:

$$\theta_{\min} = \frac{\Delta p}{p} = \frac{\lambda}{2\pi r_a}, \tag{2-7}$$

where $p$ is the momentum of the incident particle and $\Delta p$ is the uncertainty in momentum. The differential scattering cross-section is virtually uninfluenced by screening effects when $\theta >> \theta_{\min}$. However, if $\theta < \theta_{\min}$, screening significantly diminishes the scattering probability, therefore Eq. (2-6) should be employed. That equation reduces to a convenient form under the small angle approximation, unhampered by a singularity at $\theta = 0$:

$$\left(\frac{d\sigma}{d\Omega}\right)_{e-n} = \frac{D_{e-n}^2}{\left(\theta^2 + \theta_{\min}^2\right)^2}. \tag{2-8}$$

A maximum allowable scattering angle may be calculated in order to account for the effects of a nucleus of finite size. The nuclear charge may be imagined as clustered into a sphere of radius $r_{nuc}$. The nuclear radius is approximated as[2]:

$$r_{nuc} = 0.49 r_e A^{1/3}, \tag{2-9}$$

where $A$ is the mass number and $r_e$ is the classical electron radius.

A maximum permissible scattering angle, $\theta_{max}$ may then be derived in a fashion akin to that employed to obtain $\theta_{min}$ (Eq. (2-7)). In this instance, if $\Delta x$ is approximately set to $r_{nuc}$:

$$\theta_{max} = \frac{\lambda}{2\pi r_{nuc}}. \tag{2-10}$$

Consideration of the finite size of the nucleus has no impact on the scattering probability when $\theta << \theta_{max}$. Conversely, for $\theta > \lambda/2\pi\theta_{max}$, a swift fall in the scattering probability is observed when the finite size of the nucleus is accounted for.

Although Eq. (2-8) is a small-angle approximation, it effectively mimics Mott's relationship for electron-nucleus scattering (Eq. (2-1)) for even relatively large scattering angles[2].

#### 2.1.1.2 Radiative Collisions

As mentioned previously, a few percent of electron-nucleus interactions generate electromagnetic radiation in the form of bremsstrahlung photons. The bremsstrahlung energy spectrum includes all energies up to the maximum kinetic energy of the incident electron. In the case of an incident electron with an energy $E<<m_e c^2$, the corresponding bremsstrahlung photon will be emitted preferentially perpendicular to the direction of electron motion. Conversely, electrons whose energies significantly exceed the rest mass energy will tend to emit bremsstrahlung quanta in the forward direction. The average angle of bremsstrahlung emission in the case of higher energy electrons, $\theta_{brem}$, is expressed as[4]:

$$\theta_{brem} = \frac{m_e c^2}{E}. \tag{2-11}$$

It is obvious that Eq. (2-11) tends to zero as the electron energy $E$ tends to $\infty$, as expected.

Bremsstrahlung radiation may also be produced in a collision between a passing electron and an orbital electron. In this instance, the energy loss goes linearly with the atomic number of the absorber. However, the energy loss in the case of bremsstrahlung originating from an electron-nucleus interaction is proportional to the square of the atomic number. Therefore, radiative energy losses stemming from electron-nucleus bremsstrahlung are much more significant. The importance of radiative energy losses stemming from electron-electron interactions is manifested only at tremendous relativistic energies and for low atomic number target materials.

### 2.1.2 Hard Collisions

If the impact parameter has a value similar to that of the atomic radius, $b \sim r_a$, the incident electron will act on a single orbital electron. Provided that the passing electron possesses energy substantially greater than the binding energy of the orbital electron, the latter particle will be ejected and the atom will become ionized. The ejected electron may escape with sizeable kinetic energy, hence the term hard collision. Such an electron-electron collision may result in energy transfers of up to 50% of the kinetic energy of the incident electron. When the ejected electron is in possession of energy superior to some threshold $\Delta$, it is known as a $\delta$ ray and has enough energy to start a track of its own, carrying energy away from the site of its creation. Hard collisions are rare but induce such large energy transfers that they account for close to fifty percent of energy deposition in the medium.

Scattering derived from collisions between identical particles is expressed by the Møller cross-section. It is assumed that atomic electrons may be considered as free[1]:

$$\left(\frac{d\sigma}{d\Omega}\right)_{e-e} d\Omega = \pi D_{e-e}^2 (\gamma+1)\left[4(1-\eta^2)^{-2} - 3(1-\eta^2)^{-1} + \left(\frac{\gamma-1}{2\gamma}\right)^2 \left(1+4(1-\eta^2)^{-1}\right)\right] d\eta \cdot \quad (2\text{-}12)$$

The parameters $\gamma$, $\eta$ and $d\eta$ appearing in Eq. (2-12) may be respectively defined as:

$$\gamma = \left(1 - \frac{v^2}{c^2}\right)^{-1/2}, \tag{2-13}$$

$$\eta = \frac{2 - (\gamma + 3)\sin^2\theta}{2 + (\gamma - 1)\sin^2\theta} \tag{2-14}$$

$$d\eta = \frac{2(\gamma + 1)\sin\theta\cos\theta d\theta}{\left(\cos^2\theta + 0.5(\gamma + 1)\sin^2\theta\right)^2}. \tag{2-15}$$

The parameter $D_{e\text{-}e}$ is the distance of closest approach of the incident electron to the orbital electron with which the interaction occurs. Its definition is analogous to that of $D_{e\text{-}n}$, as related by Eq. (2-2):

$$D_{e-e} = \frac{e^2}{4\pi\varepsilon_o} \frac{1}{m_e v^2 / 2}. \tag{2-16}$$

Under the small angle approximation, the electron-electron scattering cross-section described by Eq. (2-12) is reduced to a format akin to that of the electron-nucleus scattering cross-section of Eq. (2-3):

$$\left(\frac{d\sigma}{d\Omega}\right)_{e-e} = \frac{D_{e-e}^2}{\theta^4}. \tag{2-17}$$

As in the formerly discussed case of electron-nucleus interaction, a singularity obviously occurs in the case of a zero scattering angle. A minimum scattering angle in regards to an electron-electron interaction, $\theta_{\min}^{e-e}$, may be defined in the manner previously described, leading to:

$$\theta_{\min}^{e-e} = \frac{\lambda}{2\pi r_{orb}}, \tag{2-18}$$

where $r_{orb}$ represents the orbital radius of the atomic electron involved in the interaction. As it happens, $r_a$ is a good approximation for $r_{orb}$, therefore $\theta_{\min}^{e-e}$ may be taken as $\theta_{\min}$, as computed by Eq. (2-7). Accordingly, an expression for the differential cross-section pertaining to an electron-electron interaction unhindered by the presence of a singularity may be defined in an analogous fashion to Eq. (2-8):

$$\left(\frac{d\sigma}{d\Omega}\right)_{e-e} = \frac{D_{e-e}^2}{\left(\theta^2 + \theta_{\min}^2\right)^2}. \tag{2-19}$$

### 2.1.3 Soft Collisions

If the impact parameter greatly exceeds the atomic radius, a soft collision is the consequent interaction type. The target atom reacts as a unit to the Coulomb force exerted on it by the incident electron. The response of the target atom may be excitation, during which an inner shell electron is transported to an outer shell, or ionization, the ejection of an orbital electron[4].

The excitation process only requires a few eV, therefore the energy loss of the passing electron is quite small. The atom only remains in the excited state momentarily and the electron concerned falls back into a lower state, usually emitting its surplus energy as a characteristic x-ray. On the odd occasion, the surplus energy is consumed in the production of Cerenkov radiation. This effect occurs when the velocity of the passing electron exceeds the phase velocity of light in a given medium. As fast electrons traverse the medium, it undergoes polarization. This polarization in turn triggers the traveling particle to release electromagnetic radiation. The dielectric constant of the material is a major player in the generation of Cerenkov emissions. However, surplus energy stemming from an excitation is only expended as Cerenkov radiation in a few percent of cases, making this phenomenon negligible for radiation dosimetry.

Enough energy may be redistributed to an electron uninvolved in a direct hit during a soft collision that the said electron is expelled from the atom. A particular quantum of energy is not requisite to produce ionization. The energy transferred to the orbital electron must simply be larger than the electron's binding energy. Any surplus energy transferred becomes the ejected electron's kinetic energy. The process just discussed is the basis for the creation of ion pairs; an ion pair being the expelled electron and the positively charged ion that remains once the electron has left the atom.

Such excitations and ionizations produce very little scattering of the incoming electron. An individual soft collision results in only a minute deflection, so that the incident electron travels in very nearly the same direction as prior to the collision. Although an individual soft collision results in only a tiny energy transfer, soft collisions are responsible for about fifty percent of the total energy transferred to the medium, since they are incredibly numerous.

## 2.2 Multiple Scattering

Scattering stemming from soft collisions is generally negligible, however hard collisions and nuclear Coulomb scattering create a multitude of small angle random deflections as the incoming electron passes through the medium. These deflections are spread about the direction of incidence in a symmetric fashion and the electron under consideration will emerge as angled to its initial direction after traversing a given thickness of medium. Thus, the mean square scattering angle is a measure of angular spread.

In the case of a single scattering event, the mean square scattering angle, $\overline{\theta_s^2}$, may be written as[5]:

$$\overline{\theta_s^2} = \frac{\int_0^{\theta_{max}} \theta^2 \left(\frac{d\sigma}{d\Omega}\right)_{eff} d\Omega}{\sigma_{eff}} = \frac{\int_0^{\theta_{max}} \theta^2 \left(\frac{d\sigma}{d\Omega}\right)_{eff} d\Omega}{\int_0^{\theta_{max}} \left(\frac{d\sigma}{d\Omega}\right)_{eff} d\Omega}, \tag{2-20}$$

where $\theta_{max}$ is the maximum scattering angle in the case of an electron-nucleus interaction, as defined by Eq. (2-10). This angle typically exceeds the maximum scattering angle for interactions occurring between an incident electron and an orbital electron. Nevertheless, electron-nucleus interactions contribute in vast majority to the effective cross-section, making this an acceptable choice for the upper limit of integration. In addition, the probability of large scattering angles is very small. $\left(\frac{d\sigma}{d\Omega}\right)_{eff}$ is the effective differential cross-section which accounts for both elastic nuclear scattering and hard collisions. This total differential cross-section is defined as:

$$\left(\frac{d\sigma}{d\Omega}\right)_{eff} = \left(\frac{d\sigma}{d\Omega}\right)_{e-n} + Z\left(\frac{d\theta}{d\Omega}\right)_{e-e}. \tag{2-21}$$

The presence of the atomic number in Eq. (2-21) accounts for the fact that there are $Z$ orbital electrons. $\left(\frac{d\sigma}{d\Omega}\right)_{eff}$ may be expressed in the same form as the individual cross-sections (Eq. (2-8) and Eq. (2-19)):

$$\left(\frac{d\sigma}{d\Omega}\right)_{eff} = \frac{D_{eff}^2}{\left(\theta^2 + \theta_{\min}^2\right)}, \tag{2-22}$$

where $D_{eff}$ is the effective distance of closest approach. By inserting Eq. (2-2) into Eq. (2-8) and inserting Eq. (2-16) into Eq. (2-19), and then inserting Eq. (2-8) and Eq. (2-19) into Eq. (2-21), the following expression for $D_{eff}$ may be obtained:

$$D_{eff} = \sqrt{Z(Z+1)}\frac{e^2}{4\pi\varepsilon_o}\frac{1}{m_e v^2/2}. \tag{2-23}$$

The mean square scattering angle with regard to a single scattering event may be found by using the expression provided by Eq. (2-22) in Eq. (2-20). The following result is obtained:

$$\overline{\theta_s^2} = \frac{\ln\left(1+\frac{\theta_{max}^2}{\theta_{min}^2}\right)+\left(1+\frac{\theta_{max}^2}{\theta_{min}^2}\right)^{-1}-1}{\frac{1}{\theta_{min}^2}-\frac{1}{\theta_{max}^2+\theta_{min}^2}}. \tag{2-24}$$

As mentioned previously, an incident electron typically engages in numerous scattering interactions. Such behaviour may be modeled statistically[5]. After an electron has traveled a given length, its net scattering angle is a statistical function of the single scattering events that occurred over that length. Central limit theorem statistics allow a mean square scattering angle pertaining to multiple scattering, $\overline{\theta^2}$, to be defined as:

$$\overline{\theta^2} = N\overline{\theta_s^2}, \tag{2-25}$$

where $N$ is the number of scattering events that arise in a given thickness of medium. $N$ may be computed using the effective cross-section for multiple scattering:

$$N = \frac{N_A}{A}\rho t \sigma_{eff}, \tag{2-26}$$

where $N_A$ is Avogadro's number, $\rho$ is the density of the medium and $t$ is the thickness of the layer of medium. The cross-section $\sigma_{eff}$ may be computed as the integral of the differential effective cross-section, provided by Eq. (2-20). The probability function describing the angle that an electron will possess after traversing a given thickness of absorber will be a Gaussian characterized by a variance equivalent to $\overline{\theta^2}$.

Initially, the mean square scattering angle rises in a roughly linear manner with the thickness of the absorbing medium[5]. However, beyond approximately one-third to one-half the value of the practical range, this parameter attains an equilibrium value of 0.6 square radians. Beyond this point, the width of the angular distribution remains constant and the electrons have achieved a state of total diffusion. Electrons with paths that suffer large deflections at the outset may be rapidly lost from the beam,

suggesting that the electrons remaining deeper within the medium are those whose initial paths were comparatively straight.

### 2.3 Scattering Power

Electron interactions with matter produce seemingly erratic paths through the medium. From a dosimetric point of view, an easily tabulated parameter is required that provides a simple description of electron scattering through the medium. Linear scattering power answers this need and is defined as[5]:

$$T = \frac{\overline{\theta^2}}{t}, \tag{2-27}$$

where $t$ is the thickness of the scattering medium. Mass scattering power describes the increase in mean square scattering angle per unit mass thickness:

$$\frac{T}{\rho} = \frac{1}{\rho}\frac{\overline{\theta^2}}{t}. \tag{2-28}$$

The advantage of this definition is that it eliminates scattering power dependence on material density. The mass scattering power may be computed via Eq. (2-28), making use of Eq. (2-24), (2-25) and (2-26). The following result is obtained:

$$\frac{T}{\rho} = \pi D_{eff}^2 \frac{N_A}{A}\left\{\ln\left[1+\left(\frac{\theta_{\max}}{\theta_{\min}}\right)^2\right]-1+\left[1+\left(\frac{\theta_{\max}}{\theta_{\min}}\right)^2\right]^{-1}\right\}. \tag{2-29}$$

For electrons with energies in the clinical range, the following formula provides an estimation of mass scattering powers[5]:

$$\frac{T}{\rho} = \frac{(E_s/E)^2}{\beta^4 X_0}, \tag{2-30}$$

where $E_s$ is a constant of value 21.2 MeV and $X_0$ is the radiation length, a parameter which varies with material. It is measured in g/cm$^2$ and has a value of 35.9 g/cm$^2$ for water[4]. A definition of radiation length which encompasses effects of atomic electrons[2]:

$$\frac{1}{X_0} = 4\alpha \frac{N_A}{A} Z(Z+1) r_e^2 \ln\left(183 Z^{-1/3}\right). \tag{2-31}$$

Werner suggested an alternate means of approximating mass scattering power[4]:

$$\frac{T}{\rho}(E) = CE^{-1.78}, \tag{2-32}$$

where $E$ is the electron energy and C is a constant dependent on the material of the absorber. The value of C is 4.525 for water.

## 2.4 Stopping Power

Radiation dosimetry demands information concerning the way electrons exhaust energy along their tracks as they move through a given material. The quantity 'stopping power' provides this information. Linear stopping power is defined as[5]:

$$S = \frac{dE}{dx} \tag{2-33}$$

where $dE$ is the amount of energy lost by an electron while traveling a length $dx$ through matter.

Mass stopping power, $S/\rho$, is a quantity that is frequently employed. It removes stopping power dependence on the density of the material with the exception of the polarization effect. Mass stopping power may be utilized to determine a mean range, $r_0$, for an electron of initial energy $E_0$[5]:

$$r_0 = \int_0^{E_0} \left( \frac{S(E)}{\rho} \right)^{-1} dE \,. \tag{2-34}$$

The continuous slowing-down approximation (CSDA) is ingrained in the definition of the mean path length provided by Eq. (2-34), hence $r_0$'s alternate name, the continuous slowing-down range. The CSDA assumes that energy is lost continuously along the entire electron track. Of course, energy loss actually occurs in discrete steps.

Regarding the calculation of absorbed dose, it is useful to split total mass stopping power into two components:

$$\frac{S_{tot}}{\rho} = \frac{S_{coll}}{\rho} + \frac{S_{rad}}{\rho}, \tag{2-35}$$

where $S_{coll}/\rho$ is the collisional mass stopping power, due to inelastic collisions that generate excitations and ionizations and $S_{rad}/\rho$ is the radiative mass stopping power which stems from electron-nucleus reactions that create bremsstrahlung photons. In the computation of absorbed dose, the energy deposited locally is of interest. Excitations and ionizations result in the absorption of energy lost from the incident electron close to the point of interaction. Bremsstrahlung photons carry the energy they receive relatively far from the interaction site. Therefore, collisional stopping power is the quantity closely linked to absorbed dose. Figure 2-1 displays collisional and radiative mass stopping power curves for water over a broad range of energies. Data was obtained from tables published in ICRU 35[5].

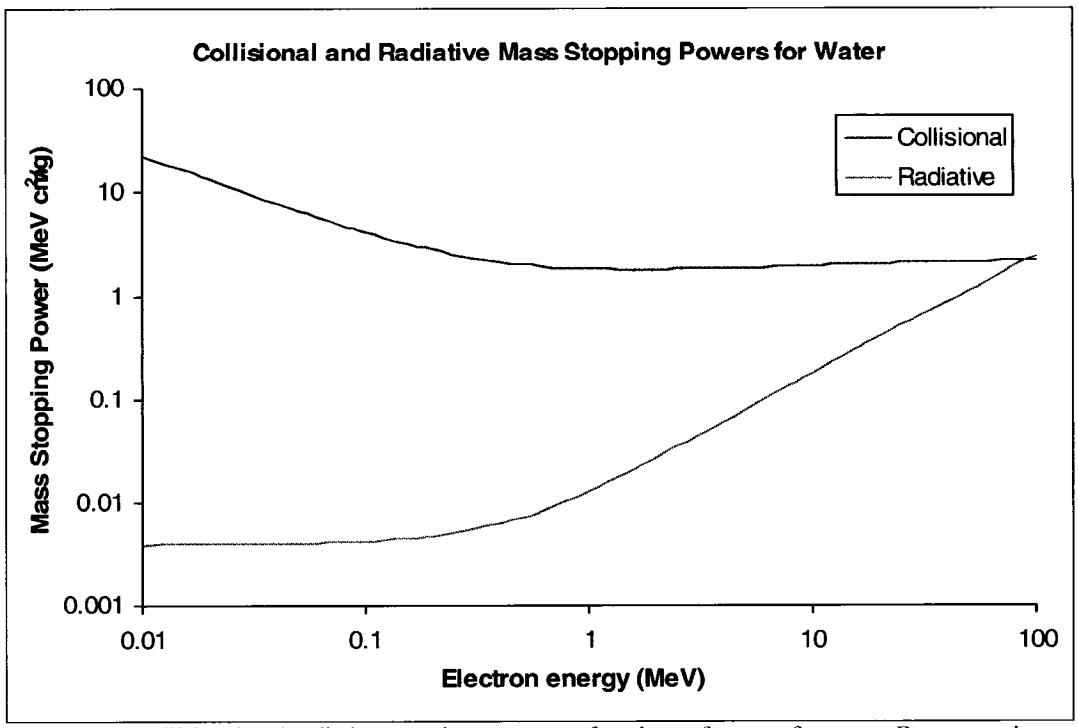


**Figure 2-1:** Collisional and radiative stopping powers as functions of energy for water. Data was taken from ICRU 35[5].

It may be noted in Figure 2-1 that, for water, radiative losses do not become comparable to collisional losses over the scope of energies employed in radiotherapy. The same is true for all biological materials, which are classified as having low atomic numbers. In the instance of a high atomic number material, such as lead, collisional and radiative mass stopping powers become comparable at significantly lower energies, approximately around 10 MeV[4]. Figure 2-1 also reveals that while collisional losses are minimized around 1 MeV, radiative losses increase once medium to high electron energies are achieved.

Bethe derived an expression for collisional stopping power for the case of heavy charged incident particles. A modified version of that expression corresponds to the collisional stopping power function when the incident particle is an electron[5]:

$$\left(\frac{S_{coll}}{\rho}\right)=\frac{2\pi N_A r_e^2 m_e c^2}{\beta^2}\frac{Z}{A}\left[\ln\left(\frac{\tau^2(\tau+2)}{2(I/m_e c^2)}\right)+F(\tau)-\delta\right], \tag{2-36}$$

where $\tau$ is the ratio of the kinetic energy of the incident electron to its rest mass, $I$ is the mean excitation energy and $F(\tau)$ and $\delta$ are correction factors. The presence of $F(\tau)$

accounts for quantum mechanical and relativistic effects while $\delta$ corrects for material density effects.

The calculation of absorbed dose focuses on energy that is deposited locally. Hence, when relatively large amounts of energy are transferred to secondary electrons, creating δ rays, energy will be absorbed in regions comparatively far from the initial site of interaction. In order to solely consider local energy deposition, an arbitrary energy threshold, Δ, may be defined[5]. When the primary electron energy losses lead to the production of δ rays of energy superior to a given Δ, these losses will be excluded from the stopping power calculation. This new form of stopping power is known as the "restricted stopping power".

## 2.5 Fermi-Eyges Theory and Parameterization of the Electron Beam

Fermi-Eyges theory is fundamentally a solution of the Boltzmann transport equation that expresses the penetration of an electron pencil beam as Gaussian. This description assumes multiple scattering and neglects the sporadic occurrence of large angle single scattering events. Consider depth to be directed along the $z$-axis and $x$ and $y$ to be the lateral coordinates. Deflections in the $x$ and $y$ directions may be regarded as independent. Azimuthal symmetry is a property of multiple scattering[6], implying that distributions in the $x$-$z$ and $y$-$z$ planes will be identical. The electron probability distribution function, $P$, describes the likelihood that a given electron will be situated between $x$ and $x+\Delta x$ and $\theta_x+\Delta\theta_x$ upon attaining a depth $z$. $x$ denotes the lateral displacement. $\theta_x$ symbolizes the scattering angle projected onto the $x$-$z$ plane and $\theta_y$ represents its projection onto the $y$-$z$ plane. The scattering angle, $\theta$, thus corresponds to $\left(\theta_x^2+\theta_y^2\right)^{1/2}$. Fermi stipulated that the probability function must sate the following equation[4,6]:

$$\frac{\partial P}{\partial z}=-\theta_x\frac{\partial P}{\partial x}+\frac{T}{4}\frac{\partial^2 P}{\partial \theta_x^2}, \tag{2-37}$$

where $T$ is the linear scattering power, as discussed in section 2.2. Fermi solved Eq. (2-37) ignoring electron energy loss[6]:

$$P(\theta_x, x, z) = \frac{2\sqrt{3}}{\pi T z^2} \exp\left[ -\frac{4}{T}\left(\frac{\theta_x^2}{z}\right) - \frac{3x\theta_x}{z^2} + \frac{3x^2}{z^3} \right]. \tag{2-38}$$

To reiterate, Eq. (2-38) denotes the probability that a particle will manifest a certain lateral displacement and a certain angular deflection at some depth $z$ when considering the $x$-$z$ plane. An identical solution, with all $x$'s substituted for $y$'s, pertains to the $y$-$z$ plane. Eyges later presented a solution to Eq. (2-37) which still assumed solely small angle scattering but took collisional energy loss into consideration by describing the electron energy as varying with depth[7].

Fermi-Eyges formalism led many investigators, such as Brahme et al.[8], to describe a generalized solution of the diffusion equation:

$$P(\theta_x, x, z) = \frac{\exp\left( -\dfrac{\overline{\theta^2}(z)x^2 - 2\overline{r\theta}(z)x\theta_x + \overline{r^2}(z)\theta_x^2}{\overline{\theta^2}(z)\overline{r^2}(z) - (\overline{r\theta}(z))^2} \right)}{\pi(\overline{\theta^2}(z)\overline{r^2}(z) - (\overline{r\theta}(z))^2)^{1/2}}, \tag{2-39}$$

where $\overline{\theta^2}(z)$ is the mean square scattering angle, as previously defined in section 2.2, $\overline{r\theta}(z)$ is the mean covariance and $\overline{r^2}(z)$ is the mean square radial spread. These parameters may be further defined as[5,8]:

$$\overline{\theta^2}(z) = \overline{\theta^2}(0) + \int_0^z T(z')dz', \tag{2-40}$$

$$\overline{r^2}(z) = \overline{r^2}(0) + 2\overline{r\theta}(0)z + \overline{\theta^2}(0)z^2 + \int_0^z (z - z')^2 T(z')dz', \tag{2-41}$$

$$\overline{r\theta}(z) = \overline{r\theta}(0) + \overline{\theta^2}(0)z + \int_0^z (z - z')T(z')dz', \tag{2-42}$$

where $\overline{\theta^2}(0)$, $\overline{r^2}(0)$ and $\overline{r\theta}(0)$ are correspondingly the initial values of the mean square scattering angle, the mean square radius and the mean covariance. Eq. (2-39) reduces to Eq. (2-38) when no energy loss is assumed and when the initial mean square scattering angle, the initial mean covariance and the initial mean square radius are all taken as zero.

In the case of a uniform medium and providing that the scattering power rises linearly with the thickness of material traversed, the mean square radius may be written as:

$$\overline{r^2}(z) = \overline{r^2}(0) + 2\overline{r\theta}(0)z + \overline{\theta^2}(0)z^2 + \frac{T(0)z^3}{3}\left(1 + \frac{\varepsilon_o z}{2}\right), \tag{2-43}$$

where $\varepsilon_o$ is the specific stopping power, defined as the total stopping power divided by the initial electron energy. This description of the mean square radius thus accounts for energy loss in an approximate manner.

The joint spatial and angular probability distribution, $P(\theta_x, x, z)$, described by Eq. (2-39), may also be expressed as a product of two Gaussians; one corresponding to the purely spatial component and the other characterizing the spatial variation of the angular component:

$$P(\theta_x, x, z) = \frac{\exp\left[-\dfrac{x^2}{\overline{r^2}(z)}\right]}{\sqrt{\pi\overline{r^2}(z)}} \frac{\exp\left[\dfrac{-(\theta_x - \theta_{x,p})^2}{\overline{\theta_c^2}}\right]}{\sqrt{\pi\overline{\theta_c^2}}}, \tag{2-44}$$

where $\theta_{x,p}$ signifies the most probable electron direction and $\overline{\theta_c^2}$ represents the angular spread about the most probable direction.

The most probable direction of electrons positioned at a distance $x$ from the central axis, $\theta_{x,p}$, is explicit in the exponent of the second factor in Eq. (2-44). This parameter may be evaluated as:

$$\theta_{x,p} = \frac{\overline{r\theta}(z)}{\overline{r^2}(z)} x \,. \tag{2-45}$$

It is evident from Eq. (2-45) that the most probable direction of electron motion will demonstrate a greater deviation from $\theta_x$=0 for a larger distance $x$ from the central ray or for a mean covariance of larger magnitude. Furthermore, Eq. (2-45) communicates a more lucid understanding of the mean covariance. Effectively, $\overline{r\theta}(z)$ indicates the extent to which electrons external to the central axis diverge. A positive mean covariance is particular to a divergent beam while a negative value denotes beam convergence. A mean covariance equal to zero implies that the direction of net electron motion is along the central axis.

The angular spread about the most probable direction, $\overline{\theta_c^2}$, may be of a value that differs from that of the beam as a whole, $\overline{\theta^2}(z)$. As follows from Eq. (2-44), $\overline{\theta_c^2}$ may be expressed as:

$$\overline{\theta_c^2} = \overline{\theta^2}(z) - \frac{\left(\overline{r\theta}(z)\right)^2}{\overline{r^2}(z)} \,. \tag{2-46}$$

A purely spatial and a purely angular distribution may be derived from Eq. (2-44) that are also Gaussian in nature. The former may be obtained by integrating the product of Eq. (2-44) and its $y$-$z$ plane counterpart over all angles $\theta_x$ and $\theta_y$, giving:

$$Q(x,y,z) = \frac{\exp\left(-\dfrac{x^2+y^2}{\overline{r^2}(z)}\right)}{\pi \overline{r^2}(z)} \,. \tag{2-47}$$

The solely angular probability distribution may be found in an analogous manner, producing:

$$R(\theta,z)=\frac{\exp\left(-\dfrac{\theta^2}{\overline{\theta^2}(z)}\right)}{\pi\overline{\theta^2}(z)}. \tag{2-48}$$

Ultimately, Fermi-Eyges theory provides a Gaussian description of the generalized distribution of an electron pencil beam incident upon a semi-infinite uniform medium. However, the accuracy of this representation is limited by the confines of small angle multiple scattering, which disregards large single scattering events and assumes infinite electron range. Consequently, underestimation of lateral scatter at shallow depths and exaggeration of the presence of electrons at greater depths will arise.

One limitation of Fermi-Eyges theory becomes apparent when concerned with non-uniform media. Consider a medium composed of layers of different materials. As previously discussed, the distribution function is influenced by the mean square radius, $\overline{r^2}(z)$. It is by the use of this parameter that Fermi-Eyges theory deals with heterogeneous media. Recalling Eq. (2-41), $\overline{r^2}(z)$ is a function of the initial values of the mean square radius, the mean covariance and the mean square scattering angle. It also demonstrates a dependence on the scattering power of the absorbing medium. As the electron beam enters a new layer of medium, Fermi-Eyges theory considers it as essentially being redefined, according to Eq. (2-41). The initial values of the mean square radius, the mean covariance and the mean square scattering angle as the beam comes to this layer of new material will be equivalent to the values of these parameters as the beam emerged from the previous layer. The scattering power employed in Eq. (2-41) will be that of the new material over the thickness of this new layer. However, Fermi-Eyges theory, being based on multiple scattering, has no means of describing the backscattering phenomenon that arises at interfaces between two materials. When an electron beam strikes a higher density material, a non-negligible fraction of electrons are scattered upstream, contributing dose to points at shallower depths. Clearly, Fermi-Eyges theory is not equipped to describe this occurrence.

## 2.6 References


1. Mott, N.F., Massey, H.S.W., *The theory of atomic* collisions, Claredon Press, Oxford, 1965.

2. Rossi, Bruno, *High energy particles*, Prentice-Hall, New York, 1952.

3. Scott, W.T., *The theory of small angle multiple scattering of fast charged particles*, Rev. Mod. Phys. 35, p. 256-257, 1963.

4. Klevenhagen, S.C., *Physics of Electron Beam Therapy*, Adam Hilger, Ltd., Bristol, 1985.

5. International Commission on Radiation Units and Measurement (ICRU), Report No 35, *Radiation Dosimetry: Electron Beams with Energies Between 1 and 50 MeV*, 1984.

6. Fermi, as quoted by Rossi, B., Greisen, K., *Cosmic ray theory*, Rev. Mod. Phys. 13, p. 262-309, 1941.

7. Eyges, L., *Multiple scattering with energy loss*, Phys Rev, 74, p. 1534-1535, 1948.

8. Brahme, A., Lax, I., Andreo, P., *Electron beam dose planning using discrete Gaussian beams: Mathematical background*, Acta Radiol Oncol, 20(2), p.147-158, 1981.

# Chapter 3

## The CadPlan Algorithm

For electron beam treatment planning, CadPlan uses a generalized pencil beam algorithm conceptualized by Lax and colleagues at the Karolinska institute in Sweden[1]. A broad beam is mimicked by the summation of numerous pencil beams, which fill the calculation grid. The basis of this algorithm is Fermi-Eyges theory, as discussed in the previous chapter. The shortcomings of Fermi-Eyges theory are counteracted in the CadPlan algorithm; each pencil beam is described by a summation of Gaussians, whose weighting factors are derived from a fit to Monte Carlo data. A reduction factor is also incorporated to account for range straggling. CadPlan Version 6.2, employed in this work, is fully three-dimensional and is designed to handle arbitrary field shapes and orientations and heterogeneities. This chapter will describe how CadPlan calculates a given dose distribution.

### 3.1 A Formula for Dose to a Point

Consider a monodirectional pencil beam, orthogonally incident upon a semi-infinite homogeneous phantom. Such beams boast dose distributions that, in the transverse ($x$ and $y$) planes, are close to Gaussian in nature[2]. Therefore, Fermi-Eyges theory may be applied to describe the angular and spatial distributions of electrons in the medium. Assume that electrons undergo solely small angle multiple scattering and that the $x$ and $y$ deflections are independent. The joint spatial and angular distribution will be the product of the individual distributions, both of which are Gaussian. The generalized solution will be Gaussian as well. Disregarded, however, are the few single large scattering events that do occur. The consequence is an underestimation of lateral scatter at shallow depths and an exaggeration of the presence of electrons deeper within the medium. For small field sizes, the resultant error may exceed 20 %[3].

For a single pencil beam, the radial dose distribution at a depth $z$ and a distance $r$ from the central axis, $D(r,z)$, may be described by a sum of weighted Gaussians[1]:

$$D(r,z)=\sum_{i=1}^{j}B_i(z)\exp\left(-\frac{r^2}{b_i(z)\overline{r^2}(z)}\right) \tag{3-1}$$

where $B_i$ and $b_i$ are the amplitude and width weighting factors, respectively and $\overline{r^2}$ is the mean square radius, or spatial spread, of the pencil beam. In his 1983 work, Lax[3] fit Monte Carlo data to a sum of three weighted Gaussians. Such an expression for an electron pencil beam was shown to dramatically reduce the error margin characteristic of the simple Gaussian model. CadPlan also employs a sum of three Gaussians in its description of pencil beams. The value of $\overline{r^2}(z)$ is computed recursively with the aid of Eq. (2-41).

The pseudo-Gaussian nature of electron pencil beams allows the distribution of a beam of finite extension to be readily computed by integration. For a field of size $A$, the dose to a given point $(x,y,z)$ may be expressed as[1]:

$$D(x,y,z)=\frac{P(z)\sum_{i=1}^{j}B_i(z)\iint_{fieldA}\Phi_{air}(x',y',z_p)\exp\left[-\frac{(x'-x)^2+(y'-y)^2}{b_i(z)\overline{r^2}\eta(z)}\right]dx'dy'}{\pi\overline{r^2}(z)\eta(z)\sum_{i=1}^{j}B_i(z)b_i(z)}. \tag{3-2}$$

Eq. (3-2) conveys that the dose to a point $(x,y,z)$ is the sum of the contributions from all pencil beams. The entire denominator of Eq. (3-2) is composed of normalization terms. $\eta(z)$ is a reduction factor, $P(z)$ is a large field central axis depth dose curve, and $\Phi_{air}$ denotes the electron fluence in air. These parameters appearing in Eq. (3-2) will be the subject of the following sub-sections of the chapter.

### 3.1.1 Parameters of the CadPlan Formula for Dose to a Point

#### 3.1.1.1 The Reduction Factor

The term $\eta(z)$ of Eq. (3-2) is an empirical reduction factor which serves to account for range straggling. The Gaussian approximation, derived from Fermi-Eyges

theory, assumes that no electrons are lost from the beam. In actuality, the range of an electron trajectory is finite. Hence, electrons scattered at larger angles have a smaller probability to attain profound depths due to increased path length. Consequent to the assumption that no electrons are lost from the beam, implicit in the Gaussian approximation, is an exaggerated presence of electrons at profound depths within the medium. This deviation from reality may be accounted for by the incorporation of $\eta(z)$, which approaches unity at shallow depths. The reduction factor may be written as[1,3]:

$$\eta(z) = \exp(-s^{12(1.5-s)}) , \tag{3-3}$$

where $s = \frac{0.95z}{R_p}$ . $R_p$ is the practical range and, as usual, $z$ represents depth.

### 3.1.1.2 The Central Axis Depth Dose Curve

The central axis depth dose curve, $P(z)$ in Eq. (3-2), acts as a scaling factor for the total of the contributions to a point at a given depth. $P(z)$ may be described as:

$$P(z) = P_{open}^{ref}(z_{eff})\left[\frac{VSD + z_{eff}}{VSD + z}\right]^2 , \tag{3-4}$$

where $VSD$ is the virtual source to reference plane distance. The virtual source is essentially an imaginary point from which the electron beam may be thought of as originating from. The CadPlan reference plane is the base of the applicator. $P_{open}^{ref}(z)$ represents the large open field central axis depth dose curve required as input by the algorithm. The effective depth, $z_{eff}$, comes into play only in the presence of heterogeneities. It may be defined as the thickness of water that produces energy loss identical to that generated by a given thickness of a given heterogeneity. The CadPlan algorithm computes this parameter as[1,4]:

$$z_{eff} = \sum_{j=1}^{n} t_j \frac{S_{tot,j}}{S_{tot,water}} , \tag{3-5}$$

where $t_j$ is the thickness of a layer $j$ of inhomogeneity and $S_{tot,j}$ and $S_{tot,water}$ are the total stopping powers of the inhomogeneity and water, respectively. The stopping power terms appearing in Eq. (3-5) should be evaluated using the mean energy at the surface. The concept of stopping power was introduced in Chapter 2. The effective depth is employed to scale heterogeneities along the fanline of the beam. The fanline is defined as a line traced from the virtual source to a given point in the irradiated medium. In Eq. (3-4), the squared term is an inverse square law correction which accounts for the change in virtual source to point distance consequential to the introduction of $z_{eff}$. In water, $P_{open}^{ref}(z_{eff})$ is simply $P_{open}^{ref}(z)$. To reiterate, in the instance of heterogeneities, the central axis input depth dose curve, $P_{open}^{ref}(z)$, is transformed into a function of the effective depth, $P_{open}^{ref}(z_{eff})$, as shown in Eq. (3-4), using Eq. (3-5).

### 3.1.1.3 The Fluence in Air

The CadPlan algorithm employs the fluence in air, $\Phi_{air}$, as a weighting factor, as evidenced from Eq. (3-2). This parameter helps to ensure an appropriate description of the penumbra region when concerned with an SSD other than the standard (100 cm)[4]. The fluence in air is computed for every pencil beam at the point of entry into the patient. The fluence in air may be expressed as[1,5]:

$$\Phi_{air}(x,y,z_p)=\frac{1}{2}\left[erf\left(\frac{r_1(x,y,z_p)}{\sqrt{\overline{r^2}(z_p)}}\right)+erf\left(\frac{r_2(x,y,z_p)}{\sqrt{\overline{r^2}(z_p)}}\right)\right], \tag{3-6}$$

where $z_p$ is the distance along the beam axis from the base of the applicator to the patient's surface, $r_1$ and $r_2$ are the distances to the field edges at the level of $z_p$ and $\overline{r^2}(z_p)$ is the spatial variance or mean square radius as related by Eq. (2-38), evaluated at the patient's surface. Figure 3-1 depicts the calculation technique employed to define the fluence in air:

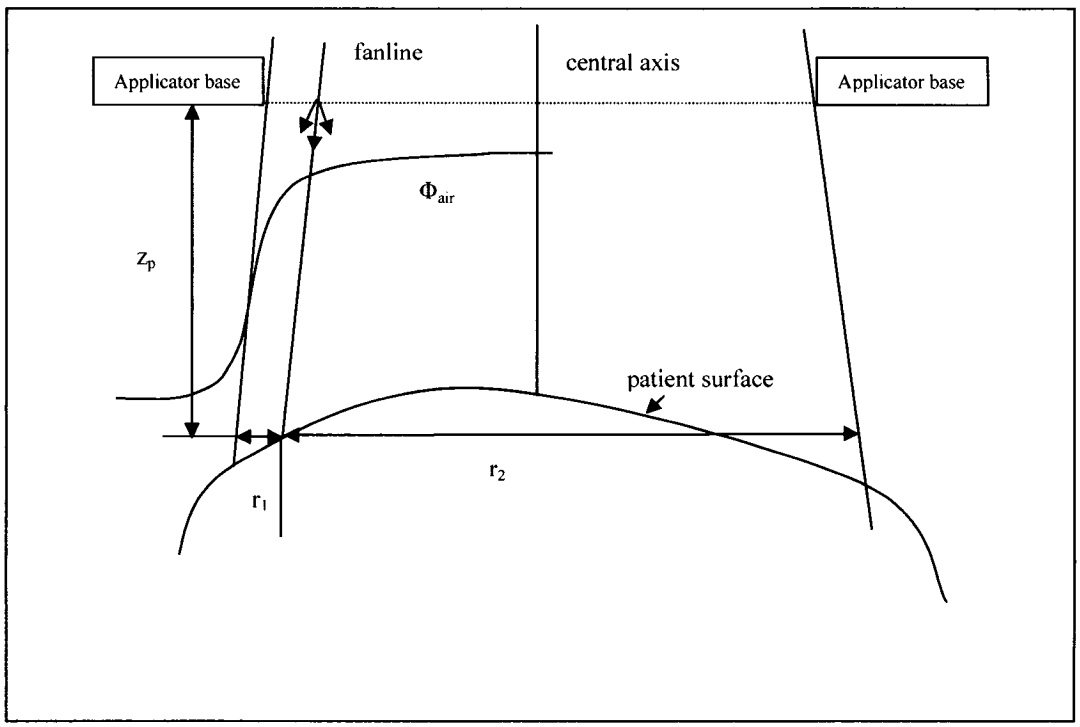


**Figure 3-1:** Description of the parameters employed in calculating the fluence in air.

The spatial variance at the patient's surface may be written as:

$$\overline{r^2}(z_p) = \overline{\theta^2}(0) z_p^2 + \frac{T_{air}}{3} z_p^3, \tag{3-7}$$

where $T_{air}$ denotes the scattering power of electrons in air, evaluated for the mean energy at the surface and $\overline{\theta^2}(0)$ represents the angular variance at the base of the applicator which constitutes the reference plane. This latter parameter serves as input information for CadPlan. The concept of scattering power was introduced in Chapter 2. Eq. (3-7) was obtained from Eq. (2-41) by considering $T_{air}$ to be independent of energy, an allowable assumption since the energy loss in air may be deemed negligible[6].

### 3.1.1.4 Tabulated Data Employed by the Algorithm Not Entered by the User

The formulae in the preceding sections are interspersed with various constants and parameters that are not among those entered by the user. The amplitude and width constants, $B_i(z)$ and $b_i(z)$, respectively appearing in Eq. (3-1) and Eq. (3-2) are

tabulated within the CadPlan program. Energy-wise, values of these parameters are present at steps of 1 MeV. Depth-wise, values for these constants appear at increments of $0.05/r_0$, where $r_0$ is the CSDA range of electrons, defined by Eq. (2-31). The values of these amplitude and width constants, reported in this same fashion, were taken from Lax's 1983 work[3]. As mentioned previously, CadPlan describes each pencil beam as a sum of three Gaussians. Therefore, an entry in the table for a given energy and a given depth will correspond to three sets of $B_i(z)$ and $b_i(z)$. However, pencil beams whose energies exceed 22 MeV are characterized by only one Gaussian and thus, for these cases, only one pair of these weighting factors is tabulated in CadPlan.

The other parameters required by the CadPlan algorithm but not entered by the user are presented in Table 3-1

| **Tabulated Algorithm Parameters** | |
|---|---|
| Mass Total Stopping Power | $\frac{S_{tot}}{\rho}$ |
| Mass Scattering Power | $\frac{T}{\rho}$ |
| Mean Range | $r_0$ |
| Ratio of Mean Range to Practical Range | $\frac{r_o}{R_p}$ |
| Specific Stopping Power | $\varepsilon_o$ |

**Table 3-1:** Parameters tabulated for use within the CadPlan algorithm.

The parameters listed in Table 3-1 are logged according to energy and grouped by tissue type: air, lung, fat, muscle and bone.

### 3.1.1.5 Data to be Entered by the CadPlan User

The CadPlan user must input several parameters which aim to provide an accurate description of the electron beam under consideration. All of the parameters in this category have either been alluded to in previous chapters or will be discussed in greater detail in the following chapter. Therefore, they will be treated here in only a cursory manner. Table 3-2 summarizes these parameters:

| Algorithm Parameters to be Entered by the CadPlan User | |
|---|---|
| Open field central axis depth dose curve | $P_{open}^{ref}(z)$ |
| Blocked field central axis depth dose curve | $P_{blocked}^{ref}(z)$ |
| Virtual source to reference plane distance | $VSD$ |
| Input mean square scattering angle at the reference plane | $\overline{\theta^2}(0)$ |
| Mean electron energy at the phantom surface | $\overline{E_0}$ |
| Normalization factor | $F$ |

**Table 3-2:** Parameters required by the CadPlan algorithm that must be determined by the user.

The parameters presented in Table 3-2 must be entered into a new CadPlan virtual machine for each energy desired. The normalization factor serves to make the peak dose of the reference field 100 %. The algorithm only requires a large field central axis depth dose curve in water as input data. No profiles or off-axis ratios are demanded. Hence, the width of a predicted distribution depends heavily on the value chosen for the mean square scattering angle at the base of the applicator. Ideally, the input parameters should be of values such that, for a given energy, satisfactory dose distributions are predicted for all field sizes. The blocked field depth dose curve provides information regarding electron transmission through applicator cut-outs, as well as describing the bremsstrahlung component of the dose delivered.

### 3.2 The Bremsstrahlung Component Model

The input PDD curves are treated such that the pure electron component is separated from the bremsstrahlung component. This latter portion is then modelled according to Sorcini[7]. Firstly, the total photon component is described as a sum of bremsstrahlung contributions originating from two distinct sources[1]:

$$D_x(z) = D_{x,p}(z) + D_{x,c}(z), \tag{3-8}$$

where $D_x(z)$ represents the entire bremsstrahlung component and $D_{x,p}(z)$ and $D_{x,c}(z)$ signify phantom-generated and contamination bremsstrahlung, respectively. Contamination bremsstrahlung includes all photons present in the beam that were

created via interactions with the linac head, applicator, cerrobend cut-outs and air traversed by the beam before reaching the phantom. Phantom-generated bremsstrahlung is modelled in the following manner:

$$D_{x,p}(z) = \frac{z}{R_{\max}} D_{x,p,\max} \text{ if } 0 \leq z < R_{\max}, \tag{3-9a}$$

$$D_{x,p}(z) = D_{x,p,\max} e^{-\mu_p (z - R_{\max})} \text{ if } x \geq R_{\max}, \tag{3-9b}$$

where $R_{\max}$ is the maximum range of electrons. The parameter $D_{x,p,\max}$, appearing in Eq. (3-9a) and Eq. (3-9b) is defined as:

$$D_{x,p,\max} = 0 \text{ if } 0 \leq \overline{E_0} < E_{x,0}, \tag{3-10a}$$

$$D_{x,p,\max} = \frac{(\overline{E_0} - E_{x,0})}{E_x} \text{ if } \overline{E_0} \geq E_{x,0}, \tag{3-10b}$$

where $E_{x,0}$ = 4.5 MeV and $E_x$ = 940 MeV for water[7] at the standard SSD. The value of $E_x$ is governed by the properties of the medium and is inversely proportional to the bremsstrahlung production. $E_{x,0}$ is the threshold energy below which phantom-produced bremsstrahlung is trifling, that is, falling below 0.5 % of the total dose. A value of 4.5 MeV for the threshold energy is suitable for all materials characterized by an effective atomic number between 1 and 30. The values of these constants were chosen empirically. The parameter $\mu_p$ is the appropriate attenuation coefficient. Attenuation coefficients pertaining to electron beam bremsstrahlung components considerably exceed those serving to describe x-ray beams of identical nominal energies[8]. Electron beam bremsstrahlung is softer than x-ray beams which have been hardened during their passage through the very thick flattening filter employed in the production of photon beams. Phantom-generated bremsstrahlung is represented as a percentage of the peak dose for an SSD of 100 cm. As evidenced from the preceding equations, the model just described depicts the early part of the phantom-generated photon curve as a linearly increasing function and the latter part as an attenuation curve. This description is typical as photons will continually be produced as a

consequence of electron interactions, until the electrons have exhausted their range. Subsequently, these photons will be attenuated by the medium.

The contribution of contamination bremsstrahlung to the total photon component normally exceeds that of phantom-generated bremsstrahlung. Furthermore, the largest constituent of contamination bremsstrahlung is by far photons originating from the linac head[8]. The CadPlan algorithm computes contamination bremsstrahlung as[1]:

$$D_{x,c}(z) = D_c(e^{-\mu_p z} - \nu e^{-\mu_e z}). \tag{3-11}$$

The parameters $\nu$ and $\mu_e$ are linked to the build-up region of the PDD curve; $\mu_e$ expresses the rate of build-up and $\nu$ is related to the surface dose[7]. $D_c$ is a scaling constant[1]. Both $\mu_p$ and $\mu_e$ are functions of the mean surface energy, $\overline{E_0}$. When concerned with larger field sizes, created either by larger cut-outs or larger applicators, more bremsstrahlung photons from the linac head will be present[8]. In addition, the CadPlan algorithm accounts for the transmission of bremsstrahlung photons through cut-outs, if present[9].

Ultimately, the bremsstrahlung contribution for a given set of conditions is added to the predicted electron dose distribution. Bremsstrahlung is considered to demonstrate a Gaussian distribution across the field. More specifically, the bremsstrahlung contribution at each point across the field is obtained by scaling the value of the input central axis blocked field depth dose curve to a Gaussian characterized by a value of 1.0 at the central ray and a value of 0.5 at the field edges[1]. Measured bremsstrahlung profiles[8] confirm the soundness of such a procedure. In the CadPlan algorithm, the bremsstrahlung constituent of the beam is never altered by inhomogeneity corrections.

### 3.3 Computer Implementation of the Algorithm

Earlier in the chapter, the dose to a point from a broad electron beam was depicted in Eq. (3-2) as involving the integral of the contributions from all points of

interest. In reality, the dose is calculated by the summation of a set of square pencil beams distributed throughout the field in a regular fashion[1]. Furthermore, pencil beams beyond the field boundaries are also incorporated in order not to neglect the ramifications of in-air scattering. The number of these additional pencil beams is derived from the initial mean square scattering angle and the applicator to surface distance. Pencil beams are of side length 2.5 mm at the standard treatment distance. Pencil beam dimensions are rescaled with distance from the reference plane. The CadPlan calculation grid always measures 160 columns by 112 rows. The greater the resolution desired, the smaller the dimensions of the grid pixels and the smaller the area of covered by the calculation grid. Square pixels of four side lengths are available: 1.25, 2.5, 5 and 10 mm.

The mean square scattering angle is only redefined at the point of intersection of a given fanline and the surface of the patient or phantom. It is at this point where the fluence in air is computed. The covariance and the mean square radius of the pencil beam at the point of patient entry are then set to zero.

If a pencil beam is situated in the blocked portion of the field, the weight of the beam is compared to the relative value of the blocked beam electron depth dose curve at the surface. Should the former be dwarfed by the latter, the blocked electron central axis depth dose curve is employed. In this way, block transmitted electrons are modelled.

The Image Utilities package allows the CadPlan user to create a three-dimensional electron density matrix which serves to mimic the phantom or patient. Free ray-tracing of the pencil beam fanlines through this matrix renders CadPlan capable of predicting dose distributions involving non-coplanar beams. The fanlines are ray-traced until the depth corresponds to the maximum range of the electrons. As shown by Eq. (3-1), each pencil beam is actually described by a sum of three Gaussians. The amplitude and width coefficients of each Gaussian, $B_i(z)$ and $b_i(z)$, serve to characterize the pencil beam. These coefficients are classified according to energy as well as depth. Heterogeneities are scaled to an effective depth, as previously discussed, and the appropriate amplitude and width coefficients are then selected. In this manner, the algorithm accounts for inhomogeneities. The values of these

amplitude and width coefficients are updated at set depth increments. In the instance of electron energies inferior to 10 MeV, the coefficients are re-evaluated every millimetre. The increments become progressively larger as electron energy rises, with increments of 3.5 mm for energies surpassing 35 MeV.

The calculation matrix is designed to correspond to a given plane of the patient. The contributions of dose from every pencil beam are then summed at the points of this grid. The integrals of the Gaussians have been replaced with a set of pre-calculated error functions in order to accelerate the calculation process. Once the electron dose distribution has been calculated, the bremsstrahlung component is calculated as described previously.

### 3.4 References


1. Varian, *CadPlan manual: External beam modelling physics v 6.0*, 1999.

2. Abou Mandour, M., Nüsslin, F., Harder, D., *Characteristic functions of point monodirectional electron beams*, Acta Radiol Suppl 364, p. 43-48, 1983.

3. Lax, I., Brahme, A., Andreo, P., *Electron beam dose planning using Gaussian beams : Improved radial dose profiles*, Acta Radiol Suppl 364, p. 49-59, 1983.

4. Brahme, A., Lax, I., *Absorbed dose distribution of electron beams in uniform and inhomogeneous media*, Acta Radiol Suppl 364, p. 61-72, 1983.

5. Huizenga, H., Storchi, P.R., *The in-air scattering of clincal electron beams as produced by accelerators with scanning beams and diaphragm collimators*, Phys Med Biol 32(8), p.1011-1029, 1987.

6. van Battum, L.J., Huizenga, H., *On the initial angular variances of clinical electron beams*, Phys Med Biol 44(11), p. 2803-2820, 1999.

7. Sorcini, B.B., Hyödynmaa, S., Brahme, A., *Quantification of mean energy and photon contamination for accurate dosimetry of high-energy electron beams*, Phys Med Biol 42 (10), p. 1849-1873, 1997.

8. Zhu, T.C., Das, I.J., Bjarngard, B.E., *Characteristics of bremsstrahlung in electron beams*, Med Phys 28(7), p.1352-1358, 2001.

9. Samuelsson, A., Hyödynmaa, S., Johansson, K.A., *Dose accuracy check of the 3D electron beam algorithm in a treatment planning system*, Phys Med Biol 43(6), p. 1529-1544, 1998.

# Chapter 4

## Experimental Methods

An assessment of CadPlan's aptitude for electron beam treatment planning necessitated numerous measurements under a variety of conditions. At the outset, a suitable detector, with which the majority of the required measurements would be performed, had to be chosen. The detector candidates and the selection process will be detailed in Chapter 5. Upon choosing an apposite measuring device, isodose curves were measured, intended as an evaluation standard for CadPlan-predicted dose distributions in a homogeneous phantom. Output factors were measured under the conditions of a uniform medium and orthogonal beam incidence. Also, PDD curves were measured for tissue substitute phantoms inlaid with simple heterogeneities in order to investigate CadPlan's ability to determine dose distributions under non-uniform conditions. CadPlan requires the input of several parameters, as discussed in the preceding chapter. Input values for the virtual source distance were measured for four of the energies studied. Corresponding values for the other energies were determined by estimation. The quality of CadPlan-predicted distributions depends on the required input PDD curves. In order to confirm the satisfactoriness of the build-up regions of measured PDD curves, these portions of the curves were verified by measurements in a solid water phantom with a thin wall parallel-plate chamber. CadPlan dose distributions were all created using the same grid size and hence the same resolution. The calculation grid was placed in approximately the same position for each distribution. The assessment of CadPlan's accuracy was based on a modified version of the acceptance criteria for electron beam treatment planning systems outlined by Van Dyk in 1993[1].

### 4.1 Instrumentation

All measurements were executed with the Elekta SL 25 linac, previously described in Chapter 1. In order to create field sizes inferior to that provided by the smallest available applicator, cerrobend cut-outs were employed. Initially, three detectors were investigated in order to determine which would be most suitable for the

numerous measurements necessitated by this work: an IC10[2] thimble chamber, an NACP[3] parallel-plate chamber and a GR-p BS[4] p-type silicon diode. The following chapter discusses why IC10 chamber was chosen to perform the required measurements and provides a detailed description of this chamber and the other detector types studied. The effective point of measurement for each of these detectors was taken into consideration during each measurement. The IC10 chamber is rounded and therefore the fluence varies over the surface of the chamber. In order to account for this fluence gradient, the effective point of measurement for this chamber type is positioned a distance of $0.5r$ upstream from the centre of the chamber, where $r$ is the radius of the chamber's air cavity[5]. The fluence is uniform on the surface of a parallel-plate chamber, thus the effective point of measurement is situated just inside the entrance window. The entrance window respective to the NACP chamber is 0.6 mm thick, hence the effective point of measurement for this detector is situated 0.6 mm downstream from the surface. Similarly, the diode's effective point of measurement is located 0.5 mm downstream from the surface of the detector. Many measurements undertaken with these detector types also employed a reference chamber taped to the electron applicator; an IC10 chamber in the case of the thimble and parallel-plate chambers and in the case of the diode a special reference chamber[4] particular to that detector. A fourth detector, the PTW Markus[6] chamber, was utilized for measurements involving tissue substitute phantoms. When this detector was employed, no reference detector was used as the number of monitor units administered was known. In addition, this parallel-plate chamber is characterized by a very thin reference window allowing any effective point of measurement to be disregarded.

The majority of measurements employed the WP700 Wellhöfer Dosimetrie[7] 3D scanning system. This system is comprised of a water tank of dimensions 60x60x60 $cm^3$ which includes a motorized arm, an electrometer and a hand controller attached to the tank. A detector may be affixed to the motorized arm and thus record data as it moves through the volume in a desired direction. The volume through which the detector may actually move is 48x48x48 $cm^3$. The position of the detector may be determined by either the corresponding WP700 computer or by the hand controller. Scanning speeds up to 15 mm/s are offered. No scans were acquired at speeds above 5.13 mm/s in order to avoid water perturbation which could lead to noisy readings. A scanning speed of 2.56 mm/s was employed to acquire all PDD curves and small field

beam profiles. The Wellhöfer user must assign limits that define the volume in which the detector is desired to travel. This was done with the aid of the hand controller. Similarly, the positions of the water surface and isocentre must be assigned. A source to surface distance (SSD) was determined with the mechanical pointer. The diode and parallel plate detectors were placed with their faces flush with the surface of the water. The thimble chamber, however, was positioned such that it was only half-submerged. The WP700 program allows effective points of measurement to be accounted for. The position of the isocentre was determined with the aid of the wall lasers and the mechanical pointer. This position was verified and adjusted, if necessary, by the central axis (CAX) check provided by the WP700 program. A Wellhöfer Dosimetrie CU 500E electrometer was utilized during all measurements involving the water tank. Prior to data acquisition, the detector was descended to the nominal depth of dose maximum ($d_{max}$) and both the field and reference electrometer gains were adjusted until they both approximated 100 %. Photograph 4-1 depicts an experimental set-up typical of this work.

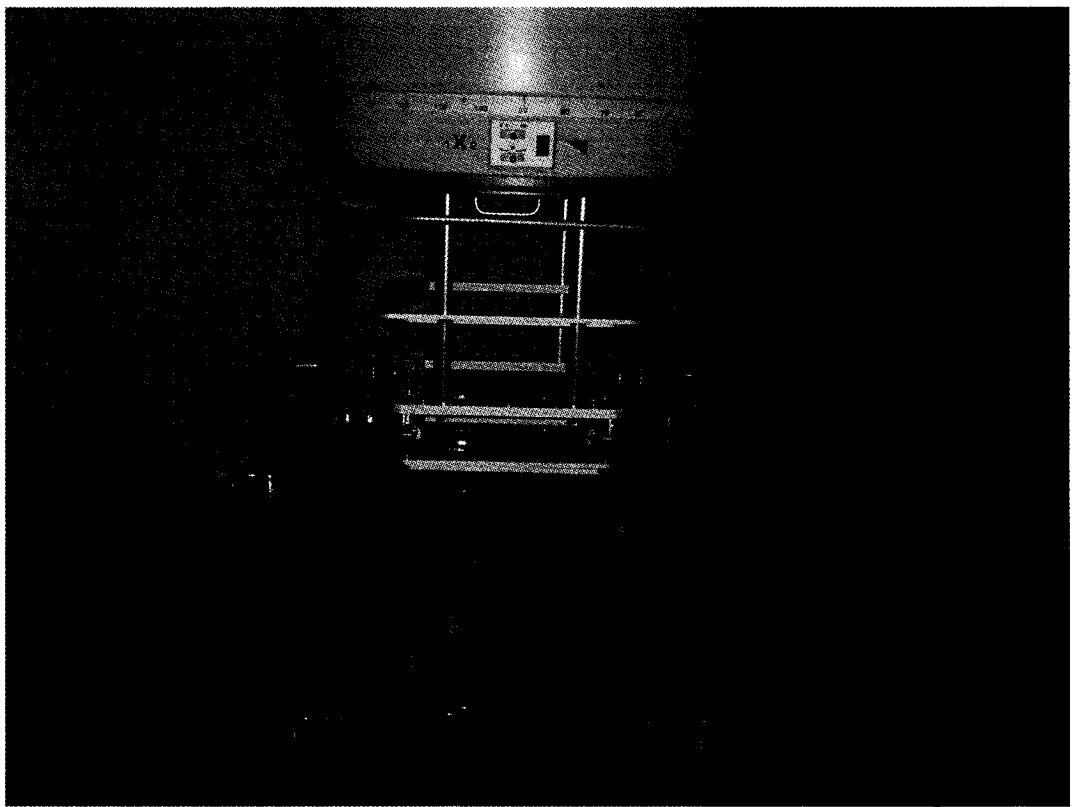

**Photograph 4-1:** Wellhöfer tank pictured with the Elekta SL 25 linac head with 25x25 $cm^2$ applicator attached. Both the measuring and the reference detectors shown here are IC10 chambers.

Solid Water™ (RMI Inc.)[8], an epoxy-based water or tissue substitute, was employed in several experiments. The substance is created from resins or powders containing carbon, nitrogen, oxygen, calcium and chlorine. Solid Water™ slabs of varying densities serve to mimic many biological materials. Water, lung and bone slabs were utilized in this work. These materials have densities of 1.000, 0.292 and 1.707 g/cm$^3$, respectively. Solid Water™ phantoms of desired characteristics were created from slabs of varying thickness. Special slabs, 2 cm thick, in each of the three materials employed, are each fashioned with a cavity in which the PTW Markus chamber was placed while the necessary measurements were performed. The electrometer utilized for these measurements was the Keithley 35040 Therapy Dosimeter[9]. Surface measurements were performed with a very thin acrylic sheet, of thickness 0.47 mm, placed over the top of the phantom and detector. As mentioned in Chapter 1, the radiation sensitivity of the skin only begins beyond the outermost layer.

### 4.2 Conversion of Depth Ionization Curves to Depth Dose Curves

Conversion of depth ionization curves to depth dose curves in water was executed according to Burns et al.[10] using the following relationship:

$$\left(\frac{L}{\rho}\right)_{air}^{water}(d_{50},z)=\frac{a+b(\ln d_{50})+c(\ln d_{50})^2+d(z/d_{50})}{1+e(\ln d_{50})+f(\ln d_{50})^2+g(\ln d_{50})^3+h(z/d_{50})}\,, \tag{4-1}$$

where a=1.0752, b = -0.50867, c=0.08867, d=-0.08402, e=-0.42806, f=0.064627, g=0.003085 and h=-0.12460. $d_{50}$ is the depth at which the dose has fallen to 50 % of its maximum value and $z$ represents depth. $d_{50}$ (in centimetres) may be obtained from $I_{50}$, the depth of 50 % ionization, via[5]:

$$d_{50}=1.029I_{50}-0.06\text{, if } 2\le I_{50}\le 10 \text{ cm, or} \tag{4-2a}$$

$$d_{50}=1.059I_{50}-0.37\text{, if } I_{50}>10 \text{ cm.} \tag{4-2b}$$

Burns established that if $0.02 \le z/d_{50} \le 1.1$, Eq (4-1) generates a maximum deviation of 1 % when compared to Monte Carlo-derived data. However, it was

reported, again by Burns, that if the upper limit of $z/d_{50}$ is raised to 1.2, errors of up to 1.7 % may arise. Burns did not provide discrepancies in the case where $z/d_{50}$ is superior to 1.2.

In this work, it was deemed necessary to substantiate where Eq. (4-1) breaks down. The stopping power values provided by this formula were compared to those tabulated by Berger[11]. For energies spanning 4-20 MeV, it was confirmed that, up until $z/d_{50}$ =1.2, discrepancies between the stopping power ratios calculated with Eq. (4-1) and those published by Berger were well below 1.7 %. Furthermore, outstanding agreement between these two data sets was noted up to and including $R_p$, the practical range. It was beyond the practical electron range where Eq. (4-1) was shown to degenerate. This finding is logical as no electrons remain beyond that point, eliminating the need for conversion and thus the need for Eq. (4-1) to function. Values of $z/d_{50}$ that very significantly exceed 1.2 were employed in Eq. (4-1). Such values obviously correspond to depths well beyond $R_p$. In these cases, Eq. (4-1) generated stopping power ratios that were truly inconsistent with Berger's values. Absurd stopping power ratios, such as negatives values, were even seen in some cases. However, if $z/d_{50}$ is greater than 1.2 but $z$ is less than or equal to the practical range, Eq. (4-1) still behaves in a satisfactory manner. For example, consider a 4 MeV large field beam. In this case, the practical range corresponds to $z/d_{50}$ = 1.3. A discrepancy of only 0.7 % in the stopping power ratio exists at this point with respect to Berger.

Interestingly, a plot of $d_{50}$ and $R_p$ values, both expressed in centimetres, obtained from PDD curves measured in this work, reveals the linear relation:

$$R_p = 1.18 d_{50} + 0.26 . \qquad (4\text{-}3)$$

Over the clinical range of energies, Eq. (4-3) allows the practical range to be roughly approximated as $1.2 d_{50}$, corresponding to the Burns cut-off for Eq. (4-1).

One of the most advantageous aspects of Eq. (4-1) is that it allows the determination of mean energy as a function of depth to be circumvented. Although sanctioned by the AAPM[12], the application of Harder's equation (Eq. (1-2)) to mean

energies may lead to very significant errors. Ding et al. compared Monte Carlo-calculated mean energies to those obtained using AAPM protocol[13]. Large discrepancies were observed. For example, in the instance of a 10 MeV beam, the mean energy at $d_{max}$ found using Harder's equation was overestimated by 26 % with respect to the value obtained using Monte Carlo. Furthermore, Eq. (1-3) also acts as the source of some error. The relationship between the mean energy at the surface and $d_{50}$ is influenced by the presence of scattered low-energy electrons, a beam component that varies appreciably between different beams from different accelerators. These differences make it impossible for a universal equation such as Eq. (1-3) to ensure extremely high accuracy for all conditions, for all beams, from all accelerators.

## 4.3 Water Tank Measurements

### 4.3.1 Choice of Detector

Measurements aiding to determine which detector type should be employed to acquire the large set of data demanded by this project were all performed in the water tank. Central axis depth ionization curves were obtained by executing scans along the depth direction. Profiles in a direction orthogonal to the depth direction were measured at desired depths. A 10x10 $cm^2$ applicator was utilized and smaller field sizes were created with cerrobend cut-outs. Energies of 4, 8, 12 and 20 MeV were employed in this set of measurements. A detailed description of the measurements pertaining to the choice of detector and their results are the subject of the following chapter. Ultimately, the IC10 chamber was chosen.

### 4.3.2 Measurements Designed to Verify CadPlan in a Homogeneous Medium

The primary task of this work was to verify CadPlan's ability to predict dose distributions when the irradiated medium was of a uniform nature. The necessary isodose distributions were obtained by measuring, for each condition under study, profiles in a direction perpendicular to depth and a central axis depth ionization curve. The latter was then converted to a PDD curve using Eq. (4-1). The profiles were not converted since they would be scaled to the central axis PDD curve. Furthermore, the stopping power variation in the transverse planes is unknown, and so it was assumed

to be constant. The number of profiles constituting a given distribution depends on the criteria the user enters into the Wellhöfer program. In order to ensure a complete representation of a given distribution, it was stipulated that a profile should be acquired at least as often as 2 cm depth is traversed and also every time the dose gradient attains a value of 5 %/mm or greater. Firstly, data was gathered for various field size and energy combinations with an SSD of 100 cm and a zero gantry angle. The Elekta SL 25 accelerator offers nine electron energies, all of which were utilized in this work. These energies have nominal values of 4, 6, 8, 10, 12, 15, 18, 20 and 22 MeV. All of the available applicators were also employed. These provided field sizes of 6x6, 6x10, 6x14, 10x10, 14x14, 8x16, 10x20, 20x20 and 25x25 $cm^2$. The collimator was usually set to 90° but when a rectangular applicator was employed, a second set of data was recorded with the collimator set to 0°. This procedure allowed fields of dimension 10x6, 14x6, 16x8 and 20x10 $cm^2$ to also be acquired.

CadPlan requires that a large open field PDD curve and a large blocked field PDD curve be entered for every energy desired. A field size of 20x20 $cm^2$ was chosen since this applicator size is the reference field at HMR. The blocked field PDD curve was achieved by inserting a cerrobend plate into the standard 20x20 $cm^2$ applicator.

Next, measurements aiding to verify CadPlan's aptitude for predicting dose distributions involving SSDs ranging from 98 to 102 cm were required. Energies of 4, 8, 12 and 20 MeV and field sizes of 6x6 and 20x20 $cm^2$ were employed.

It was also desired to examine CadPlan's ability to generate dose distributions involving an angled gantry. Energies of 4, 8, 12 and 20 MeV were used in this experiment. Again, only two field sizes were studied: 6x6 and 20x20 $cm^2$ created with the standard Elekta applicators. In the case of the 6x6 $cm^2$ applicator, angles of 20° and 40° were tested. When the 20x20 $cm^2$ applicator was employed, gantry angles of 10° and 20° were used. The maximum angle tested depended on how far the gantry could be rotated before the applicator would touch the water.

### 4.3.3 Measurement of the Virtual Source Distance

CadPlan requires that a virtual source distance (*VSD*) be entered for each nominal beam energy. This parameter was measured for 4, 12 and 20 MeV and for field sizes 6x6 $cm^2$, 10x10 $cm^2$ and 20x20 $cm^2$, each created with the respective standard applicator. For the purpose of this work, the *VSD* was considered to be equivalent to the effective SSD, discussed in Chapter 1. Khan's method was employed to acquire the necessary data and was previously described in detail. As stipulated by the method, ionization measurements were performed at the nominal $d_{max}$, depth of dose maximum, with varying distances between the base of the applicator and the phantom surface (air gap distances). The measurements were executed using the Wellhöfer water tank and its associated electrometer. One hundred monitor units were given. The necessary pressure and temperature correction was performed. A plot of the square root of the ratio of the ionization measured without a gap and the ionization measured with a given gap versus gap distance was drawn. The slope of this graph was then found and Eq. (1-7) was used to find the *VSD*. As mentioned in Chapter 1, the jaws of the Elekta SL 25 assume different positions as different applicators are fitted to the linac head. Also, different applicator sizes create varying amounts of scatter. Therefore, it was expected that the *VSD* would vary depending on which applicator was used for a given energy.

Although much variation in the value of the *VSD*, for a given energy, is observed between small field and large field applicators, only one *VSD* may be entered into CadPlan per energy. Values closer to those obtained for large fields were typically used as the required input *VSD* since the reference field is of dimensions 20x20 $cm^2$. As *VSD*s were only measured for three out of the nine energies, the remaining values were determined by estimation. The impact of the *VSD* on the predicted distribution will be addressed in Chapter 6.

### 4.3.4 Measurement of Output Factors

Output factors are employed clinically to relate the dose at $d_{max}$ particular to a given field to that of the reference field. Experimental determination of output factors involved measuring the dose at $d_{max}$ of a given field as well as the dose at $d_{max}$

respective to the reference field. The output factor is the quotient of the two values. Measurements were carried out with the Wellhöfer Dosimetry System and the IC10 chamber. Pressure and temperature corrections were applied. Output factors were experimentally determined for all available applicators. In addition, cut-out factors were measured that related the peak dose of a field created with a cerrobend cut-out to the peak dose of the standard field for the same applicator. Circular cut-outs of diameters 2, 3, 4, and 10 cm were employed with the 10x10 $cm^2$ applicator.

### 4.4 Measurements in Solid Water™

#### 4.4.1 Simple Heterogeneities

Solid Water™ phantoms were used to model simple heterogeneities. Slabs of material simulating lung of thickness 3 cm or 7 cm were positioned at depth of dose maximum, depth of 80% dose and depth of 50 % dose where these depths correspond to PDD curves measured in a water phantom. In a similar fashion, slabs simulating bone of thickness 0.5 cm or 3 cm were placed at the same depths. Percent depth dose curves were measured for each geometry using a PTW Markus chamber. Each data point along the measured ionization curves was the average of three measurements, corrected for temperature and pressure. Before Eq. (4-1) was used to convert this data to dose, the presence of the heterogeneities had to be accounted for by computing the effective depth, $z_{eff}$. This parameter provides the thickness of water that would produce the same amount of energy loss as the heterogeneity. Considering a given thickness of a low density material, such as lung tissue, less water would be required to obtain the same ionization. Conversely, a greater amount of water would be necessary to replace a given thickness of a higher density medium, such as bone. In this work, the coefficient of equivalent thickness (*CET*) method was employed to obtain the necessary effective depths. This method assumes that the attenuation induced by a given thickness $t$ of a heterogeneity is matched by a thickness of water ($t$ x *CET*), where *CET* is the ratio of the electron densities of the heterogeneity and water. The effective depth may therefore be calculated as[14]:

$$z_{eff} = z - t(1 - CET). \tag{4-4}$$

The parameter $z_{eff}$ is then applied in Eq. (4-1) to obtain the appropriate stopping power ratios. Considering a region of heterogeneity, Eq. (4-1) leads to the dose in a small mass of water surrounded by the material of the inhomogeneity. The true dose to such a point demands further multiplication by the ratio of stopping power of the medium concerned to that of water. That procedure was neglected in this work because CadPlan omits that step.

### 4.4.2 Measurement of the Build-Up Region

The quality of the dose distributions predicted by CadPlan depends heavily on the quality of the large field PDD curves entered. Thimble air ionization chambers such as the IC10 are known to be less accurate while measuring in the build-up region than beyond the peak dose. In order to evaluate the satisfactoriness of the build-up regions acquired with the IC10 chamber, build-up region measurements in Solid Water™ with the parallel-plate PTW Markus chamber were performed. Firstly, an entire PDD curve was measured using Solid Water™ slabs (all of which simulated water, no heterogeneities were present) to verify that the two measurement techniques were indeed comparable. The complete PDD curve was obtained with an energy of 12 MeV and a field size of 20x20 $cm^2$. These parameters were selected because the 20x20 $cm^2$ standard applicator constitutes the reference field and 12 MeV is mid-range among the energies considered in this work. Good agreement was observed between the two curves. Build-up regions were then measured for field sizes of 20x20 $cm^2$ and 6x6 $cm^2$ using nominal beam energies of 4, 12 and 20 MeV. These measurements essentially served as a spot check. Should the results have been unfavourable, the build-up regions of the input PDD curves measured with the IC10 chamber would have been replaced by those measured in Solid Water™. Klevenhagen confirms the acceptability of measuring various portions of the PDD curve in different media with different detectors. However, the build-up regions obtained with the two measuring techniques demonstrated accordance to within 2.5 %. These results demonstrate that the IC10 chamber is suitable to provide the complete PDD curves to be entered into CadPlan. In fact, CadPlan is known to be somewhat unreliable in the build-up region, making discrepancies such as these negligible.

### 4.5 Configuration of CadPlan

CadPlan requires that a virtual machine be created for each energy desired. The user must enter the name of the treatment unit and specify electrons as the radiation type. Next, the source to phantom (equivalent to the SSD), source to axis and collimator to skin distances must be defined. The two former were set to 100 cm. The latter was set to 5 cm, the distance between the end of an Elekta applicator and the surface with an SSD of 100 cm. The user must then indicate whether blocks should be allowed and whether a multileaf collimator (MLC) will be present. The affirmative was selected in response to the question of blocks but the presence of the MLC was negated since MLCs are not utilized for electron treatments. Furthermore, as this work focuses on electron beams, all fields required only regular jaw positions, characterized by the given applicator and energy combination. The next parameter to be entered is the depth interval between the points that will be entered to define the required input open and blocked field PDD curves. The number of points that may be entered per curve is limited to eighty. Virtual machines simulating energies spanning the lower end of the clinical spectrum were given PDD measurement intervals equal to 0.1 mm, making the maximum length of the input PDD curves 7.9 cm. This choice allows for good definition of the sharper build-up regions of low energy curves. Furthermore, the precipitous fall-off regions of such curves quickly lead to insignificant doses, rendering added length superfluous. An interval value of 0.2 mm was employed for higher energy virtual machines. The user must then set the remaining parameters which actually define the electron pencil beam of that energy. These parameters were listed in Table 3-2. The first of these is the mean square scattering angle, which, as described in Chapters 2 and 3, essentially defines how CadPlan-calculated isodose curves balloon. Varian suggested values for this parameter for various energies but it was quickly discovered that much higher values would be required to match CadPlan dose distributions to the data acquired from the Elekta SL 25. The correct values were determined by trial and error. The next pencil beam parameter to be entered is the mean energy at the surface, $\overline{E_0}$, which was determined using Eq. (1-3). The parameter $d_{50}$, required by this equation, was obtained for each energy from the 20x20 $cm^2$ open field PDD curve that served as the input curve for CadPlan. Another pencil beam parameter is the virtual source distance (*VSD*). As described earlier in this chapter, the

*VSD* was measured for a few energies and values for the remaining energies were estimated. The last parameter figuring among this group is the normalization factor whose function is to ensure that a dose of 100 % occurs at $d_{max}$ for the reference field. The user must first set this parameter equal to one and then compute the dose distribution for the reference field. The normalization factor, $F$, may then be approximated by the following equation:

$$F = \frac{D_{20x20} - D_{x,max}}{100 - D_{x,max}}, \tag{4-5}$$

where $D_{20x20}$ is the maximum central axis dose for the reference field (the value of $D_{20x20}$ will lie between 800 and 1000) and $D_{x,max}$ is the dose value of the blocked field curve at $d_{max}$. The value of $F$ obtained from Eq. (4-5) should then be entered into CadPlan. It should be verified that, for the reference field, $F$ gives 100 % at $d_{max}$. Any slight adjustments required may be done by trial and error. The CadPlan user must also define the treatment unit limits such as the collimator, gantry and table angles as well as the table height. CadPlan offers an electron field size monitor unit table, into which the user could enter values that would force the maximum central axis dose to be 100 % for any field size. For the purpose of this work, however, all values in this table were set to one. As aforementioned, one large open field PDD curve and one large blocked field PDD curve must be entered. The user may type in the values of the individual points or use a digitizer. The former method was adopted in this work. The user must then select the command to "complete" the PDD curves. This command essentially triggers the algorithm discussed in Chapter 3 which separates the pure electron component from the bremsstrahlung component of the open field PDD curve.

CadPlan's image utilities package was employed to create synthetic phantoms which serve as the media through which the desired dose distributions would be calculated. Almost all of the phantoms were cubes of side 30 cm. A larger phantom was required when concerned with a field size of 25x25 $cm^2$ as the width of the field exceeded the width of the phantom at a fairly shallow depth. In that case, the phantom's side measured 36 cm. Homogeneous phantoms, which served to model the Wellhöfer tank, were easily created by choosing the desired shape of the phantom and

the dimensions. The density of water was automatically selected. In order to mimic Solid Water™ phantoms formed of heterogeneous slabs, the phantom outline and regions of heterogeneity were digitized. The appropriate densities were entered for the body (water) and the region of inhomogeneity.

When preparing CadPlan to compute a given dose distribution, the collimator and gantry angles were set to the values selected during measurement. The field size provided by the applicator is defined at 95 cm. The CadPlan user must enter the field dimensions at the source to surface distance specified during the configuration of the virtual machine for that energy, which was consistently the standard 100 cm. Therefore, the input field dimensions were scaled accordingly. When necessary, blocks were added to define the field using CadPlan's autoblock function which allows the user to choose a regular block shape (circular cut-outs were used in this work) and enter the desired radius. Finally, the size and placement of the calculation grid had to be determined. The placement and size of the calculation grid makes a slight but noticeable impact on the predicted distribution. While comparing CadPlan distributions with measured distributions, such an effect is negligible. Conversely, even minor grid resizing and repositioning may exert a significant effect on output factors, where one or two percent become important. Therefore, while calculating output factors for a given energy, the grid was positioned for the reference field and not moved until all the output factors for that energy had been determined. Instead of creating a new plan for each applicator, the normalization of the previous plan was removed and the field size was altered, allowing the grid to remain immobile. This procedure circumvented the inclusion of extra error in CadPlan's calculation of output factors.

### 4.6 Acceptance Criteria

In order to determine whether or not CadPlan's electron beam treatment planning capabilities were adequate for clinical implementation, a set of acceptance criteria had to be established. The tolerances adopted in this work are a slightly modified version of those specified by Van Dyk in 1993. Table 4-1 presents these tolerances:

| Acceptance Criteria for Electron Beam Treatment Planning | |
|---|---|
| **Region** | **Tolerance** |
| *Homogeneous Phantom* | |
| Central ray | ± 1 mm |
| Profiles: low gradient | 4 % |
| Profiles: large dose gradient (>30 %/cm) | ± 2 mm |
| *Inhomogeneities* | |
| Central ray | ± 1 mm |

**Table 4-1:** Acceptance criteria used to evaluate CadPlan's satisfactoriness in terms of clinical implementation.

The Van Dyk tolerance for central axis PDD curves in regards to a homogeneous phantom was 2 %. This criterion was rejected as unreasonable, especially for low energy beams. Error in large dose gradient regions is customarily defined in millimetres as a tiny lateral shift may often translate into a large percentage difference that would overstate the clinical impact of the error. Electron beam central axis PDD curves are high gradient regions. For example, 4 MeV electron beams are characterized by gradients of magnitudes upwards of 70 %/cm. A deviation of 1 mm, such as those seen with day-to-day output fluctuations, would already exceed the Van Dyk 2 % limit. Therefore, a tolerance of ± 1 mm was set for central axis PDD curves. Van Dyk suggested a tolerance of 5 % along the central axis in the presence of heterogeneities. This criterion was also changed to an allowable deviation of ± 1 mm.

### 4.7 Evaluation Methods

A MatLab program was created to ensure a complete yet rapid data analysis process. This program reads measured data files acquired by the Wellhöfer Dosimetrie System as well as the CadPlan files containing the predicted dose distributions. The program then transforms these data sets such that their calculation matrices are identical, making for easy comparison. Subsequently, the error is computed and mapped in a colour-coded fashion; lines indicate errors expressed as a percentage and filled-in regions designate regions where error is expressed in millimetres. Both the measured and the calculated dose distribution for a given set of conditions were normalized to the depth of dose maximum of the measured distribution. The central axis PDD curve of the measured and of the calculated distribution were extracted and compared. The error map compares the measured and calculated distributions in all

areas other than the central axis, along which measured and calculated dose values are forced to conform. Van Dyk[1] suggested that evaluation of an electron beam treatment planning system requires comparison of a few measured and calculated profiles at designated depths. The error map goes beyond this criterion, allowing the error in all regions of interest to be known very rapidly. The MatLab program was not employed for the evaluation of cases involving heterogeneities since measured data was not collected using the Wellhöfer system. Instead, predicted and measured PDD curves were plotted in a Microsoft Excel spreadsheet and a manual comparison was executed.

## 4.8 References


1. Van Dyk, J. et al., *Commissioning and quality assurance of treatment planning computers*, Int J Radiation Oncology Biol Phys 26, p. 261-273, 1993.

2. Wellhöfer Dosimetrie, *IC10 chambers*, serial numbers : 2073, 2217.

3. Dosetek, *NACP chamber*, serial number : 1479.

4. Scanditronix, *GR-p BS p-type diodes for electron beams and corresponding reference diodes*, serial numbers : F1934, F1940.

5. Almond, P.R.et al., *AAPM's TG-51 protocol for clinical reference dosimetry of high-energy photon and electron beams*, Med Phys 26(9), p.1847-1870, 1999.

6. PTW-Freiburg, *Markus chamber*, serial number : N23343-1569.

7. Wellhöfer Dosimetrie, *WP700, CU 500 E electrometer.*

8. RMI, *Solid Water™*, water, lung, bone substitutes.

9. Keithley, *35040 Therapy Dosimeter*, serial number : 68396.

10. Burns, D.T., Ding, G.X., Rogers, D.W.O., $R_{50}$ *as a beam quality specifier for selecting stopping-power ratios and reference depths for electron dosimetry*, Med Phys 23(3), p. 383-388, 1996.

11. International Commission on Radiation Units and Measurement (ICRU), Report No 35, *Radiation Dosimetry: Electron Beams with Energies Between 1 and 50 MeV*, 1984.

12. Khan, Faiz M. et al., *Clinical electron beam dosimetry: Report of the AAPM Radiation Therapy Committee Task Group No. 25*, Med Phys 18(1), p. 73-109, 1991.

13. Ding, G.X., Rogers, D.W.O., Mackie, T.R., *Mean energy, energy-range relationships and depth-scaling factors for clinical electron beams*, Med Phys 23(3), p. 361-376, 1996.

14. Khan, Faiz M, *The Physics of Radiation Therapy*, Williams & Wilkins, Baltimore, 1994.

# Chapter 5

## Choice of Detector

Before performing the numerous measurements required to evaluate CadPlan's electron beam planning capabilities, a suitable detector had to be selected. A comparative study was executed to determine whether a thimble chamber, a parallel-plate chamber or a diode detector would prove most able to satisfy the demands of this work. Ideally, a detector should be of dimensions small enough to fulfill the conditions for a Bragg-Gray cavity, thereby minimizing fluence perturbation effects and promoting good resolution in both forward and lateral directions. Of course, the size of the detector must also be large enough to provide a reasonable signal. In addition to examining the dimensions of each detector, PDD curves and profiles were measured and compared. This chapter will first describe each of the detectors tested, followed by the presentation of the measured data. The results indicated that the IC10 chamber was the detector of choice.

### 5.1 Detector Types

Three detectors of different type were studied in order to establish which was most appropriate to carry out the many measurements demanded by this work. Two air ionization chambers, an IC10 thimble chamber and an NACP parallel-plate chamber, as well as a GR-p BS p-type silicon diode, were examined. This section of the chapter is dedicated to describing the salient characteristics of each of these detectors.

#### 5.1.1 IC10 Thimble Chamber

Air ionization chambers are the most prevalent detection method employed in radiation dosimetry. Ions are mostly generated in the surrounding medium and the chamber wall when exposed to directly and indirectly ionizing radiation. An applied polarizing voltage creates an electric field, which allows collection of ions as they traverse the air-filled chamber. A thimble or cylindrical chamber is so named for the shape of its wall, which encloses the air-filled cavity. Thimble chambers have a

central electrode which lies along the chamber's long axis and an outer electrode which makes up part of the chamber wall. Although thimble chambers are employed for electron beam measurements, they were originally designed for use with photon beams. Photon dosimetry demands that the chamber wall provide charged particle equilibrium (CPE). Precisely, the wall should be of a thickness that corresponds to the maximum range of a secondary electron produced in the chamber wall. Hence, the wall of a thimble chamber is typically constructed of a relatively thick layer of air equivalent plastic.

Conversely, a thin wall is stipulated for electron dosimetry. In this case, ionization in the air volume of the chamber arises due to charged particles stemming from the surrounding medium. In order to determine absorbed dose, Bragg-Gray cavity theory must be applied but this approach specifies that the cavity's presence must not affect the electron fluence. If the chamber wall is of a thickness comparable to the range of incident electrons, the interpretation of interactions within the air volume becomes challenging[1]. However, over the scope of energies typically employed in radiation therapy, the electron range dwarfs the wall thickness. This condition corroborates the suitability of the thimble chamber as a measurement device in electron beams.

The air volume itself is also a source of fluence perturbation. The cylindrical shape of the thimble chamber entails a relatively large thickness of air along the direction of irradiation. This condition favours the in-scatter effect so that electrons are more likely to be scattered into the lower density medium (air), within the chamber, than out of the chamber and into the higher density medium (water)[2]. The in-scatter effect leads to an overestimation of dose. However, electrons will adhere to straighter paths within a medium of lower density than of higher density. This phenomenon is known as the obliquity effect and is also consequential to a thicker air volume. This latter effect counteracts the in-scatter effect to some degree, but the in-scatter effect is dominant. Figure 5-1A illustrates the in-scattering effect while Figure 5-1B depicts the obliquity effect.

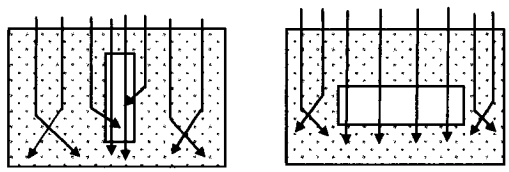


**Figure 5-1:** The in-scatter effect is depicted in A and the obliquity effect is shown in B.

The specific model of thimble chamber tested in this work was the IC10. The chamber wall and central electrode of this detector are constructed of the air equivalent plastic Shonka C 552. The wall thickness of the IC10 is 0.4 mm. This chamber's active region is characterized by a cross-sectional diameter of 6 mm, a length of 6.3 mm and a volume of 0.147 $cm^3$.

### 5.1.2 NACP Parallel Plate Chamber

The functional basis of parallel plate chambers is also air ionization. As stated previously, a good detector should minimize disruption of particle fluence. Plane parallel chambers accomplish this with active regions that feature a thin air gap. This gap separates the parallel electrodes characteristic of this chamber type. In this work, the NACP chamber was investigated. This chamber was designed for electron dosimetry involving beams in the energy range 2 to 50 MeV. The NACP boasts a thin coin-shaped air cavity, with spacing between electrodes measuring only 2 mm. This parallel-plate chamber features guard electrodes which prevent the measurement from including current leaks down the sides of the capacitor. In addition, the guard ring allows the active region of this chamber to be more sharply defined[2]. Mattson et al. reported that a parallel-plate chamber with an air cavity 2 mm deep should be equipped with a guard ring no less than 3 mm wide[1]. The design of the NACP chamber satisfies this requirement since its guard ring is 3 mm wide. This feature of the chamber ensures that any fluence perturbation does not reach the active volume[2]. The fluence perturbation correction for this detector may be taken as unity. The NACP chamber is characterized by an active diameter of 10 mm and an active volume of 0.16 $cm^3$. The dimensions of the chamber's Rexolite exterior are a height of 10 mm and a diameter of 30 mm. This detector's front window is 0.5 mm thick graphite covered by a 0.1 mm thick mylar film for waterproofing purposes. This relatively thin

window thickness ensures a stable active volume and facilitates measurements at shallow depths[1].

The limitations of the NACP chamber come into play when measuring profiles in a direction orthogonal to the beam direction. The degree of exactness to which a profile is measured is heavily dependent upon the detector's intrinsic spatial resolution[1]. The recorded data will actually be a convolution of the true profile and a function created by the presence of a detector of finite dimensions. D'Sousa demonstrated that the misrepresentation of true profiles rises with detector dimensions[1]. As the slope of the penumbra region becomes less abrupt deeper within a medium, this distortion effect becomes less pronounced. The active diameter of the NACP chamber is quite large at 10 mm and thus is detrimental to spatial resolution for profile measurement.

### 5.1.3 GR-p BS Diode

Introducing a minute amount of another material into silicon allows for the creation of a semiconductor. In the case of n-type silicon, an excess of electrons is produced while in the case of p-type silicon the resultant effect is a surplus of positively charged 'holes. Such holes may be thought of as an electron deficit. A p-type diode is created by adding a small quantity of n-type silicon to p-type silicon. A charge-free region, the depletion region, is formed. Upon irradiation of the diode, electron-hole pairs are produced and a small current is generated across the p-n junction. This signal is induced by charge carriers in the depletion region as well as minority carriers (electrons in the case of a p-type diode) that have managed to diffuse all the way to the depletion region[3]. Diodes only permit current to travel in a single direction. The impurity level is greater on the n side of the p-n junction to minimize the diffusion distance for holes and thus prevent them from contributing to the signal. Diodes may be operated with or without a bias voltage. In this work, the p-type diode employed was operated without a bias voltage. Such a technique minimizes leakage currents and allows for the detection of lower radiation intensities[2].

Semiconductor diodes are distinguished by a solid detection medium. The use of a higher density material allows for minimization of detector dimensions.

Additionally, approximately ten times less energy is needed to produce an electron-hole pair in silicon than an ion pair in air. This feature provides semiconductor detectors with great sensitivity. Ultimately, diode detectors may be constructed with small dimensions, allowing for good spatial resolution, yet still providing a good signal-to-noise ratio. Furthermore, restricted collisional silicon-water stopping power ratios approximate a constant function in the range typically employed in radiotherapy, 5-20 MeV. This trait eliminates the need for conversion and allows the depth ionization curve to be taken as the PDD curve.

The chief shortcoming of diode detectors is their susceptibility to radiation damage following exposure to especially large doses. Additional flaws are formed in the crystal lattice subsequent to much irradiation. Such imperfections behave like supplementary traps for minority carriers, skewing the radiation response. Rikner and Grusell demonstrated that a silicon diode detector may generate an invalid PDD curve after a great deal of use in a pulsed radiation beam[4]. However, p-type silicon is known to be much more resistant to radiation damage than n-type silicon. P-type diodes preserve linearity of response even after large dose accumulation. N-type diodes, on the other hand, are known to demonstrate non-linear behaviour. In order to minimize sensitivity loss due to radiation damage, diodes are pre-irradiated with large doses. Nonetheless, sensitivity fluctuations of about 0.3 % per kGy must be considered[3]. Also, diodes engineered to have higher impurity levels lose less sensitivity.

Other drawbacks are also associated with diode detectors. Diodes are subject to ambient temperature sensitivity. The change of sensitivity with temperature is linked to the amount of pre-irradiation administered to the diode[3]. Temperature effects are drastically diminished if the detector is operating in a large water phantom, which behaves like a thermal shield[2]. Directional dependence is a concern for n-type detectors. However, directional dependence of p-type diodes has been reported to be as low as 4 %[5]. A lack of reproducibility when employing diodes in electron beams was described by Thomas and Shaw[6]. It was determined that the orientation of the diode in its holder was the cause.

The particular p-type diode detector utilized in this study was the GR-p BS detector, produced by Scanditronix. It is characterized by a sensitive volume of

0.25 $mm^3$. The thickness of its active region is 0.06 mm and its active diameter is 2.5 mm. Such small active dimensions offer superior spatial resolution. The GR-p BS diode was pre-irradiated with 5 kGy of 20 MeV electrons, ensuring that further irradiation will not greatly affect the diode's sensitivity. The subsequent sensitivity variation with temperature for this amount of pre-irradiation is 0.3-0.4 % per °C. The level of boron doping of the GR-p BS diode is sufficiently high at $10^{15}$ atoms per $cm^3$ to elude superfluous sensitivity loss.

### 5.2 Measurements and Results

Before verifying the performance of each detector, the diode detector appeared to be the prime candidate due to the small dimensions of its active region. In order to determine which detector was truly superior, percent depth dose (PDD) curves and transverse profiles were measured and compared for all three detector types.

#### 5.2.1 Percent Depth Dose Curves

A study carried out by Rikner[5] revealed accordance to within 1.5 % or 1 mm between PDD curves measured with an NACP chamber and a p-type diode detector. Similarly, Ding and Chu[7] also demonstrated excellent agreement between PDD curves acquired with these detector types. The investigators also found that PDD curves measured with an IC10 chamber were in good accordance with those measured by the NACP chamber, albeit 1-2 % deviations were observed in the build-up region. By acknowledging the effects of depth and beam energy on fluence correction factors for the thimble chamber, such variations were diminished. Hence, it was anticipated that comparable curves would be produced by the three detectors to be tested in the study at hand.

In order to corroborate the output similarity of the three detectors, PDD curves were measured in water using a 3D scanning dosimetry system, as described in the preceding chapter. Energies of 4, 8, 12 and 20 MeV were employed. All measurements were executed with a source to surface distance (SSD) of 100 cm. Various field sizes were created using a 10x10 $cm^2$ applicator and circular cerrobend cut-outs of diameters 2, 3, 4 and 10 cm. These field sizes were selected because depth

of dose maximum, $d_{max}$, becomes progressively deeper with increasing field size until a certain diameter is reached, after which $d_{max}$ is essentially constant. The field of diameter 10 cm was chosen as it lies well within the plateau region of $d_{max}$ versus field diameter curve for all the energies tested. Figure 5-2 depicts $d_{max}$, measured with an IC10 chamber, as a function of field diameter for energies of 4, 8 and 12 MeV.

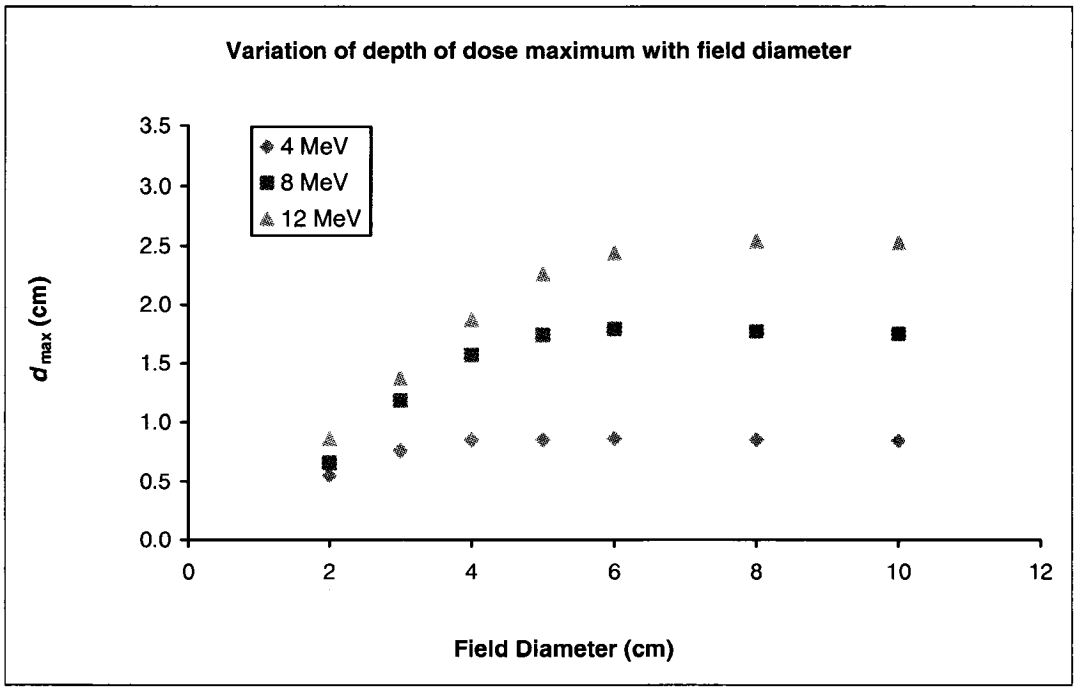


**Figure 5-2:** Depth of dose maximum, $d_{max}$, as a function of field diameter for various energies. Cerrobend masks with circular cut-outs of varying diameter were used in a 10x10 $cm^2$ applicator.

PDD curves acquired under a given set of conditions with each of the three detectors were compared. Some results appeared to confirm output similarity between the three detectors. Figure 5-3 presents such an example.

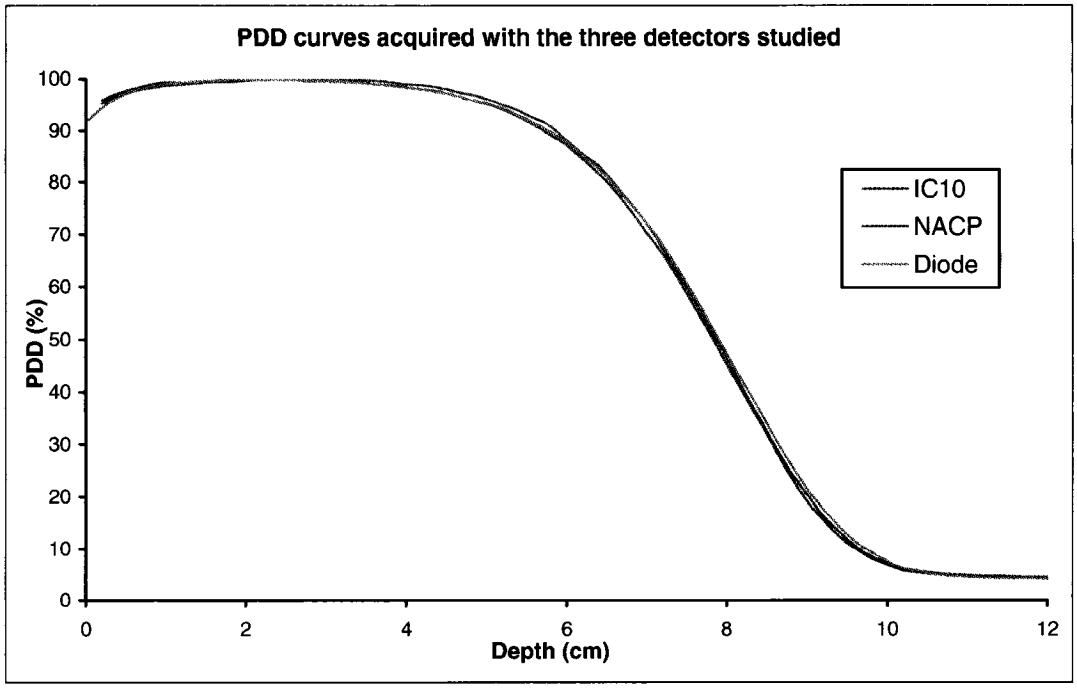


**Figure 5-3:** Comparison of PDD curves measured with the three detectors studied. The measurement conditions for these PDD curves were a 20 MeV beam and a circular field of diameter 10 cm. A 10x10 $cm^2$ applicator was employed.

Disappointingly, similar results were not seen for all of the other cases tested. While the IC10 and NACP chambers generally produced concurring results, the diode behaved in an erratic manner. During some measuring sessions, the diode produced PDD curves that matched those obtained with the other detectors. Other sessions, however, resulted in diode PDD curves plagued by gross deviations.

No deviation greater than 1 mm occurred between the dose fall-off regions of PDD curves measured with the IC10 and NACP chambers for all field size and energy combinations tested. An average discrepancy of 2 mm was apparent between diode PDD curves and curves acquired with the IC10 and NACP chambers. A trend of larger disparity with higher beam energy was noted. More prominent, however, is the fact that the largest deviations all arose in the instance of a field of diameter 2 cm. All diode PDD curves that did not match the curves acquired with the other detectors were located distinctly to the right of the PDD curves measured with the IC10 and NACP chambers. This fact suggests some systematic component to the error observed.

Figure 5-4 displays an example where the diode produced a PDD curve that differed greatly (up to 2 mm) from the curves acquired with the air ionization chambers.

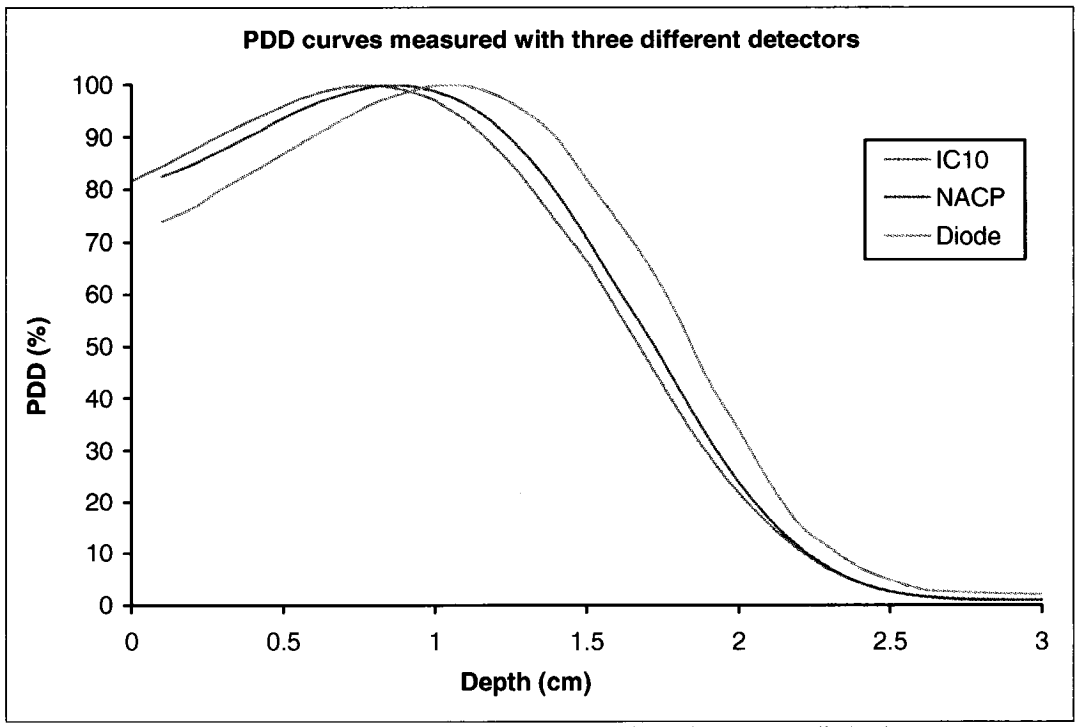


**Figure 5-4:** Comparison of PDD curves measured with the three detectors studied. The measurement condition was a 4 MeV beam and a circular field of diameter 10 cm created by a cerrobend cut-out inserted into a 10x10 $cm^2$ applicator.

A total of five measuring sessions were dedicated to investigating the inconsistent behaviour of the diode. During the initial session, the diode produced curves that conformed excellently, as presented in Figure 5-3. Erroneous curves were generated during the second, third and fifth sessions. During the fourth session, diode PDD curves exhibited adequate agreement with those acquired with the other detectors. The cause of such variation could not be a fluctuation of beam energy as curves obtained with the IC10 and NACP chambers curves neatly coincided with one another during all of the measuring sessions.

It is interesting to note the day-to-day variation in bremsstrahlung dose, $D_X$, predicted by the diode, since diode detectors are known to provide a more realistic $D_X$ than ionization chambers. $D_X$ values obtained from IC10 and NACP PDD curves

demonstrated accordance to within 0.2%. Diode $D_x$ values were originally expected to be slightly higher than those acquired with air ionization chambers. However, diode $D_x$ values tended to either exceed IC10 and NACP $D_x$ values by up to 3 % or produce $D_x$ values about 0.5 % below what was obtained with the other detectors.

Noteworthy discrepancies in the build-up, fall-off and tail regions of diode PDD curves acquired on different days are typical results of this investigation. Figure 5-5 depicts diode PDD curves measured with the same energy and field size combinations during two different measuring sessions. The diode PDD curves obtained during Session 2 deviate significantly from IC10 and NACP PDD curves measured under the same conditions. On the contrary, the diode PDD curves acquired during Session 4 conform adequately to those obtained via the other detectors. Discrepancies of up to 3 mm at $d_{50}$ were observed between PDD curves measured with the same diode during two different measuring sessions.

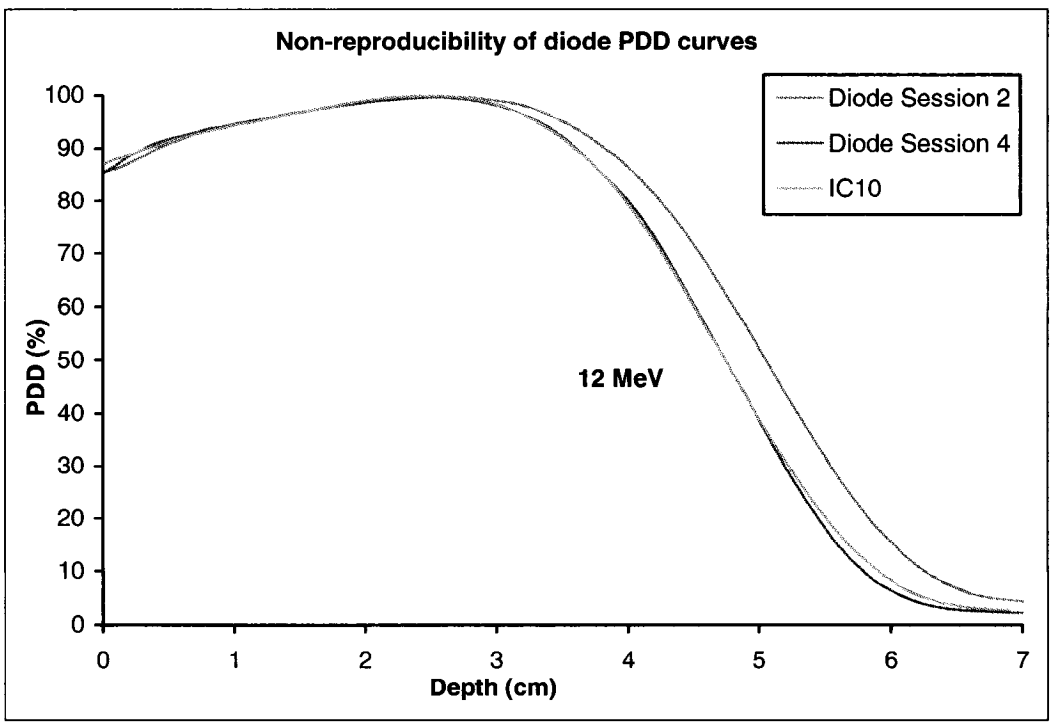


**Figure 5-5:** Diode PDD curves obtained during two separate measuring sessions under the same conditions in comparison with a curve acquired with an IC10 detector. The conditions represented here include a 12 MeV beam and a circular field of diameter 10 cm created with a cerrobend cut-out inserted in a 10x10 $cm^2$ applicator.

Throughout the measuring sessions, the diode had been oriented consistently in the position recommended by the manufacturer; straight up with its circular face flush

with the water surface. As some experimenters[6] had reported reproducibility problems stemming from bad orientation, a second position was tested. The diode was placed orthogonal to its original position. This repositioning failed to improve the PDD curves obtained with the diode.

The same diode had been used in all of the measuring sessions so it needed to be verified that the diode itself was not the problem. This possibility seemed doubtful however, as the diode had rarely been used and was thus unlikely to be warped by radiation damage. Another diode of the same model was tested. In a measuring session during which the first diode had failed to produce PDD curves akin to those of the other detectors, a second diode was employed. PDD curves generated by the second diode consistently corresponded to those produced by the first diode for a variety of field sizes and energies. Consider, for example, the case of an 8 MeV beam and a field of diameter 10 cm. The IC10 and NACP chambers produced similar results while the PDD curves generated by the first and second diodes tested matched one another but strayed from the curves acquired with the other detectors. Figure 5-6 displays these results.

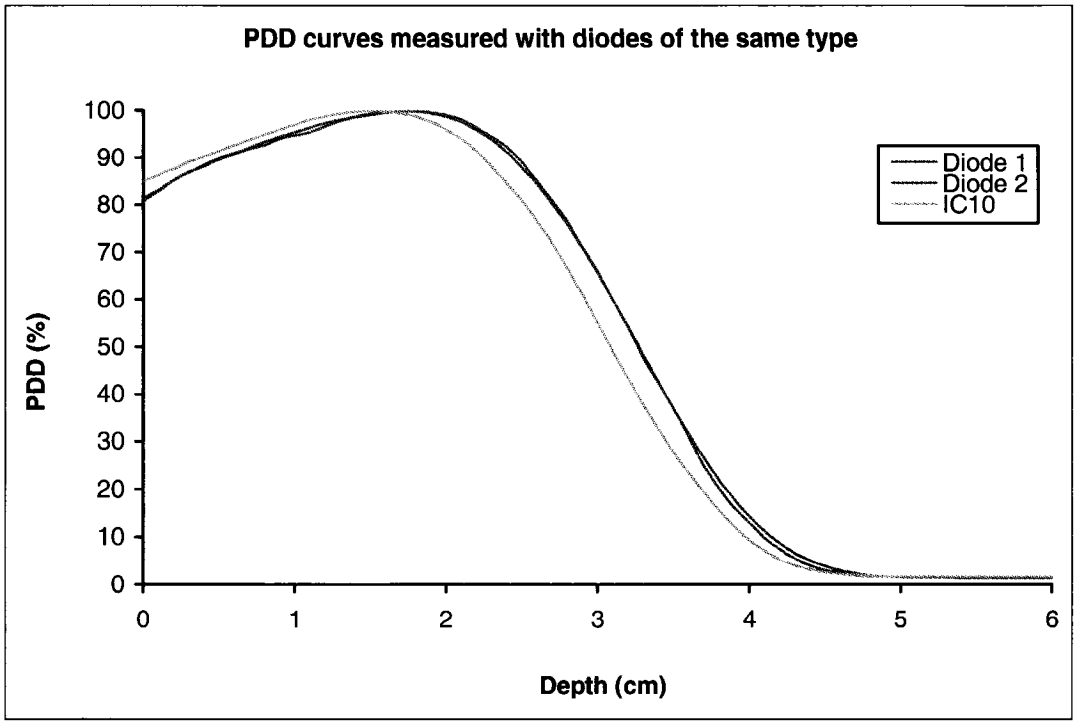


**Figure 5-6:** PDD curves measured with two different diodes of the same type during the same measuring session as well as an IC10 PDD curve. Measurement conditions were an 8 MeV beam and a circular field of diameter 10 cm produced with a cerrobend cut-out in a 10x10 $cm^2$ applicator.

It thus appears that the most probable cause of the observed diode instability was the electrometer. A set-up error on the part of the experimenter is unlikely since the set-up was verified by colleagues on more than one occasion. Both the IC10 and NACP chambers require a polarizing voltage; 400 V was utilized. No polarizing voltage should be applied to the diode, however. Prior to the commencement of diode measurements it was consistently verified that the electrometer was set to zero volts. Nevertheless, each time the diode was employed it took relatively long for the electrometer to stabilize, an indication that the electrometer might have been the source of the problem.

### 5.2.2 Transverse Profiles

Profiles were measured at $d_{max}$, $d_{85}$ and $d_{50}$ of the PDD curve for a given field size and energy combination. Profile analysis included comparison of the full profile width at various depths. All profiles were normalized to 100 %. Their widths were then evaluated at 90 %, 80 %, 50 % and 30 % of the normalization value. The IC10 chamber was selected as the reference as it was expected to achieve better spatial

resolution than the NACP chamber. Table 5-1 presents differences in full widths of profiles acquired with different detectors at $d_{max}$ and $d_{50}$ for 4 and 8 MeV beams and a circular field of diameter 2 cm. These results are typical as similar results were obtained for 12 and 20 MeV beams.

| **Discrepancies (mm) in profile full width for the three detector types** | | | | | | | | |
|---|---|---|---|---|---|---|---|---|
| | 4 MeV | | | | 8 MeV | | | |
| | Profile at $d_{max}$ | | Profile at $d_{50}$ | | Profile at $d_{max}$ | | Profile at $d_{50}$ | |
| | *NACP-IC10* | *Diode-IC10* | *NACP-IC10* | *Diode-IC10* | *NACP-IC10* | *Diode-IC10* | *NACP-IC10* | *Diode-IC10* |
| 90 % | 0 | 0.1 | 0.6 | 0 | -0.2 | 1.0 | 0.5 | 0.2 |
| 80 % | 0 | -0.1 | 1.0 | 0.1 | -0.1 | 1.1 | 0.9 | 0.1 |
| 50 % | 0.2 | -0.8 | 1.4 | 0.1 | 0.9 | 1.1 | 1.8 | 0.1 |
| 30 % | 0.4 | -1.6 | 1.9 | 0.4 | 1.9 | 1.4 | 2.8 | 0.4 |

**Table 5-1:** Differences (mm) between full profile widths for the three detectors studied. Measurement conditions in this example included beams of energies 4 and 8 MeV and a circular field of 2 cm diameter created with a cerrobend cut-out inserted into a 10x10 $cm^2$ applicator.

The diode detector most often overvalued the width of profiles obtained at $d_{max}$, as reported by the 8 MeV column in Table 5-1. However, on seemingly random occasions, the diode underestimated profile width, as related in the 4 MeV column of the table. In this manner, diode instability manifested itself in the transverse profiles. In spite of this, discrepancies between the diode and the air ionization chambers were not nearly as dramatic as those observed for PDD curves. Deviations between the detectors were consistently inferior to 3 mm, with the largest disparities appearing in the lower dose regions of a given profile. These regions are wide enough that even a difference of 3 mm on the full width is not terribly large. The NACP chamber usually produced profile widths that were larger than those derived from data obtained with the IC10 chamber. These differences were typically more pronounced for profiles acquired at greater depths, as may be noted in Table 5-1. For a given profile, the discrepancies also tended to be larger for widths evaluated at 50 % or 30 % of the normalization value.

### 5.3 Rationale for Detector Selection

The IC10 chamber was the detector selected to perform the numerous measurements required to evaluate CadPlan. Although the diode's physical characteristics were superior to those of the ionization chambers, it obviously had to

be eliminated as a choice due to the extreme instability it revealed during comparison testing. The IC10 and NACP chambers generated PDD curves and crossplane profiles that demonstrated a high degree of accordance and reproducibility. These results indicated that either ionization chamber would have been a fit choice.

Many of the measurements to come demanded scanning in an orientation perpendicular to the depth direction. This requirement stressed the importance of spatial resolution. As the penumbra region is characterized by an abrupt dose decline or rise, this portion of a profile is especially susceptible to significant misrepresentation triggered by a large active diameter. The margins that deem a treatment planning system acceptable are fairly stringent. It was thus important to circumvent error caused by a lack of spatial resolution, which would manifest itself in all isodoses. Hence, the NACP chamber was rejected.

The walls of the IC10 chamber are actually slightly thinner than the entrance window of the NACP chamber. Nonetheless, they are thick enough to undermine the viability of this detector in the build-up region, where a thin entrance window is valuable for obtaining accurate measurements. Beyond $d_{max}$, however, this criterion loses its importance[2]. Therefore, problems associated with the use of an IC10 chamber for electron beam measurements are essentially confined to the build-up region. In order to investigate the extent of errors induced by the use of this chamber type, build-up curves were measured in Solid Water™ with a PTW Markus parallel-plate chamber (as referred to in Chapter 4) for beam energies of 4, 12 and 20 MeV and field sizes of 6x6, 10x10 and 20x20 $cm^2$. The PTW Markus chamber is characterized by an extremely thin entrance window and a small active volume[1], permitting very accurate measurement in the build-up region. Figure 5-7 presents typical results of comparisons between build-up curves measured with an IC10 chamber in water and a PTW Markus chamber in solid water.

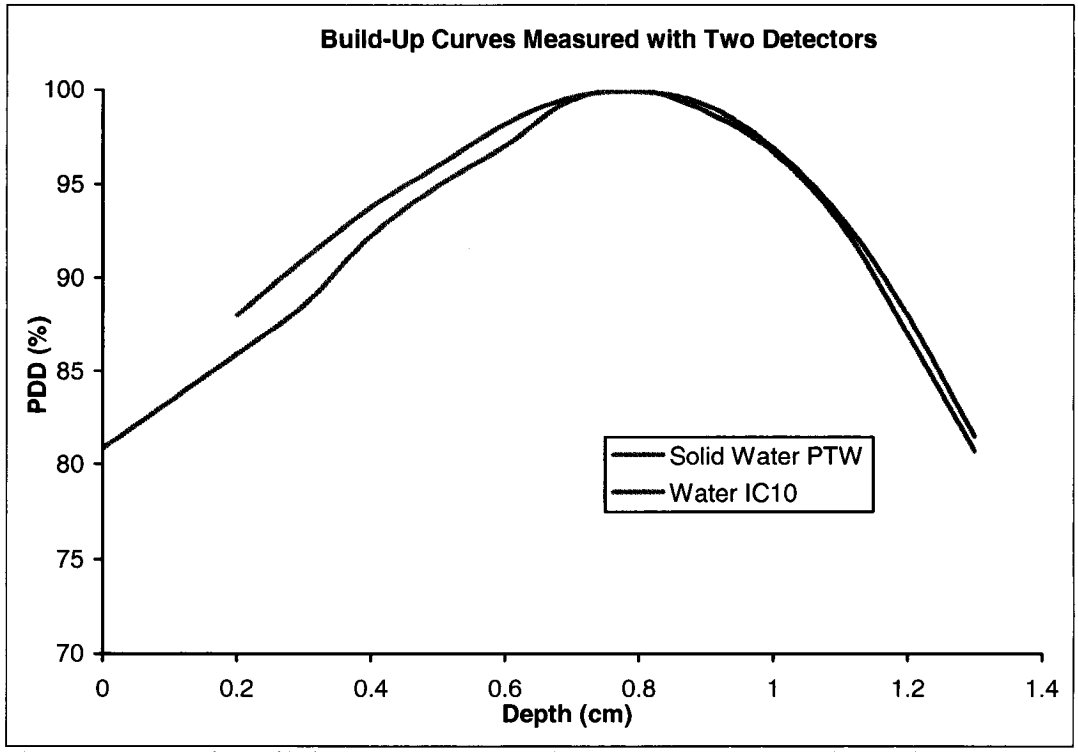


**Figure 5-7:** Comparison of build-up curves measured in water with an IC10 chamber and in solid water with a PTW Markus chamber. Measurement conditions included a beam energy of 4 MeV and a 20x20 $cm^2$ field created with a standard applicator. A positive polarity was applied to each detector.

Satisfactory agreement was obtained for all cases tested, with no disparity exceeding 2.5 %. Hence, the IC10 chamber was deemed suitable for measurements within the build-up region for the purposes of this work. Furthermore, CadPlan is known to be unsound within the first 5 mm below the surface[8, 9], making the accuracy of measurements within the build-up region less than critical. Beyond 0.5 cm, dose differences in the build-up regions of curves acquired with the IC10 and the PTW Markus chamber were typically diminished to about 1 %. The importance of accurate measurement is intensified, however, when considering the large field PDD curves that must be entered into CadPlan. These curves play a major role in determining the quality of the dose distribution predicted by CadPlan. To ensure accuracy, build-up regions measured in solid water with the PTW Markus chamber could be substituted for build-up regions measured with the IC10 chamber in water for the curves to be entered into CadPlan. Klevenhagen confirms the legitimacy of measuring different portions of PDD curves with different detectors in different media[2]. However, this procedure was determined to be unnecessary for the scope of this work. Ultimately, the utilization of the IC10 chamber for the measurements necessitated by this work is a justifiable choice.

## 5.4 References


1. Klevenhagen, S.C., *Physics and Dosimetry of Therapy Electron Beams*, Medical Physics Publishing, Madison, 1993.

2. Klevenhagen, S.C., *Physics of Electron Beam Therapy*, Adam Hilger, Ltd., Bristol, 1985.

3. Knoll, G.F., *Radiation Detection and Measurement*, John Wilely & Sons, New York, 1989.

4. Grusell, E., Rikner, G., *Radiation damage induced dose rate non-linearity in an n-type silicon detector*, Acta Radiol Oncol 23, p. 465-469, 1984.

5. Rikner, G., *Characteristics of a p-Si detector in high energy electron fields*, Acta Radiol Oncol 24, p.71-75, 1985.

6. Thomas, R.L., Shaw, J.E., *Radiation measurements with diode detectors*, Phys Med Biol 23(3), p. 519-521, 1978.

7. Ding, G.X., Yu, C.W., *Determination of percentage depth-dose curves for electron beams using different types of detectors*, Med Phys 28(3), p. 298-302, 2001.

8. Varian, *CadPlan manual: External beam modelling physics v 6.0*, 1999.

9. Ding, G.X. et al., *Evaluation of a commercial three-dimensional electron beam treatment planning system*, Med Phys 26(12), p. 2571-80, 1999.

# Chapter 6

## Results and Discussion

A comprehensive set of measurements was performed with the object of assessing CadPlan's capacity to calculate electron beam distributions. Before implementing CadPlan electron beam treatment planning clinically, it is imperative that the error margins be tabulated for a gamut of field characteristics. Several user-entered parameters must be entered into CadPlan in order to ensure that some specificity of the user's accelerator is taken into account. The chapter commences by presenting the values for these parameters that were used in this work. In addition, the effect of each input parameter on the predicted dose distributions is also discussed. Overall, CadPlan performed in a fair manner as an electron beam treatment planning system, although errors did not always lie within the set tolerances when non-standard conditions were imposed. This chapter details the degree of accuracy achieved by CadPlan-predicted dose distributions when considering fields of various size, energy, gantry angle and source to surface distance for homogeneous phantoms. Furthermore, CadPlan-generated depth dose curves were compared to curves measured in heterogeneous phantoms for an assortment of field size and energy combinations, all employing a zero degree gantry angle and the standard treatment distance. Although CadPlan was somewhat more capable of determining cut-out factors, the system failed completely at predicting output factors that related fields created by different applicators. As a final test, the CadPlan distribution created for a real patient was evaluated. The chapter concludes with a discussion of the shortcomings of CadPlan as an electron beam treatment planning system. Possible improvements are suggested.

### 6.1 CadPlan Input Parameters

For each virtual machine created in CadPlan, the user must enter values for several parameters. These include the mean square scattering angle, the mean energy at the surface, the virtual source to reference plane distance and a normalization factor. Large field open and blocked depth dose curves must also be entered. The quality of CadPlan-generated distributions hinges on the values of these parameters, which must be optimized by the user.

In order to make CadPlan electron beam treatment planning clinically viable, only one virtual machine should be created per energy. The ideal situation would allow for a virtual machine to exist for individual applicator and energy combinations. In that case, the values of the input parameters entered could be specific enough for a given combination to guarantee increased accuracy. However, that approach would entail the creation of about 100 virtual machines, an undertaking of monumental impracticality. Therefore, the challenge that presents itself to the user is determining the globally satisfactory set of values, for a given energy, that provides accurate distributions for all applicators. This section presents the input parameter values employed in this study.

### 6.1.1 Mean Square Scattering Angle at the Reference Plane

The angular variance, or mean square scattering angle at the base of the applicator, $\overline{\theta^2}(0)$, is a parameter of chief importance. In the CadPlan algorithm, it functions as the principal regulator of the width of a given dose distribution, as it is intimately linked to spatial variance (Eq. (3-7)). A more rigorous description of angular and spatial variances was presented in Chapter 2. By the time the electron beam attains the reference plane, it has already navigated many obstacles. These include the components of the linac head, such as the monitor chamber, scattering foils and jaws, and the applicator itself. In their 1987 work, Huizenga and Storchi demonstrated that the angular variance will be augmented if the beam traverses scattering layers[1]. As it happens, the scattering agents situated closer to virtual source, for instance the primary scattering foil, contribute minimally to the boost in the angular spread[2]. Therefore, the secondary scattering foil, the jaws and the applicator contribute most to the increase. As mentioned in Chapter 1, the Elekta SL 25 employs several secondary scattering foils of varying thicknesses on a carousel. The selection of the secondary scattering foil to be placed in the beam is dependent only on the electron energy requested by the user. As each electron energy necessitates its own virtual machine in CadPlan, only changes in angular spread incited by different jaw positions and different applicators become important for this work.

The design of the applicator heavily influences the distribution of scattered radiation at the reference plane, thus influencing the value of the mean square scattering angle required as input for CadPlan. The material of which the applicator is fabricated, the number of tiers used for intercepting electrons, the distance to the isocentre and the position that the jaws assume when an applicator is fitted all participate in determining the angular spread. Jaw design also plays a role. Interestingly, the linac employed in this work, the Elekta SL 25 features an MLC located between the two sets of jaws, as mentioned in Chapter 1.

Van Battum and Huizenga[2] have proposed that the angular variance at the base of the applicator is linearly dependent on the scattering power in air, evaluated using the mean energy at the surface, $T_{air}(E)$. In other words, a constant value was suggested for the ratio $\overline{\theta^2}(0)/T_{air}(E)$, for a given make and model of linac. It should be noted that the authors of the original work used different notation. Theory indicates that angular variance is dependent on energy and not on field size. This energy dependence is embodied by the scattering power, thus the energy dependence may be removed by considering the aforesaid ratio. This ratio may be used to determine the initial mean square scattering angle that is required as input by pencil beam models. Such a procedure requires caution; theory's dismissal of field size or applicator size dependence does not mirror reality, as will be evidenced later in the chapter. Van Battum and Huizenga found that several modern accelerators may be characterized by the same angular variance to scattering power ratio. However, in their paper, the Elekta SL 15 was set apart by a ratio 50 % larger than that of the other accelerators[2]. This result translates into larger mean square scattering angles at the reference plane for that machine. Furthermore, the investigators demonstrated that the jaws and the applicator are responsible for this difference. The angular variance of the primary radiation was investigated by performing measurements incorporating extended SSDs. At such distances any scattered radiation would have been dispelled, leaving only the primary component. These measurements revealed that the Elekta machine is characterized by the same primary angular variance to scattering power ratio as the other linacs. The Elekta SL 15 is of the same series as the Elekta SL 25, employed in this work, thus these results are applicable. Interestingly, a recent van Battum article

reported that Elekta applicators actually produce less scatter than those of other companies[3]. The scatter that is produced, however, is characterized by a wider spread.

The values deemed optimal in the present work are displayed in Table 6-1, along with values suggested by the CadPlan manual[4] and those derived from the ratio suggested by van Battum and Huizenga, using scattering power tables from ICRU 35[5]. These ICRU tables were tabulated from Eq. (2-30). In the current work, trial and error was used to determine the optimal value for the initial mean square scattering angle for each virtual machine. For 20 and 22 MeV beams, a single value for this parameter was unable to generate satisfactory results for all applicator sizes. Hence, two virtual machines with different mean square scattering angles were created for these two energies.

| **Comparison of Mean Square Scattering Angle Values** | | | | |
|---|---|---|---|---|
| Energy (MeV) | Mean Square Scattering Angle ($rad^2$) | | | |
| | *CadPlan Manual* | *Van Battum* | *Hodefi* | |
| 4 | 0.0065 | 0.0287 | 0.0195 | |
| 6 | 0.0065 | 0.0156 | 0.0170 | |
| 8 | - | 0.0100 | 0.01235 | |
| 10 | 0.0025 | 0.0071 | 0.0105 | |
| 12 | - | 0.0044 | 0.0090 | |
| 15 | - | 0.0036 | 0.0076 | |
| 18 | - | 0.0025 | 0.0054 | |
| 20 | 0.0009 | 0.0022 | 0.00436 | 0.00146 |
| 22 | - | 0.0016 | 0.0032 | 0.0013 |

**Table 6-1:** Comparison of the mean square scattering angle values at the reference plane ($rad^2$). The latter column presents the values employed in the present work for the Elekta SL 25. The first column relates the start values suggested in CadPlan documentation[4]. The central column shows values for the Elekta SL 15 stemming from the work of van Battum and Huizenga[2].

Although CadPlan is manufactured by Varian, it has been shown that much higher values of the initial mean square scattering angle are appropriate for modern linacs of Varian make[2]. Significant differences also exist between the values obtained by trial and error in this work and those obtained by the angular variance to scattering power ratio, as measured by van Battum and Huizenga. In the case of the lowest energy studied, 4 MeV, the value provided by the ratio exceeds that chosen for the present study. The contrary is true for all other energies investigated. From 12 to 18

MeV, the values employed in this work are consistently twice those reported by van Battum and Huizenga.

There are several factors which may be responsible for the observed discrepancies. Firstly, as aforementioned, the jaws assume different positions depending upon which applicator and energy combination is selected. These positions are adjusted during the commissioning of the machine in order to achieve a flat dose profile at depth in water for an SSD of 100 cm. Hence, linacs of the same type may utilize different jaw positions. The scatter contribution to $\overline{\theta^2}(0)$ will be influenced by jaw configuration. However, modifying jaw positions will yield output changes of only a few percent, rendering it difficult to predict how jaw position truly impacts scattered radiation[3].

Furthermore, there exists a most noteworthy distinction between the mean square scattering angle values stemming from the work of van Battum and Huizenga and those chosen in this work. The latter set of values was found to provide the best set of dose distributions for a given energy, encompassing all applicators, even the smallest (6x6 $cm^2$), and those of an elongated rectangular shape. The former set of values was averaged over field size but only two field sizes were investigated[2]: 10x10 $cm^2$ and 20x20 $cm^2$. These field sizes may be considered as similar and are not characterized by any of the scattering eccentricities that may arise when dealing with small or non-square fields. Therefore, the angular variance to scattering power ratio may not be suitable for all Elekta SL 25 applicator sizes. Theory precludes angular variance from field size dependence. Nevertheless, the penumbra for electrons is influenced by scattering in the collimating system[5], namely, the jaws and applicator. Different field sizes necessitate that different jaw positions be assumed and that different applicators be fitted to the treatment head. The resultant changes in scatter will cause penumbra values to deviate although the nominal energy is held constant. Angular variance relates to penumbra as[2]:

$$\overline{\theta^2}(0) = 2\left(\frac{\chi^2}{2\pi g} - \frac{T_{air}(\overline{E_0})g}{6}\right), \qquad (6\text{-}1)$$

where $g$ is the gap distance between the base of the applicator and the patient surface (5 cm for the Elekta SL 25) and $\chi$ is the penumbra measurement of a profile acquired at the surface. It should be noted that Eq. (6-1) differs from that specified in the reference owing to differences in notation. $\chi$ is defined as the profile dose maximum value divided by the slope tangent to the point of half-maximum[1]. It has been demonstrated that a change in field size between a 10x10 $cm^2$ field and a 20x20 $cm^2$ triggers a change in penumbra of approximately 10 % in the case of the Siemens MD2 accelerator[2]. Clearly, greater variations in $\chi$ are to be expected for very big, very small or elongated fields. In addition, the Elekta SL 25 is known to generate scatter of larger angular variance than other modern linacs, which could produce larger changes in $\chi$. In this work, the penumbra, defined as $\chi$, was obtained from measured data for all energies studied and field sizes 6x6 $cm^2$ and 20x20 $cm^2$, with an SSD of 100 cm and zero gantry angle. In order to investigate the influence of applicator size or field size on the mean square scattering angle, this latter parameter was calculated for a large and a small applicator size using penumbrae obtained from profiles measured at the phantom surface. The relative difference in the mean square scattering angle was taken as the difference between the mean square scattering angle obtained for a large applicator and that for a small applicator divided by the value suggested as input for an electron beam treatment planning system. This relative percent difference may be denoted as $\frac{\Delta\overline{\theta^2}(0)}{\overline{\theta^2_{input}}(0)}$ and calculated using:

$$\frac{\Delta\overline{\theta^2}(0)}{\overline{\theta^2_{input}}(0)} = \frac{\overline{\theta^2_{20x20}}(0) - \overline{\theta^2_{6x6}}(0)}{\overline{\theta^2_{input}}(0)} = 2\left(\frac{1}{2\pi g^2}\frac{\chi^2_{20x20} - \chi^2_{6x6}}{\overline{\theta^2_{input}}(0)}\right), \tag{6-2}$$

where $\chi_{20x20}$ and $\chi_{6x6}$ describe the penumbrae of 20x20 $cm^2$ and 6x6 $cm^2$ standard applicator fields respectively and $\overline{\theta^2_{input}}(0)$ is the angular variance reported by van Battum and Huizenga. Table 6-2 reports the relative percent differences obtained.

| Percent Differences in Angular Variance Produced by Different Field Sizes | |
|---|---|
| Energy (MeV) | Percent Difference (%) |
| 4 | 11.0 |
| 6 | 1.2 |
| 8 | 2.0 |
| 10 | -40.7 |
| 15 | -66.3 |
| 18 | -73.6 |
| 20 | -231.6 |
| 22 | -459.8 |

**Table 6-2:** Percent differences in angular variance triggered by a change in standard applicator field sizes from 20x20 $cm^2$ to 6x6 $cm^2$.

The results presented in Table 6-2 clearly demonstrate that the design of the Elekta SL 25 does indeed cause the mean square scattering angle at the base of the applicator to depend on applicator size. Implicit in this dependence is a further dependence on jaw position since the jaws assume different positions when different combinations of beam energy and applicator are selected. The percent difference balloons at 20 and 22 MeV. These percent differences appear very large. However, they are consistent with the mean square scattering angles found by trial and error that served as CadPlan input for this work. For example, in the case of the 20 MeV and the 22 MeV beams two virtual machines had to be created in order to obtain acceptable distributions over the span of applicator sizes used in this work, as displayed in Table 6-1. In the case of the 20 MeV beam, the two mean square scattering angles used as input differ by a factor of 3. A factor of 2.5 may be noted between the input values for the 22 MeV beam. Although only one virtual machine per energy was necessary for each of the other beam energies studied, the results in Table 6-2 demonstrate that fairly large differences between the mean square scattering angles of different field sizes still exist. A relatively large difference between the actual mean square scattering angle for a given applicator and energy combination and that used by a treatment planning system does not automatically translate into an error of the same magnitude where dose is concerned. Nonetheless, more accurate input values do promote more realistic dose distributions. The results shown in Table 6-2 reveal the trend that as electron energy is augmented, the mean square scattering angle of a field created with a small applicator becomes increasingly larger than that created with a large applicator for the same energy.

The mean square scattering angle dictates the spread of the beam. A larger value prompts greater spreading while a smaller value implies that transverse profiles will be more abrupt. Figure 6-1 exhibits profile behaviour as predicted by CadPlan using different mean square scattering angles for a 6 MeV beam created with the standard Elekta 20x20 $cm^2$ applicator at a depth of 1 cm:

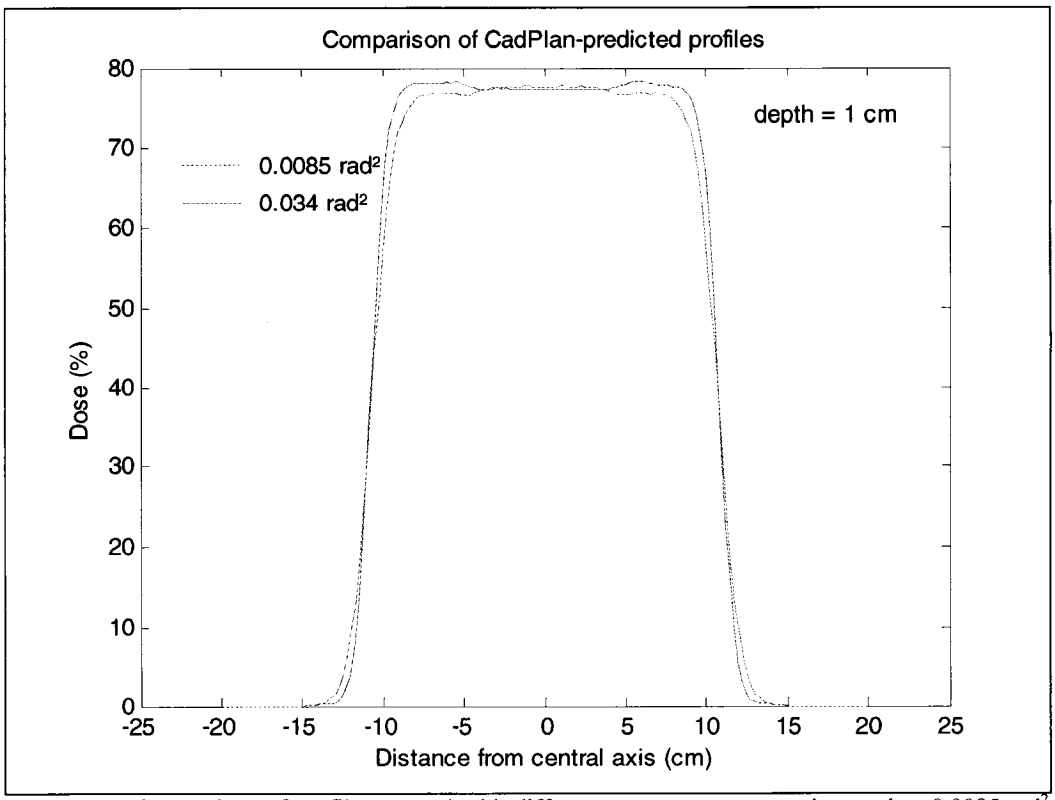


**Figure 6-1:** Comparison of profiles created with different mean square scattering angles: 0.0085 $rad^2$ and 0.034 $rad^2$. The profiles above correspond to 6 MeV beam and a 20x20 $cm^2$ field with an SSD of 100 cm and zero gantry angle at a depth of 1 cm.

The value of the mean square scattering angle at the reference plane must be chosen such that accurate profiles are predicted at nearly all depths for every field size desired for a given energy. For each field size and energy combination, a range of values will produce a distribution that satisfies the tolerances described in Chapter 4. Consider, for example, an energy of 6 MeV and a field size of 20x20 $cm^2$. The error distribution corresponding to the mean square scattering angle value entered into CadPlan (0.017 $rad^2$) is displayed in Figure 6-2. This figure is an error map, as defined in Chapter 4. It displays the errors as a 2D representation. Solid colour blocks correspond to high gradient regions where errors are in millimetres. Lines are

indicative of low gradient regions (< 30 %/cm) where errors are described as percentages. Clearly, the acceptance criteria (high gradient region errors < 2 mm and otherwise errors < 4 %) are generally satisfied. It should be noted that no error is depicted along the central axis of the error map. These diagrams display errors in all regions other than the central axis. A comparison of central axis PDD curves is used in this work to evaluate error in this region, as described in section 4.7. Figure 6-3 displays error distributions near the limits of the acceptable range. These distributions also, for the most part, satisfy the set tolerances. Thus, for the case of a 6 MeV beam and a 20x20 $cm^2$ field, any mean square scattering angle value between 0.012 and 0.021 $rad^2$ will generate a clinically acceptable dose distribution. A value of 0.011 $rad^2$ produces an unacceptable distribution riddled with errors exceeding 4 % in high dose regions. A mean square scattering angle of 0.022 $rad^2$ also makes the predicted distribution unacceptable, introducing errors exceeding 2 mm in the penumbra. Figure 6-4 displays these substandard error distributions. The change in the quality of a predicted distribution as the mean square scattering angle is varied may not be considered as truly gradual. Of course, as one moves away from the optimal value, the predicted distribution will deteriorate. However, very little change may be noted even over large jumps in the value of the mean square scattering angle. However, an additional small difference in the mean square scattering angle might result in a distribution that is significantly inferior.

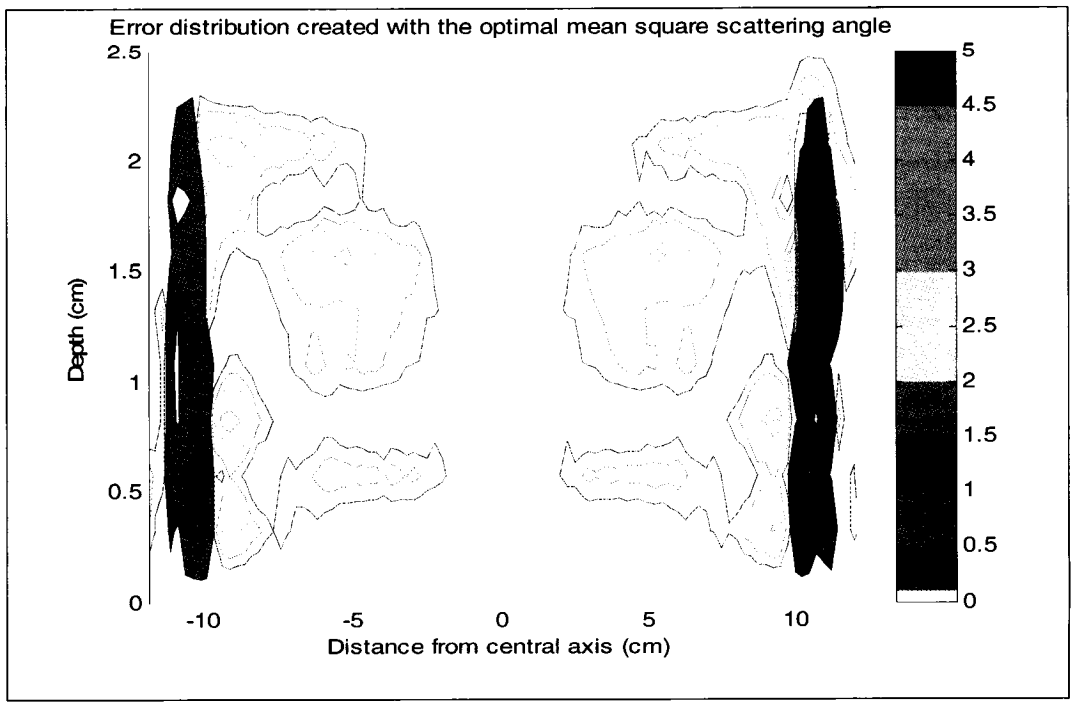


**Figure 6-2:** An error distribution generated with the optimal $\overline{\theta^2}(0)$ for the case of a 6 MeV beam. Other conditions include a field size of 20x20 cm$^2$, created with the standard applicator, an SSD of 100 cm and zero gantry angle.

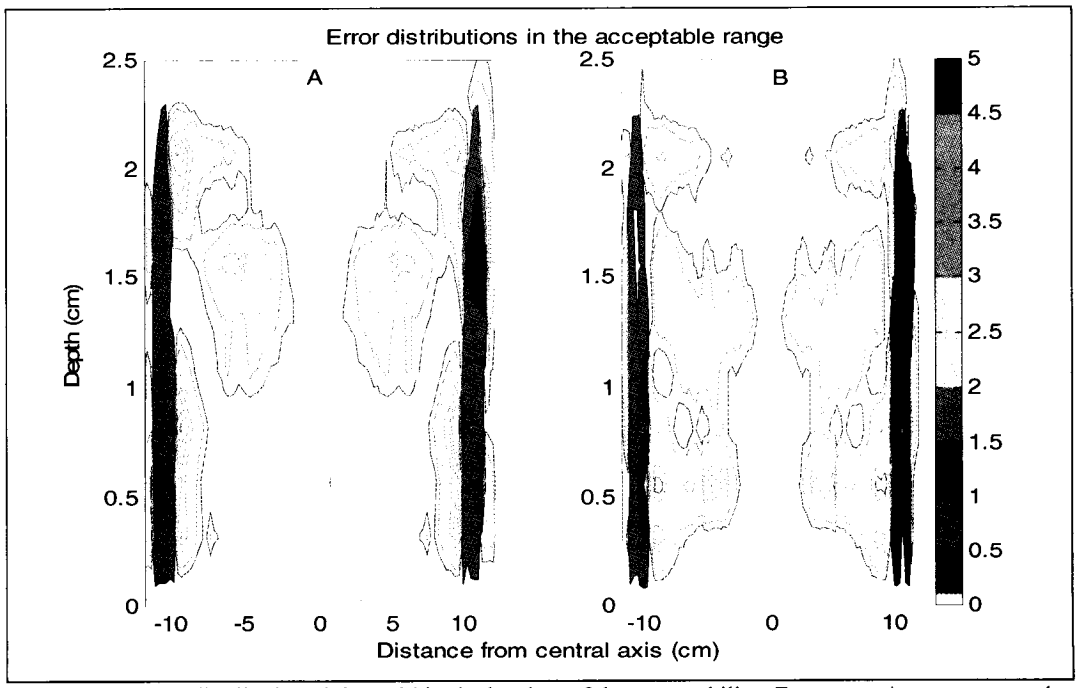


**Figure 6-3:** Error distributions lying within the borders of the acceptability. Error map A was generated using $\overline{\theta^2}(0)$ equal to 0.012 rad$^2$. This value of this parameter used in error map B was 0.021 rad$^2$. Conditions included a 6 MeV beam, a 20x20 cm$^2$ field, the standard SSD and orthogonal incidence.

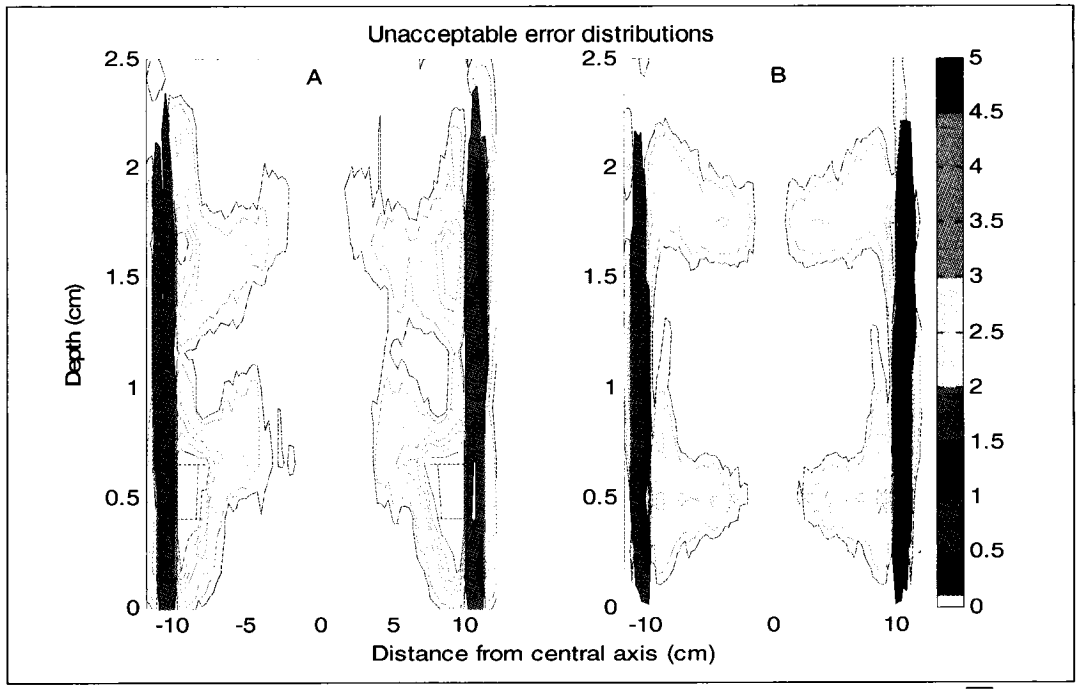


**Figure 6-4:** Unacceptable error distributions for the same case as in Figures 6-2 and 6-3. A $\overline{\theta^2}(0)$ of 0.011 rad$^2$, as in Figure 6-4A, introduces too many errors which exceed 4 % while a $\overline{\theta^2}(0)$ of 0.022 rad$^2$, as in Figure 6-4B, creates some deviations superior to 2 mm in the penumbra region.

Now consider a 6 MeV beam but a field size of 6x6 cm$^2$. In this instance, the tolerable range of mean square scattering angles narrows to 0.014 to 0.018 rad$^2$. It was consistently observed for all energies that the lower limit of the range of acceptable mean square scattering angles was superior for a 6x6 cm$^2$ field than for a 20x20 cm$^2$ field. If a given mean square scattering angle value produced accurate distributions for both 6x6 and 20x20 cm$^2$ fields, distributions describing square fields of dimensions lying between 6 and 20 cm were satisfactory as well.

It was observed that variation of the mean square scattering angle generally produced no significant effect on the central axis depth dose curve. No discernible difference occurred between PDD curves both calculated for a 6 MeV beam and a field size of 20x20 cm$^2$ but with mean square scattering angles of 0.0085 rad$^2$ and 0.034 rad$^2$. All other conditions were equal as well.

### 6.1.2 Mean Energy at the Surface

An appropriate value for the mean surface energy, $\overline{E_0}$, is vital to the quality of the CadPlan-predicted dose distribution. Firstly, as discussed in Chapter 3, the fluence profile at the surface of the phantom is dependent on the scattering power of air, values for which are stored within CadPlan by energy. Furthermore, the width and amplitude fitting parameters $b_i(z)$ and $B_i(z)$, appearing in Eq. (3-1) and (3-2), are also tabulated as functions of energy. Hence, an unsuitable value for $\overline{E_0}$ leads to pencil beam fits that are consistently inaccurate as the thickness of medium is traversed. $\overline{E_0}$ also figures prominently in the CadPlan bremsstrahlung model, as seen in Eq. (3-11). In addition, the attenuation coefficients particular to this model are charted as functions of the mean energy at the surface. Effectively, all aspects of the distribution will be affected by a wrong value for $\overline{E_0}$.

The value of $\overline{E_0}$ will vary depending on what equation was employed as its definition. In this work, Eq. (1-3), using the AAPM-recommended constant of 2.33 $MeVcm^{-1}$, was selected as the standard. However, the mean surface energies predicted by Eq. (1-3) using the slightly larger constant recommended by the Hospital Physicists' Association are not too dissimilar than those values obtained using the AAPM's constant of choice. In addition, mean surface energies obtained via Eq. (1-4) tend to lie within 1 MeV of that provided by the standard over the range of clinical energies. As the above-mentioned definitions of $\overline{E_0}$ are based on the depth of 50% dose, $d_{50}$, changes in the value of this parameter due to variation of field size also affect $\overline{E_0}$. Again, such changes over the majority of the field sizes studied are minor due to the constancy of the percent depth dose curve observed for larger field sizes. Variation of the value of $\overline{E_0}$ due to field size was also found to be within 1 MeV. It was demonstrated for all energies studied that, all other conditions being constant, a change in $\overline{E_0}$ of less than $\pm$ 1 MeV did not significantly deteriorate the predicted distribution. Variation in the distribution was observable but the quality of the distribution remained unchanged. Thus, obtaining a globally appropriate value for $\overline{E_0}$ should present no difficulties to the CadPlan user.

More dramatic variations of the mean surface energy result in large discrepancies between the measured and predicted distributions that violate the modified Van Dyk criteria outlined in Chapter 4. As expected, lower than suitable mean surface energies result in PDD curves with fall-off region slopes that are too elevated and depth of dose maximum appearing at too shallow a depth. The contrary is true for higher than suitable values of $\overline{E_0}$.

### 6.1.3 Virtual Source Distance

The virtual source to reference plane distance, *VSD*, was measured via the Khan method, as described in Chapter 1, for energies and applicator sizes representative of their relevant ranges. Figure 6-5 presents an example of the affine function obtained via the Khan method for a 12 MeV beam of field size 10x10 $cm^2$. In this example, the slope is 0.01 $cm^{-1}$ and the point of measurement, $d_{max}$, was 2.47 cm. A virtual source to phantom surface distance of 98 cm was computed using Eq. (1-7). The virtual source to reference plane distance is thus 93 cm.

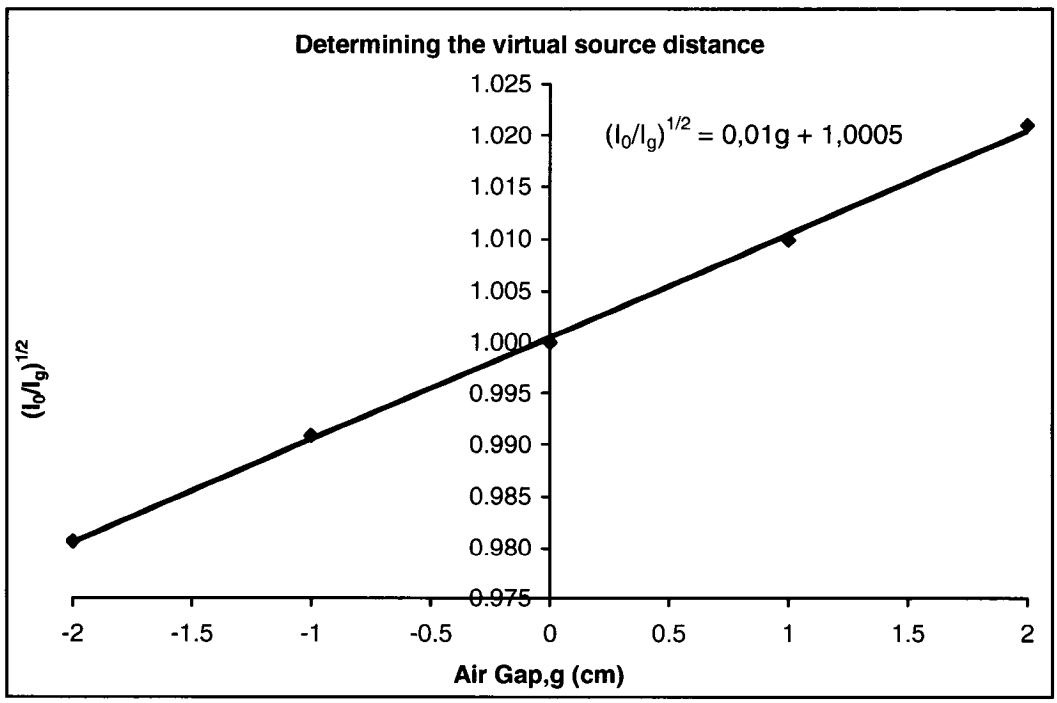


**Figure 6-5:** An example of the function from which the virtual source distance may be obtained. The measurement conditions of this example included a 12 MeV beam and a field size of 10x10 $cm^2$ created with the standard applicator.

Table 6-3 reports the measured virtual source distances. It may be observed that smaller energies and field sizes correspond to smaller virtual source distances. Furthermore, the said increases appear to plateau when medium to large field sizes and beam energies are considered.

| Measured Virtual Source Distances | | | |
|---|---|---|---|
| Energy (MeV) | Field Size ($cm^2$) | | |
| | *6x6* | *10x10* | *20x20* |
| 4 | 50 | 70 | 75 |
| 12 | 70 | 93 | 98 |
| 20 | 75 | 95 | 100 |

**Table 6-3:** Virtual source distances at the reference plane measured with respect to various energies and field sizes created with standard applicators.

Calculated dose distributions were relatively insensitive to the *VSD*. Generally, no significant changes in accuracy were observed for *VSD* values ranging from approximately 50 to 110 cm. The CadPlan manual suggests a value of ten less than the collimator to source distance. In this work, that corresponds to 85 cm, which would be acceptable. Values between 80 and 95 cm were actually selected, with larger values corresponding to larger energies. Figure 6-6 presents two distributions for which all parameters were identical with the exception of very different virtual source distances.

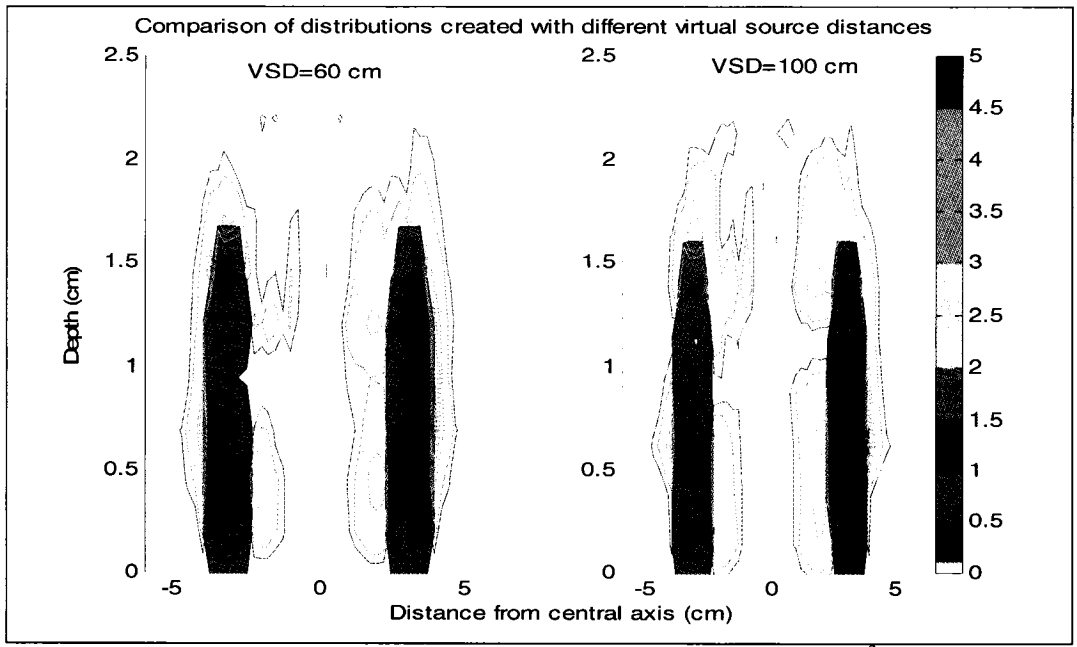


**Figure 6-6:** Error distributions in the case of a 4 MeV beam, a field size of 6x6 $cm^2$ created with the standard applicator, an SSD of 100 cm and orthogonal incidence. Error maps corresponding to virtual source distances of 60 and 100 cm are depicted.

### 6.1.4 Calculation Grid

As related in Chapter 3, four calculation grid options, containing pixels of different sizes (1.25, 2.5, 5 and 10 mm), are available. At the standard SSD, the pencil beam size is 2.5 mm x 2.5 mm. These dimensions are scaled to the distance from the reference plane. Discontinuities are observable in CadPlan-predicted profiles and PDD curves, even under standard conditions with zero gantry angle and a homogeneous phantom. As the pencil beams broaden as they are ray-traced through the electron density matrix, some pixels contain overlapping pencil beams, generating discontinuities. Essentially, primary radiation will be misrepresented, overestimated in some regions and underestimated in others. In the case of PDD curves, the build-up region consistently displayed more noticeable discontinuities than the region of steep dose decline. The first row of the CadPlan matrix is always set to zero, as mentioned in Chapter 3, making the distribution at shallow depths unreliable. Moreover, discontinuities would be more noticeable in the build-up region since smaller rates of change in dose are expected there, causing discontinuities to appear more prominent. Similarly, PDD curves for lower energies, characterized by sharper build-up regions, appeared to be plagued by fewer discontinuities. Discontinuity in the build-up region of a 4 MeV beam typically takes the form of one sharp point at dose maximum. In the case of the build-up region of a 20 MeV curve, several rounder bumps are usually observed.

The use of the smallest pixel size available does not guarantee a more exact dose distribution. Distributions of similar accuracy were produced with pixels of dimension 1.25, 2.5 and 5 mm. The largest pixel size, 10 mm, generated distributions that were often plagued with more regions of larger error. At that size, resolution becomes too poor for reliability to be ensured. Figure 6-7 displays error distributions generated with pixel sizes of 2.5 and 10 mm. For the most part, the distributions are similar but a region of intolerable error appears around a depth of 2 cm when 10 mm pixels were used. Error distributions akin to that produced with 2.5 mm pixels were created with 1.25 and 5 mm pixels.

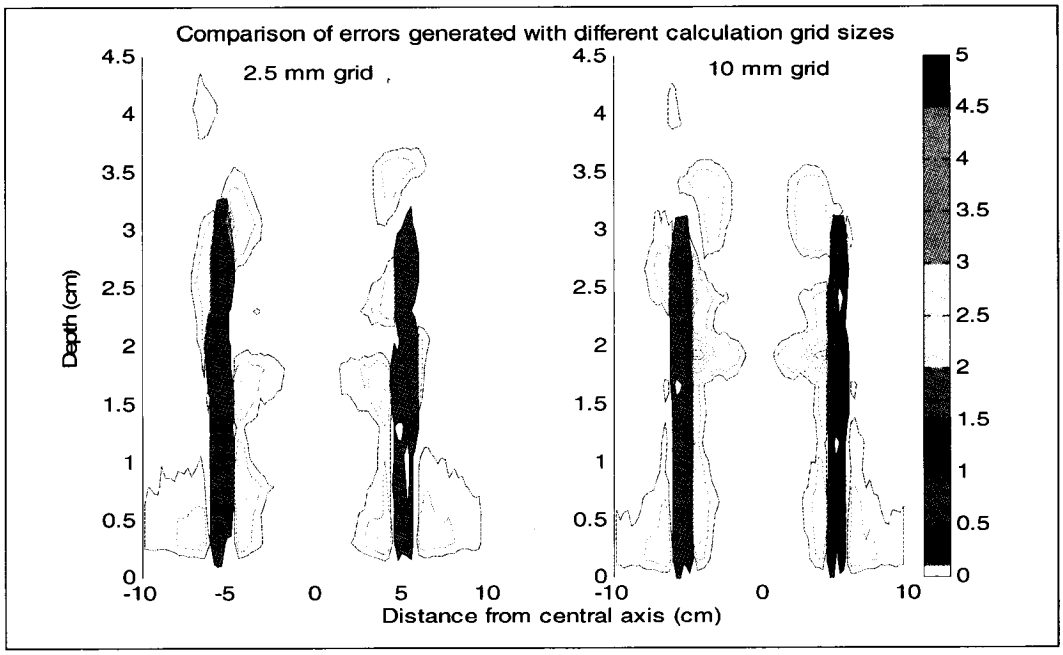


**Figure 6-7:** Error distributions created with all parameters identical with the exception of calculation grid pixel size. The conditions in this example included a 10 MeV, perpendicular incidence, a 10x10 $cm^2$ applicator and an SSD of 100 cm.

Discontinuities in PDD curves created with a smaller pixel size are more numerous but of smaller magnitude. Figure 6-8 exhibits PDD curves created with pixel sizes of 1.25 and 2.5 mm.

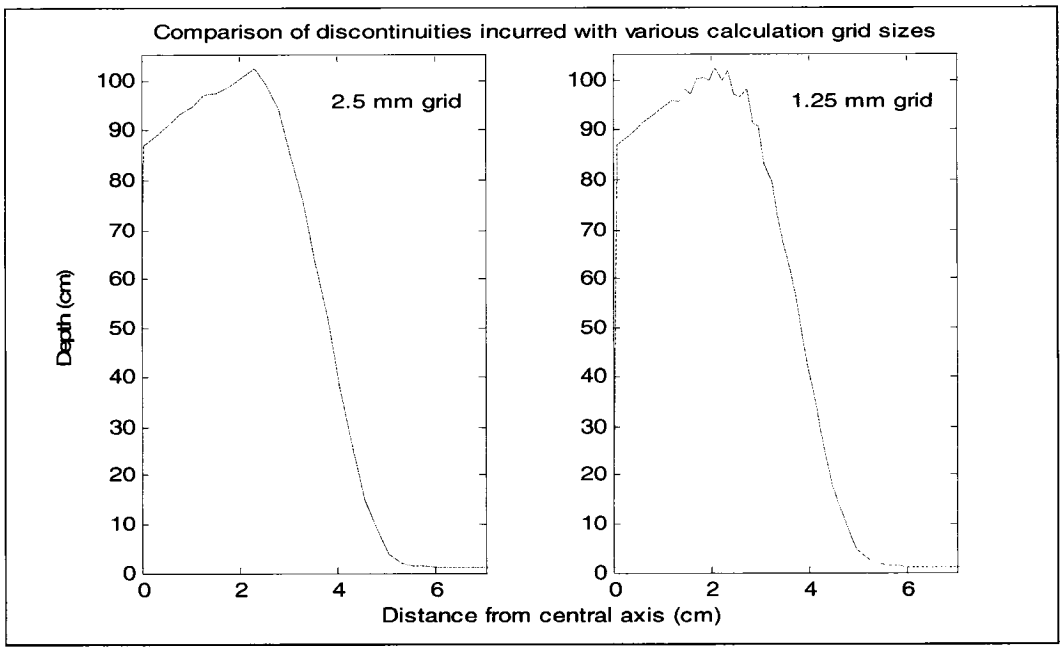


**Figure 6-8:** Central axis PDD curves calculated with all parameters identical with the exception of calculation grid pixel size. The conditions in this example included a 10 MeV, perpendicular incidence, a 10x10 $cm^2$ applicator and an SSD of 100 cm.

Discontinuity problems could be assuaged by allowing the CadPlan user to set the pencil beam size as well as the grid size, ensuring a combination that would minimize this problem. Smaller, more numerous pencil beams would allow for this without having to sacrifice resolution. Today's CPU capacity should not make this a difficult. Another option would be to offer a calculation grid that balloons with pencil beam size as distance from the reference plane is increased, as discussed by Vinceller[6].

CadPlan only allows the user to place the calculation grid with the cursor. This virtually eliminates the possibility of truly consistent grid placement. The shape of a distribution does not usually undergo any observable variations if the calculation grid is replaced in a comparable but non-identical manner. However, the value of dose maximum will differ, although by less than 1 %. Nonetheless, such differences could introduce significant error into the calculation of output factors, as will be addressed later in the chapter.

### 6.1.5 Input Depth Dose Curves

CadPlan requires that large open and blocked field central axis PDD curves be entered by the user for each energy. As evidenced by Eq. (3-2), the open field curve is important in determining dose to a given point. The blocked field curve functions in calculations for the bremsstrahlung component of the beam. In essence, the quality of the calculated distribution depends on the quality of these input curves. Figure 6-9 presents an example of input PDD curves.

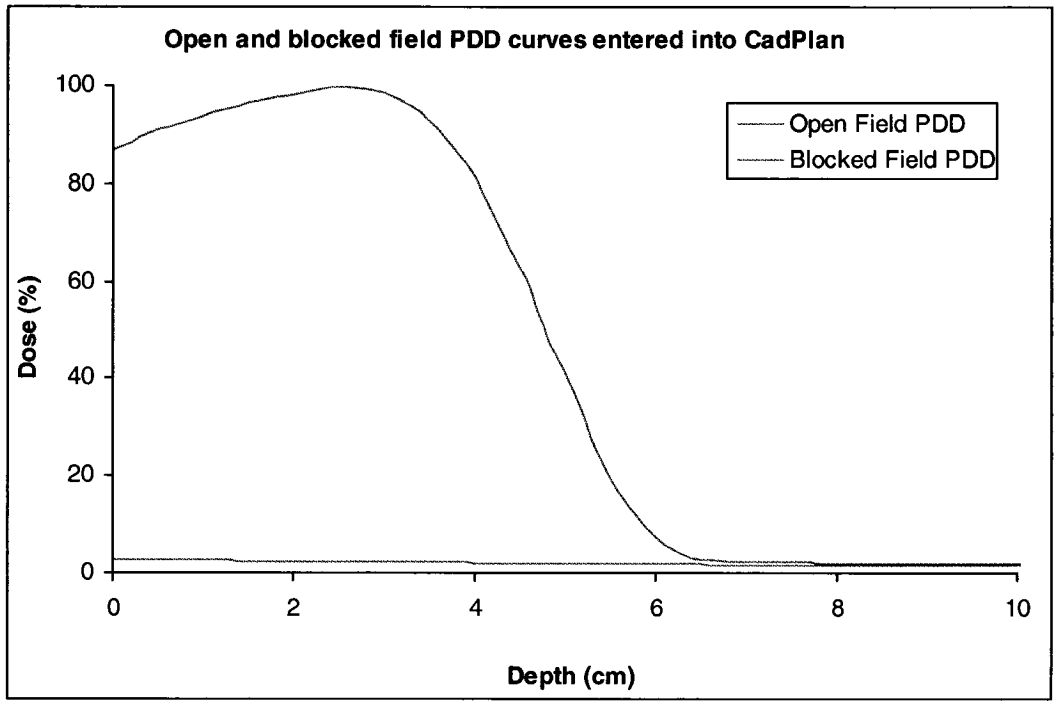


**Figure 6-9:** An example of the open and blocked field PDD curves that must be entered into CadPlan for each energy. The standard 20x20 $cm^2$ applicator was used to create all such curves. A cerrobend block replaced the standard mask in order to create the blocked field. All CadPlan input PDD curves were acquired with an SSD of 100 cm. An energy of 12 MeV was used here.

## 6.2 Homogeneous Phantom – Standard SSD and Gantry Angle

The dose distributions predicted by CadPlan in the case of an homogeneous phantom with a standard SSD of 100 cm and zero gantry angle were in good agreement with the measured distributions. The set tolerances were generally satisfied, allowing CadPlan to be deemed as clinically acceptable under the standard conditions.

Acceptable results that on the whole satisfy the acceptance criteria were steadily observed for nominal electron energies between 4 and 18 MeV, with one virtual machine created per energy. Concurrence between CadPlan and measured distributions for field sizes ranging from 6x6 $cm^2$ to 20x20$^2$, including elongated rectangular fields, was achieved. For all cases of this type, discrepancies in high dose gradient regions (penumbra) were within $\pm$ 2 mm and were within 4 % elsewhere, as stipulated for profiles. In the case of PDD curves, the region of steep dose decline was generally within 1 mm. Larger discrepancies were at times noted in and immediately after the build-up region due to the presence of discontinuities induced by the nature

of the calculation grid as discussed earlier in the chapter. Typical results are displayed in Figures 6-10, 6-11, 6-12 and 6-13. The right-hand side of each figure displays a comparison of central axis PDD curves while the left-hand side illustrates errors in all other regions.

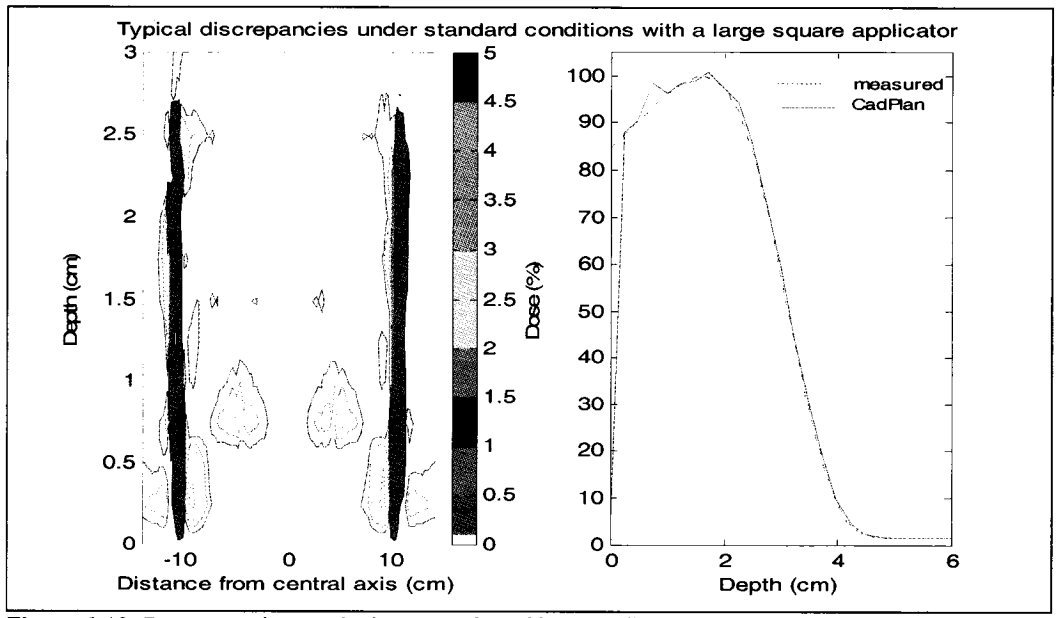


**Figure 6-10:** Representative results in cases of a uniform medium, an SSD of 100 cm, orthogonal beam incidence and a large square field, created with the standard applicator. Conditions in this example included an 8 MeV beam, a 20x20 $cm^2$ field and a 90° collimator angle.

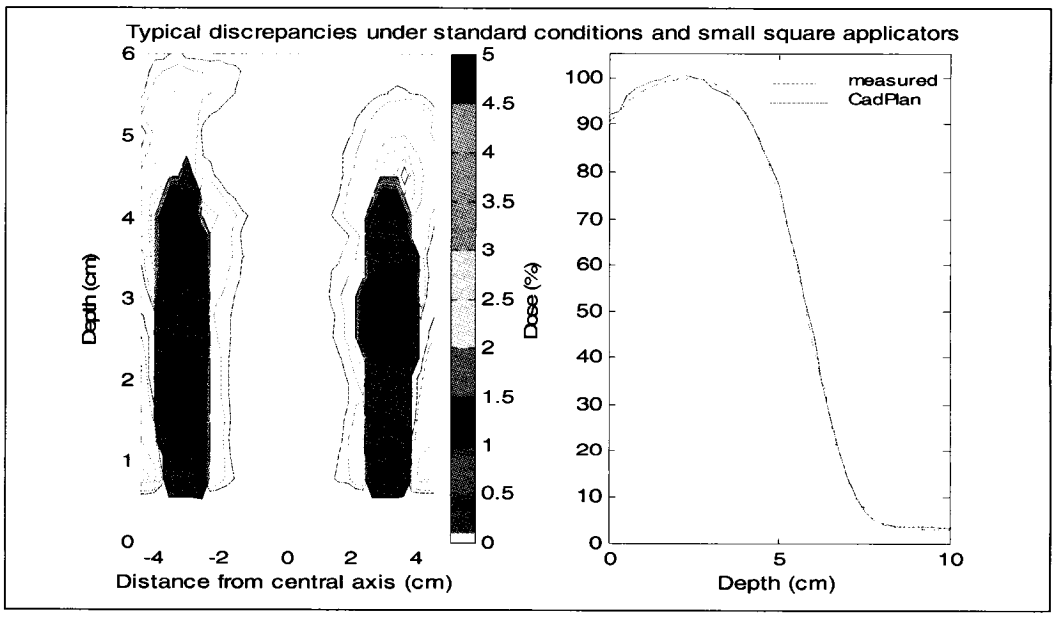


**Figure 6-11:** Representative results in cases of a uniform medium, an SSD of 100 cm, orthogonal beam incidence and a small square field, created with the standard applicator. Conditions in this example included a 15 MeV beam, a 6x6 $cm^2$ field and a 90° collimator angle.

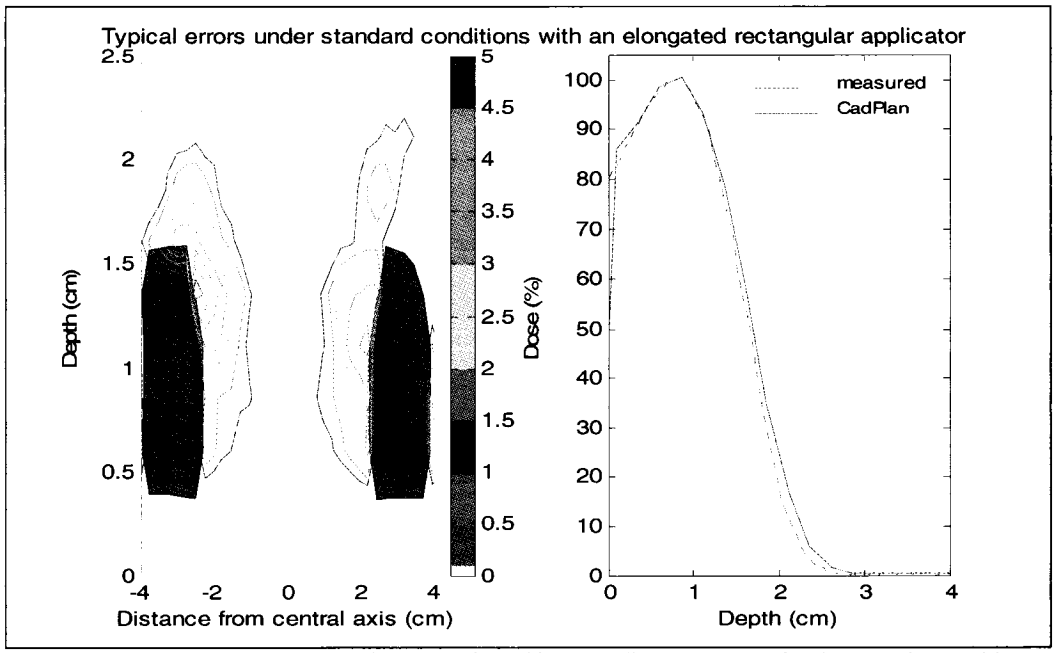


**Figure 6-12:** Representative results in cases of a uniform medium, an SSD of 100 cm, orthogonal beam incidence and an elongated rectangular field, created with the standard applicator. The short side of the applicator lay parallel to the scanning direction. Conditions in this example included a 4 MeV beam, a 6x14 $cm^2$ field and a 90° collimator angle.

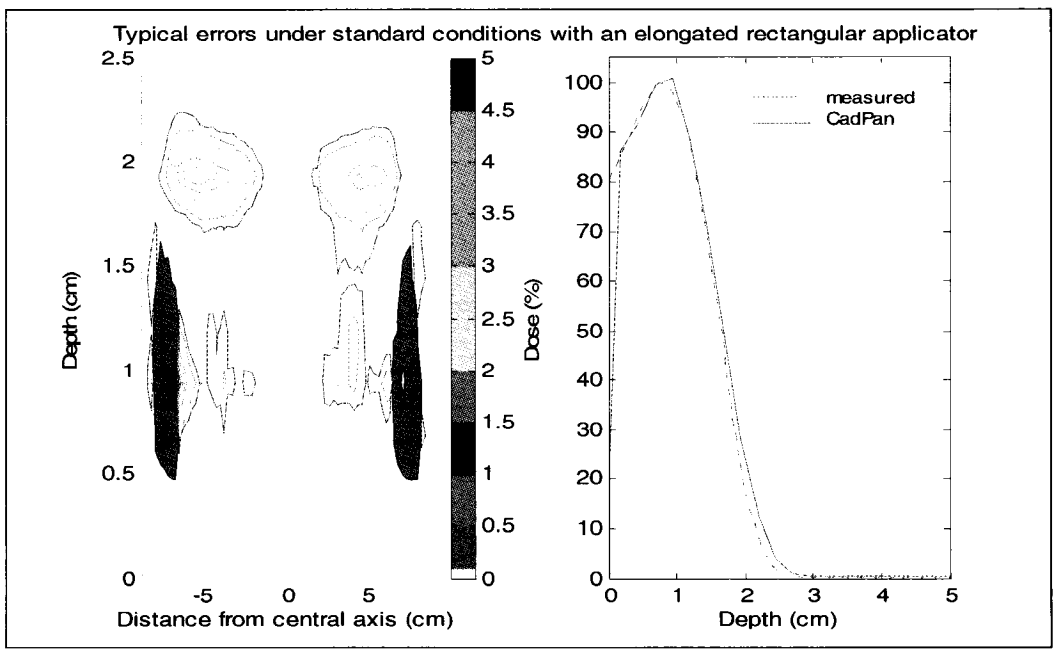


**Figure 6-13:** Representative results in cases of a uniform medium, an SSD of 100 cm, orthogonal beam incidence and an elongated rectangular field, created with the standard applicator. The long side of the applicator lay parallel to the scanning direction. Conditions in this example included a 4 MeV beam, a 14x6 $cm^2$ field and a 0° collimator angle.

Fields created with the largest Elekta applicator, 25x25 $cm^2$, regardless of nominal energy, failed to satisfy the modified Van Dyk criteria. Calculated central; axis PDD curves consistently differed from measured curves by at least 1.2 mm and up to 1.5 mm. The calculated distributions were plagued by large regions of error exceeding 4 %. An example of such deviation is shown in Figure 6-14. Accurate distributions for this field size could be predicted by CadPlan if additional virtual machines were created with different mean square scattering angles, tailored to the 25x25 $cm^2$ applicator.

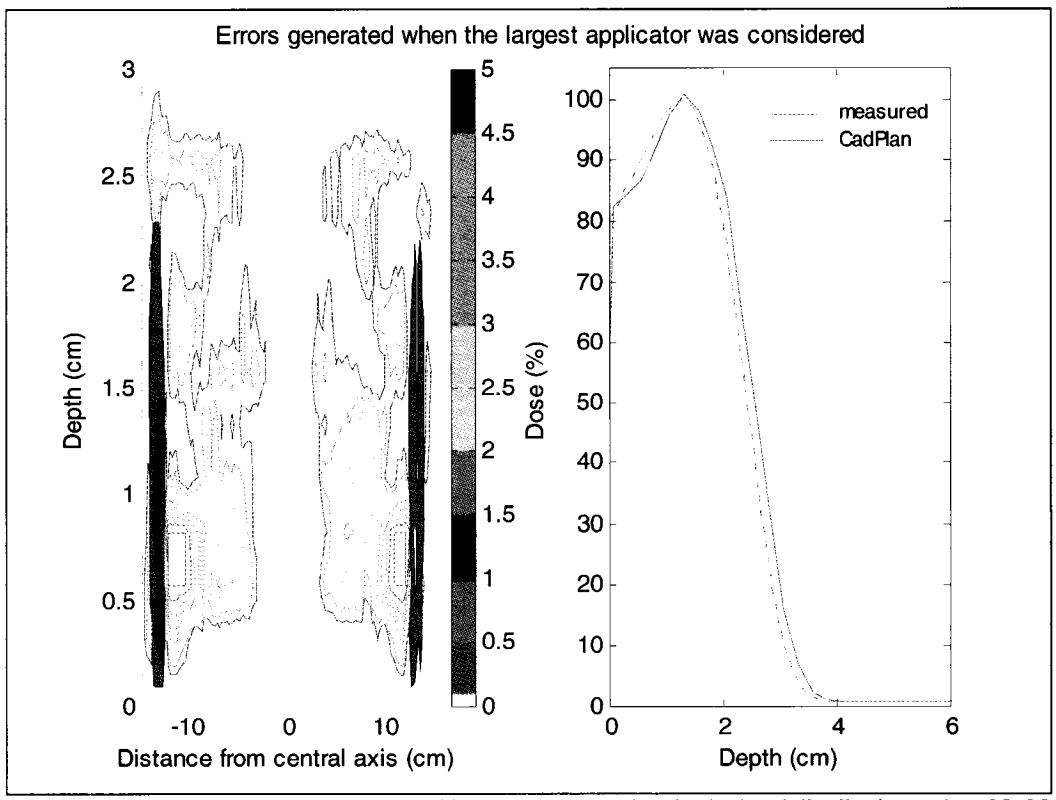


**Figure 6-14:** Typical disparity encountered between measured and calculated distributions when 25x25 $cm^2$ were created with the standard applicator. Conditions particular to this example were a 6 MeV beam, a 90° collimator angle, the standard SSD and perpendicular incidence.

Energies at the upper end of the clinical range, 20 and 22 MeV, proved to be more problematic. As mentioned previously, two virtual machines with different mean square scattering angles were necessitated for each of these energies in order to obtain satisfactory distributions for applicator sizes between 6x6 and 20x20 $cm^2$. Even so, in the case of fields of size 6x6, 6x10 and 6x14 $cm^2$ (created by their respective applicators), CadPlan-predicted distributions underestimated the dose in regions of

shallow depths at distances relatively large from the central axis. As illustrated in Figure 6-15, acceptance criteria were not strictly met in such regions. Nevertheless, these distributions were deemed satisfactory as the measured dose in these regions was very low, typically below 5 %. The predicted distributions in these cases were consistently acceptable in all medium and high dose regions.

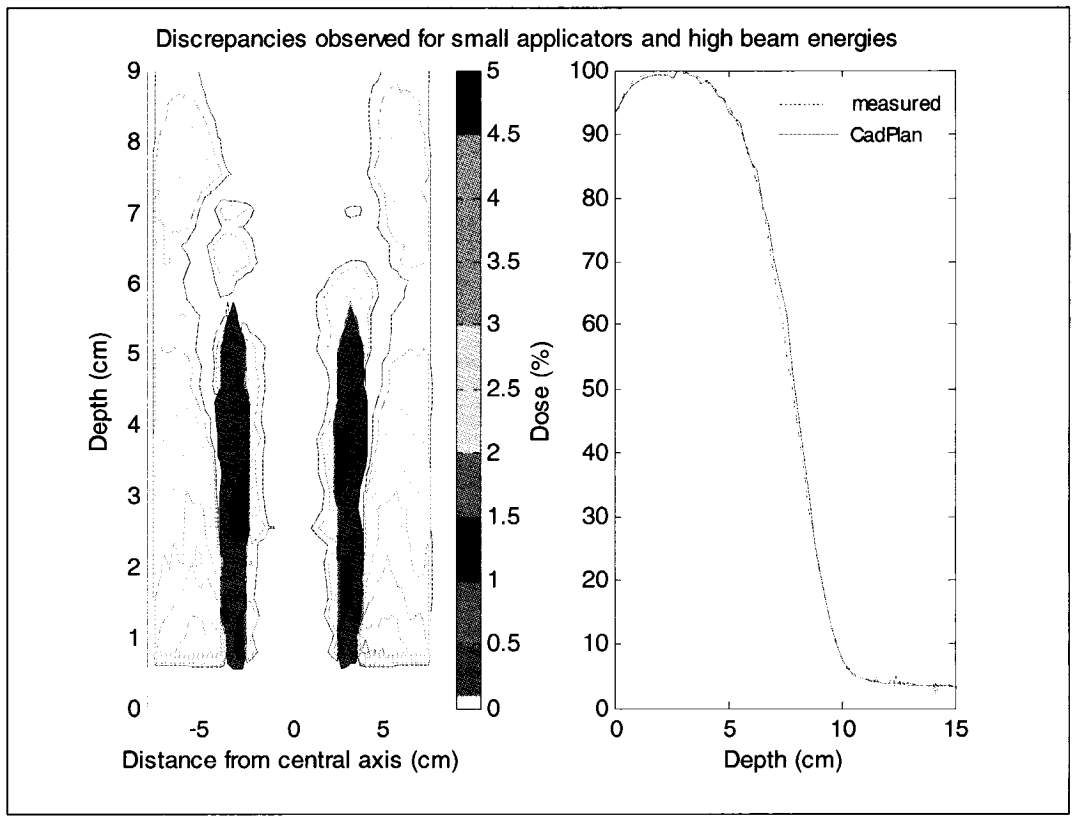


**Figure 6-15:** Typical discrepancies obtained with energies of 20 and 22 MeV and applicators of size 6x6, 6x10 and 6x14 $cm^2$. The conditions pertaining to this example included a 20 MeV beam, a field size of 6x10 $cm^2$, created with the standard applicator, a collimator angle of 90°, an SSD of 100 cm and a non-angled gantry.

Fields were also created with the aid of cerrobend inserts employed with the 10x10 $cm^2$ applicator. For the most part, errors were within the set tolerances. Figure 6-16 presents typical results. In the case of small circular fields, of diameters 2, 3 and 4 cm, some PDD curves were characterized by slightly larger discrepancies around the build-up region. This could be due to the fact that for these field sizes each pencil beam accounts for a more significant portion of the field, magnifying discontinuity errors. The largest circular field created with an insert, of diameter 10 cm, was in accordance with measured data for all energies studied. It should be noted

that even 2 cm diameter fields for energies of 20 and 22 MeV conformed well to the set tolerances, unhindered by the type of error displayed in Figure 6-15. Therefore, that type of error is more applicator dependent than field size dependent.

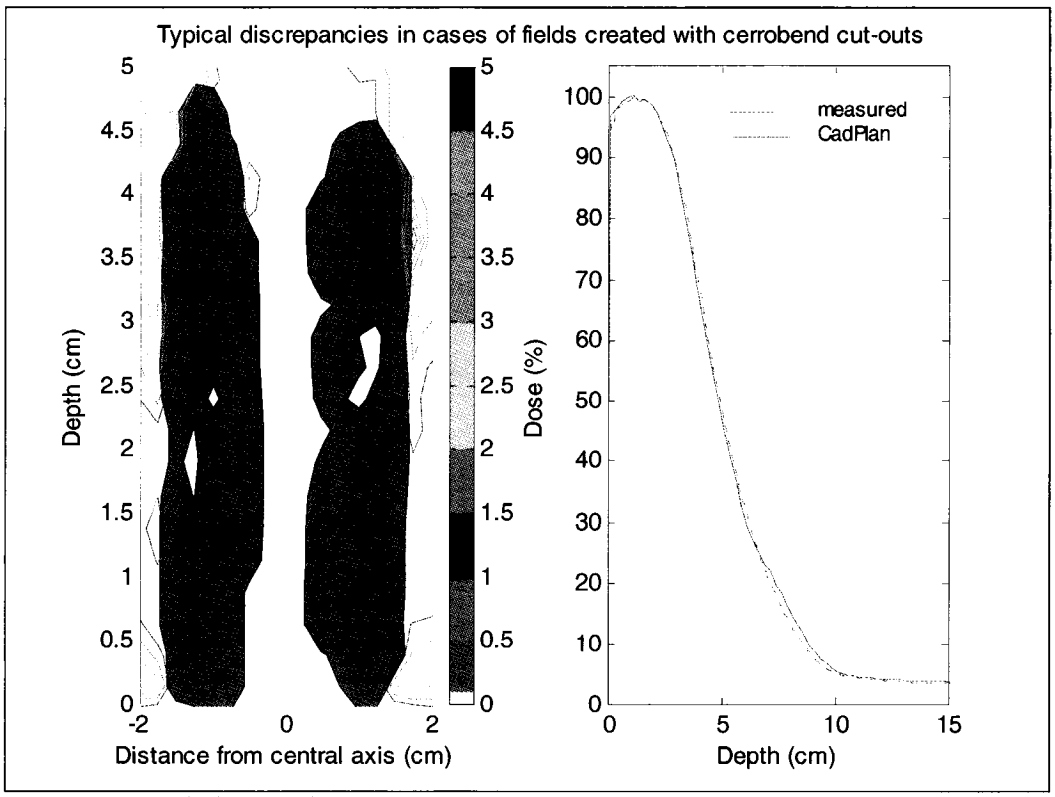


**Figure 6-16:** Typical errors observed when comparing measured and calculated distributions in cases of circular fields created with cerrobend cut-outs inserted into the 10x10 $cm^2$ applicator. The conditions of this example included a 20 MeV beam, and a cut-out of diameter 2 cm. The standard SSD was used as well as a collimator angle of 90°.

### 6.3 Homogeneous Phantom – Varied Source to Source Distances

CadPlan's capacity to predict dose distributions in the instance of non-standard source to surface distances in the clinical range (98-102 cm) was investigated. Acceptance criteria were satisfied for low and high energies, as well as for both small and large fields, for all of the SSDs tested. Figure 6-17 displays typical results.

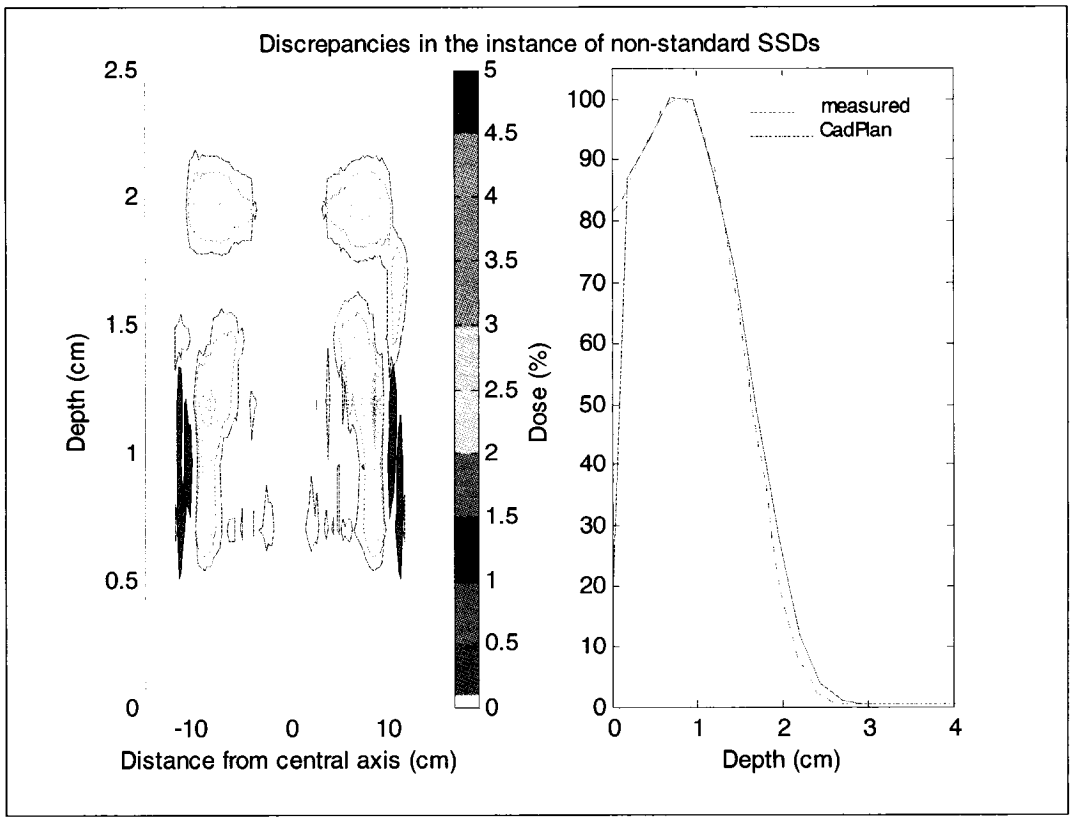


**Figure 6-17:** An example of errors in the case of SSDs in the range 98-102 cm. The conditions of this particular instance include a 4 MeV beam, a 20x20 $cm^2$ field, an SSD of 102 cm, a 90° collimator and perpendicular beam incidence.

## 6.4 Homogeneous Phantom – Varied Gantry Angle

Greater distortion of profiles due to discontinuity was observed in cases of oblique incidence. The values of the fitting parameters utilized by the algorithm are taken from discrete tables that go with depth. In the case of the perpendicularly incident beam, the same depth will have been traversed across the field, for a profile taken at a certain point along the central axis depth dose curve. The situation is not the same in a case of non-zero gantry angle. Consider a profile taken orthogonally to the beam direction at a given depth. At that particular depth, different thicknesses of medium will have been traversed at every point of the field. The tabulated values of the fitting parameters are discrete, thus discontinuities will arise since the values will move suddenly from one to the other. Samuelsson et al.[7] suggested that interpolation between tabulated values would eliminate such discontinuities. It was observed in the current study that as the gantry angle was increased, the predicted distribution

worsened in terms of profile discontinuity. This result was as to be expected as a larger gantry angle implies greater differences of thickness passed through in the case of a given profile, thus accentuating jumps from one tabulated value to another. Figure 6-18 evidences the amplification of profile discontinuity that accompanies an increase in gantry angle.

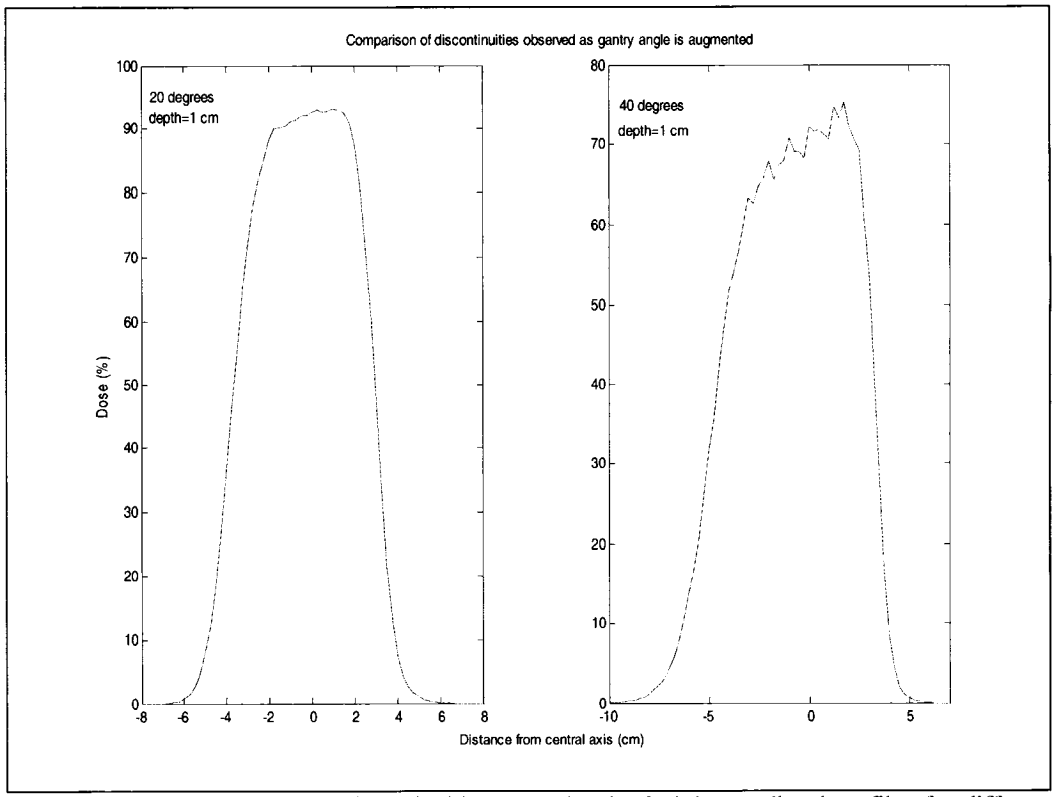


**Figure 6-18:** A comparison of discontinuities appearing in CadPlan-predicted profiles for different gantry angles. The conditions in this example included a 4 MeV beam, a 6x6 $cm^2$ field, the standard treatment distance and gantry angles of 20° and 40°. Profiles shown were taken at a depth of 1 cm.

CadPlan performed in a satisfactory manner, with errors lying mainly within the set tolerances, when asked to compute distributions involving large fields and gantry angles of 10° and 20°. Figure 6-19 displays results representative of such conditions.

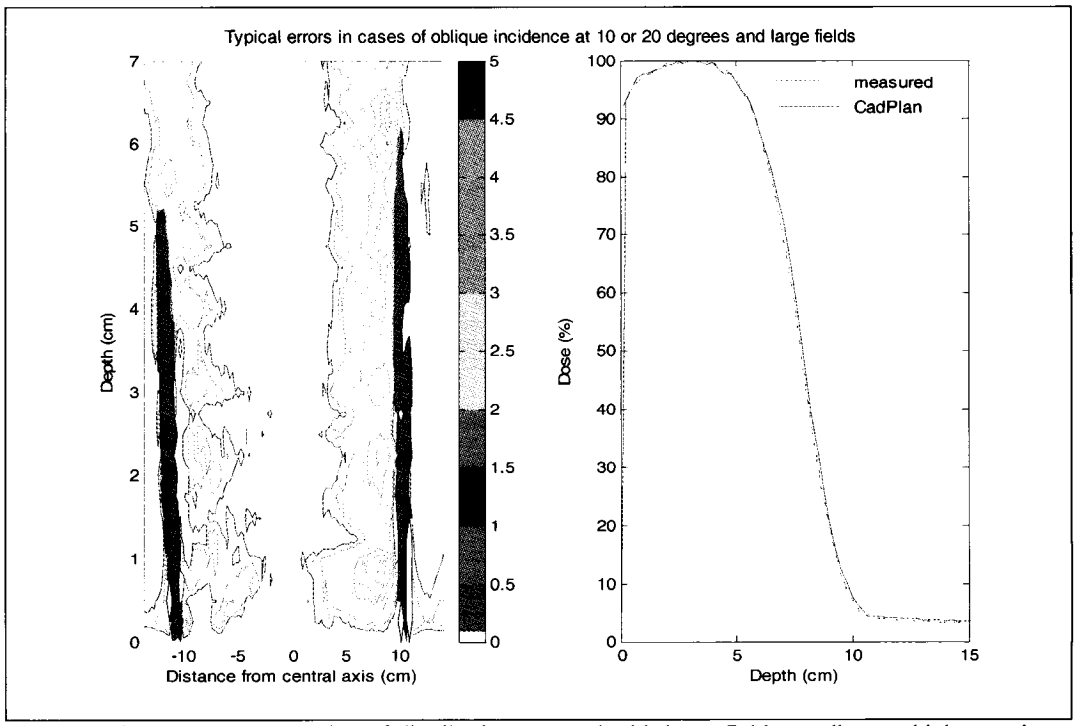


**Figure 6-19:** Errors representative of distributions created with large fields, medium to high energies and gantry angles up to 20°. The measurement conditions in this example included a 20 MeV beam, a field size of 20x20 $cm^2$, produced with the standard applicator, an SSD of 100 cm and a gantry angle of 10°.

The penumbra on either side of a 20x20 $cm^2$ field, incident upon the phantom at 10° or 20°, exhibited very good agreement with measured profiles. Error in the case of these larger fields for energies 8, 12 and 20 MeV, took the form of a slight undervaluation of dose at the extremities of the high-dose low gradient region. However, such disparities were seldom larger than 3 %.

Conversely, CadPlan modeling of large fields with the same obliquity but of energy 4 MeV revealed somewhat greater inaccuracy. CadPlan demonstrated a tendency to exaggerate the obliquity of 4 MeV profiles at depths shallower than (approximately) the depth of 80 % dose, leading to an overestimation of dose at the field edges. Beyond this depth, profiles were construed as more parallel to the surface than in actuality. These deviations, situated at the peak of a given profile, at times exceeded the limits of acceptability, overestimating or underestimating dose by up to 7 %, but such errors appeared in only very few isolated regions. In general, however, these deviations were of magnitudes less than 5 %. Figure 6-20 exemplifies a worst case scenario.

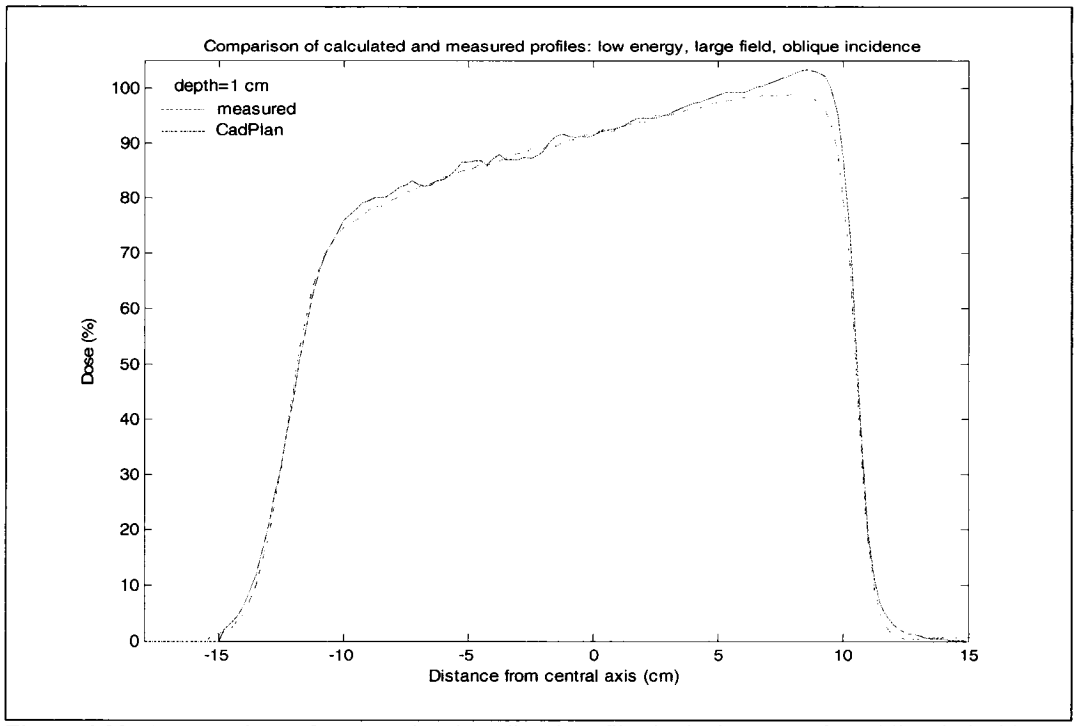


**Figure 6-20:** A comparison of measured and predicted profiles in the instance of an obliquely incident large field, low energy beam. Conditions included a 4 MeV beam, a field size of 20x20 $cm^2$, an SSD of 100 cm and a gantry angle of 20°.

On the whole, CadPlan-predicted distributions of large field, obliquely incident beams of energy 4 MeV may still be considered as fair, although tolerances are exceeded in some regions. The penumbrae of these distributions are well described and the majority of profiles exhibit a good fit along the slanted portion of the profile. The corresponding PDD curves were in concurrence with measured data as well.

Disparities which exceed the limits of acceptability were also observed in the case of distributions involving 6x6 $cm^2$ fields and a 20° angle of incidence for all four energies tested (4, 8, 12 and 20 MeV). For these small fields, the penumbra region situated on the side of the high peak of a given profile was consistently in outstanding agreement with that of the measured curve. Conversely, the penumbra region on the side of the lower end of the profile's high-dose low-gradient region tended to be wider than that of the measured data. Hence, the dose on that side was somewhat exaggerated at virtually all depths. Discrepancies in this region were at most 2.5 mm in high gradient regions. In some lower gradient regions, the dose was also overvalued beyond the set limits. These discrepancies were mostly situated in regions of low or

medium dose and were mainly inferior to 5 %. The largest percentage error encountered was 7 % in the instance of a 12 MeV beam. Interestingly, the 4 MeV beam, which proved most problematic for large field sizes, corresponded to the best small field distribution, with no high-gradient region errors superior to 1.5 mm in the case of 20° incidence. PDD curves for all energies demonstrated adequate accuracy, with larger errors only appearing in the build-up region, due to discontinuity. The worst build-up region error encountered occurred with an 8 MeV beam and is displayed in Figure 6-21. Results representative of distributions typically achieved with obliquely incident small fields are presented.

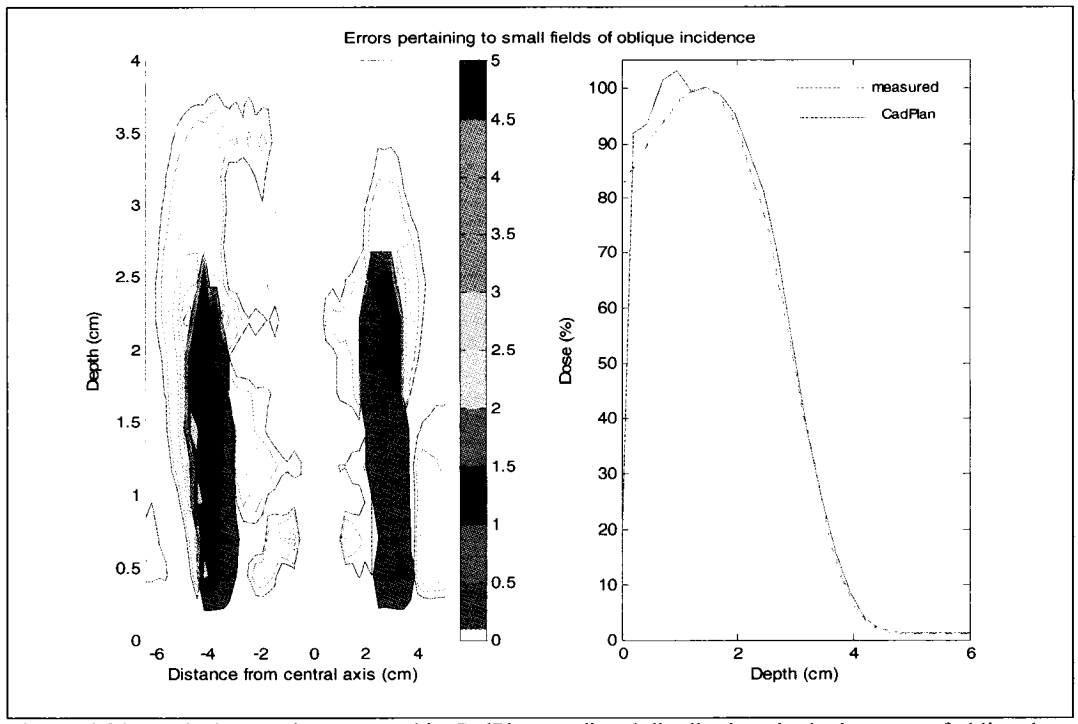


**Figure 6-21:** Typical errors incorporated in CadPlan-predicted distributions in the instance of obliquely incident small fields. This example included an 8 MeV beam, a field size of 6x6 $cm^2$, an SSD of 100 cm and a gantry angle of 20°.

More disparity was evidenced with small fields a gantry angle of 40°. The overestimation of the width of the penumbra on one side was also seen in this case but was more pronounced. Errors were generally of the same magnitude as those observed for small fields and incidence at 20° but they infested much larger portions of the distributions. Central axis PDD curves, however, still conformed to the acceptance criteria. An example of the observed deviations typical at all depths is depicted by Figure 6-22.

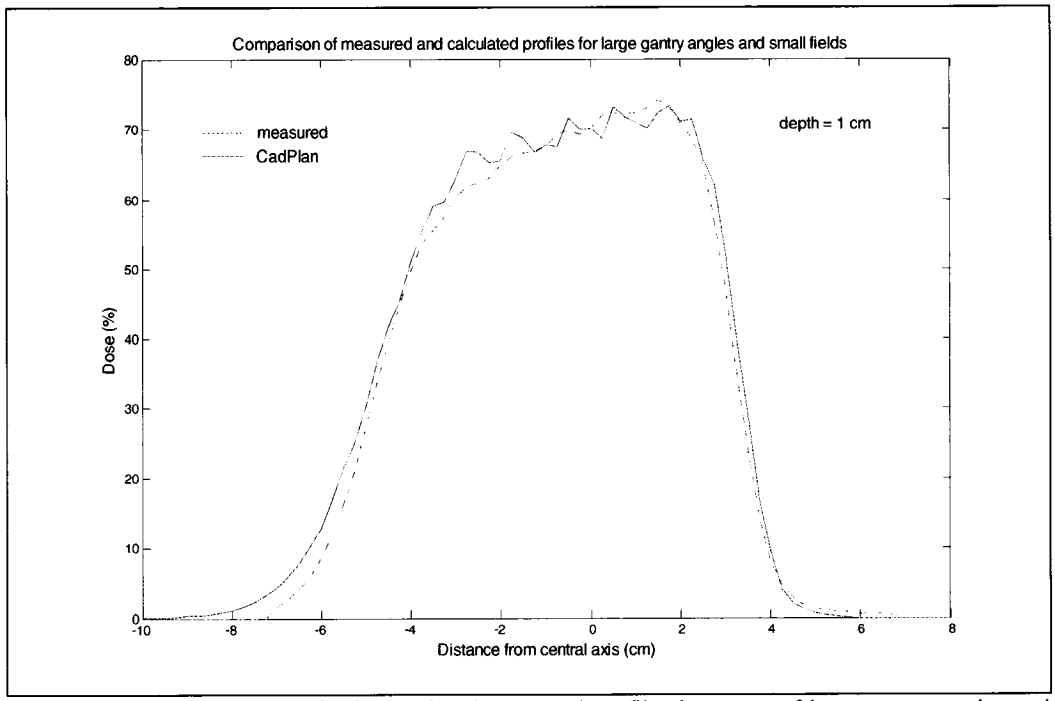


**Figure 6-22:** A comparison of calculated and measured profiles instances of large gantry angles and small fields. The conditions of this example included a 4 MeV beam, a 6x6 $cm^2$ field, the standard SSD and a gantry angle of 40°.

The side of the profile plagued by large discrepancies corresponds to that side of the applicator situated further from the water surface when the gantry is angled. As pencil beam dimensions are scaled to the distance from the base of the applicator to the surface, pencil beams striking the surface will be of varying dimensions. The largest pencil beams will be located towards the field edge farthest from the surface. Overestimation of dose due to many instances of pencil beams overlapping one another on that side of the field may be responsible for the observed discrepancies. This possibility explains why the same type of error, but of reduced magnitude, appeared in the instance of a smaller gantry angle. In that case, the reference plane to surface distances would, evidently, also vary across the field. However, the difference between the closest and farthest distances to the surface, and thus pencil beam dimensions, would be smaller, reducing pencil beam overlaps. As shown earlier, the same discrepancies were present for large fields incident at 20°. A possible explanation lies in the fact that each field is uniformly divided into pencil beams of dimension 2.5 mm. Correspondingly, a 20x20 $cm^2$ field will be described by over ten times more pencil beams that a 6x6 $cm^2$ field. Hence, the dose calculated at each point

in a larger field will be made up of many more contributions. In that case, there is more chance that pencil beam overlaps will be counteracted by more realistic contributions to the same point.

Ultimately, CadPlan is unsuitable for large gantry angles. Discontinuities in this case became overwhelming and dose was consistently overestimated beyond the tolerances on one side of the penumbra. CadPlan may be considered passable for smaller angles of incidence, since most regions of a given distribution in those cases met the tolerances. Much of the error incorporated in calculated distributions involving an angled gantry could probably be eliminated by using pencil beams of smaller dimensions. Moreover, allowing the user more freedom in the definition of pencil beam and calculation grid sizes could permit large discontinuities to be avoided.

### 6.5 Presence of Heterogeneities

CadPlan's ability to predict central axis PDD curves in the presence of slab inhomogeneities was investigated. Calculated curves generally deviated from measured data by at most 1.5 mm. The modified Van Dyk criteria stipulated accordance between measured and calculated curves to be within 1 mm. Hence, although CadPlan is capable of performing in a reasonable manner when faced with heterogeneities, it lacks the precision required to be deemed fully clinically reliable. Comparable results were obtained in all cases tested, regardless of: beam energy (4, 12 or 20 MeV), field size (6x6 $cm^2$ or 20x20 $cm^2$), whether bone or lung constituted the heterogeneity, the thickness of the heterogeneity (0.5 or 3 cm when bone was studied, 3 or 7 cm when lung was studied), the depth at which the heterogeneity lay ($d_{max}$, $d_{80}$ or $d_{50}$). Figure 6-23 displays typical results.

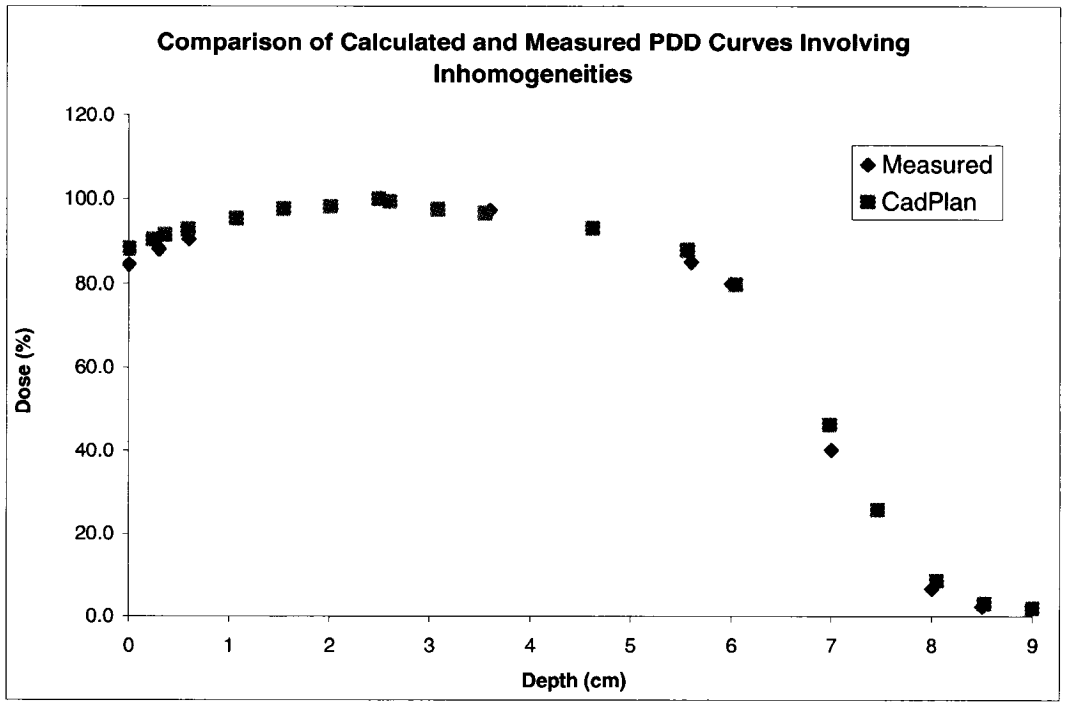


**Figure 6-23:** Typical deviations between calculated and measured central axis PDD curves in the presence of slab inhomogeneities. Conditions pertaining to this example included a 12 MeV beam, a 20x20 $cm^2$ field, the standard SSD and a zero gantry angle. A lung heterogeneity, of thickness 3 cm, was positioned at the nominal $d_{max}$ (2.6 cm) of the central axis PDD in the case of a uniform phantom.

The errors incorporated into calculated PDD curves may stem various sources. Firstly, it is assumed that the angular distributions on both sides of an interface are equivalent, which is not strictly true. Secondly, CadPlan scales inhomogeneities to equivalent depths in water by multiplying the thickness of a heterogeneous layer by the ratio of that material's stopping power to that of water, as shown by Eq. (3-5). This formula provides that thickness of water in which the same amount energy will be lost as in the layer of inhomogeneity. However, this procedure does not ensure that the same mean square angular spread will be generated by the heterogeneous layer and its equivalent thickness of water. The effective thickness of water which would result in identical mean square angular spreads, $t_{ang}$, is given by[8]:

$$t_{ang} = \frac{T_i}{T_m}, \tag{6-3}$$

where $T_i$ and $T_m$ are the linear scattering powers of the inhomogeneity and medium, respectively. Naturally, the equivalent thickness defined by Eq. (6-3) does not

necessarily fulfill the condition that an equivalent amount of energy will be lost in the effective thickness, $t_{ang}$, as in the physical thickness, $t$. . In fact, if the atomic number of the inhomogeneity differs from that of the medium, it becomes impossible for the two definitions of equivalent thickness to equate to one another. The error introduced in the mean square angular spread by using an equivalent thickness based on energy loss, $\Delta\overline{\theta^2}$ , may be expressed as[8]:

$$\Delta\overline{\theta^2} = T_i t - T_m t_e , \tag{6-4}$$

where $t_e$ corresponds to the equivalent thickness based on energy loss and $t$ is the physical thickness of a given layer of heterogeneity. The addition of this correction factor to the CadPlan algorithm may ameliorate, to some extent, CadPlan's performance with respect to inhomogeneity corrections. The coefficient of equivalent thickness (CET) method was employed to determine the equivalent thicknesses of inhomogeneities for the measured data. This method is based on beam absorption and thus also propagates a lack of equality between the mean square angular spreads of the true inhomogeneity and the water equivalent thickness. Although dose differences due to angular spread are inherent in the raw measurements, scaling by energy loss alone will cause the converted data to be somewhat in error as well. Furthermore, Eq. (3-5) and (6-3) assume that the energy variation is small over physical thickness of the inhomogeneity[8]. Therefore, overly large thicknesses of inhomogeneity may introduce additional error. Nonetheless, large regions of inhomogeneity characterized some of the test phantoms (3 cm of bone or 7 cm of lung) and the errors recorded in these cases were similar to those obtained with smaller heterogeneous regions. Thus, this potential source of error does not present too much clinical relevance. Obviously, the same types of discontinuities (due to pencil beam overlapping and a lack of interpolation between values in stored tables) intrinsic to calculated curves for a uniform medium are still present under non-uniform conditions. Discrete stopping power tables may lead to additional error by producing slightly off equivalent thicknesses. Furthermore, the electron density is evaluated at the same depth increments appearing in fitting parameter tables. Therefore, CadPlan's view of the depth of an inhomogeneity may be inaccurate. Electron density will be evaluated every millimetre for energies inferior than 10 MeV. It will be assessed progressively

less frequently for higher electron energies. For energies superior to 35 MeV, electron density will be evaluated every 3.5 mm. Essentially, CadPlan may not realize that a given pencil beam is traversing a heterogeneity until the beam is well within the region. This oversight may skew the central axis dose distribution in a significant manner as it will effectively cause a shift of the PDD curve at the depth of the heterogeneity. Bremsstrahlung is added to the calculated distribution after inhomogeneity corrections have been performed. Thus, the influence of heterogeneities on bremsstrahlung production is ignored. Materials of larger atomic number do incite increased bremsstrahlung levels. Yet, the resultant discrepancies would still be rather small. Perhaps one of the most significant effects caused by the presence of higher atomic number inhomogeneities is electron backscatter. CadPlan does not account for this phenomenon. Backscatter increases with atomic number and decreases with beam energy. At a bone-water interface, the dose may be augmented by as much as 8 %, for clinical beams, due to the presence of bone[9]. Naturally, backscattered electrons will also influence the dose upstream from the interface. Interestingly, even in the case of a bone inhomogeneity and a beam of 4 MeV, where the largest dose discrepancy at the interface would be expected, the largest recorded error was only 1.3 mm. As previously mentioned, similar errors, measured in millimetres, were recorded for all cases tested. This observation may be explained by the fact that this lowest clinical energy boasts the steepest gradient. The percentage error at the interface was 12.9 %.

In instances where the difference between the physical thickness of the inhomogeneity and the equivalent thickness of water is relatively large, an inverse square correction may be applied to account for this difference. However, in the case of biological materials, even bone and lung, this correction tends to be inferior to one percent. In addition, this correction was not applied to measured data so by neglecting it similar errors were generated in both the measured and the calculated curves.

When considering heterogeneities in the human body, as opposed to slab phantoms, sources of additional error arise. When a pencil beam encounters an inhomogeneity and the corresponding dose is calculated, it is assumed that the heterogeneity is of infinite lateral extent. This assumption may become problematic when faced with inhomogeneities which are narrow and long in the direction of the

beam. For example, the nasal septum is bounded by long, slim air passageways. Ding et al. studied CadPlan's ability to predict the dose distribution when complex heterogeneities are involved[10]. In the case of an intricate trachea and spine phantom, CadPlan was able to predict the location of hot and cold spots in the distribution but failed considerably at calculating the magnitude of the dose in these regions. The experimenters also tested a phantom which included an aluminium slab. CadPlan was unable to cope with this condition. No stopping power data for mediums of density higher than those of the biological materials are included in the algorithm. Moreover, CadPlan sets an upper limit on the electron density; 2.12 times that of water[10]. This action is not described in the CadPlan manual. CadPlan is thus completely unsuitable for patients with metal plates.

Other pencil beam algorithms employ more complicated techniques to calculate dose distributions involving heterogeneities. For example, Shiu and Hogstrom subdivided each pencil beam into different energy bands in order to approximately transport the complete angular and energy distribution from each calculation point[11]. Yu et al. designed a multiray model which creates a typical mean path from the origin of each pencil beam to each calculation point[12]. The downfall of this model is that it requires calculation times which exceed those of CadPlan-type algorithms by up to four orders of magnitude[13]. Long calculation times are impractical in a clinic. Furthermore, the Monte Carlo method is unquestionably much more accurate than any electron pencil beam model, thus the only real advantage offered by pencil mean models is reasonable calculation times. Jette described a model that solves the second-order multiple scattering equation which describes scattering power as position dependent[14]. In reality, the energy distribution at a given point in a patient may be quite broad, making it incorrect to assume a distinct value for scattering power, as is required by the initial conditions of this model. These more complex models address some of the sources of error intrinsic to the CadPlan algorithm. However, they still generate errors which are too high to allow electron models to be relied upon clinically to the same degree as photon beam planning; functioning as the primary tool for plan creation and selection. In his review article of electron beam treatment planning, Hogstrom aspires to an accuracy of 3 %[13]. Even the most sophisticated models do not attain this degree of accuracy in every situation. Complex heterogeneity-correction models also tend to require more assumptions (as in the case

of Jette's model). Therefore, they may eliminate some error seen with more basic models but often introduce other errors which may result in only moderate improvement in accuracy. The majority of pencil beam models use pencil beam dimensions similar to those employed in CadPlan. In order to achieve the level of accuracy necessitated before electron beam treatment planning may become fully integrated as a clinical tool, smaller pencil beams are demanded. It is unreasonable to expect accuracy down to 1 mm or a few percent in the modeling of real anatomy when the pencil beam dimensions themselves are at least twice this margin of error.

In addition to smaller pencil beams, CadPlan's performance involving heterogeneities could be improved by including backscatter factors in the algorithm. This addition could boost the accuracy of predicted distributions around complex bone structures such as the spine and ribs. The gross underestimation of dose seen around hot spots in the CadPlan distribution reported in the work of Ding et al. was likely to be at least partially due to CadPlan's ignorance of backscatter at interfaces. Accuracy could also be enhanced by including interpolation between points in fitting parameter tables. Additionally, CadPlan should evaluate the electron density of the medium more frequently, perhaps at every 0.2 mm.

### 6.6 Output Factors

CadPlan is unable to predict output factors with any reasonable accuracy. Errors approaching 10 % were recorded for some field sizes. This result was to be expected; CadPlan has no way of accounting for the component of output factor values that originates from jaw position. As delineated in Chapter 1, the jaws assume different positions depending on the applicator that is fitted to the treatment head and the energy selected. The CadPlan user sets the field size at the normal source to surface distance. Consequentially, the assumption that jaw position plays no role in dose determination, or alternatively, that jaw position is identical for a given applicator regardless of energy, is implicit to the algorithm. It was mentioned earlier in the chapter that the placement of the calculation grid has a relatively minor effect ($< 2$ %) on the value of the maximum dose. However, these differences become important when computing output factors. Table 6-4 presents typical errors:

| Comparison of Measured and Calculated Output Factors | | | | |
|---|---|---|---|---|
| Applicator ($cm^2$) | | Energy (MeV) | | |
| | | *6* | *10* | *18* |
| *6x6* | Measured | 0.924 | 0.996 | 1.073 |
| | CadPlan | 0.969 | 0.985 | 0.987 |
| | Error (%) | 4,9 | -1.1 | -8,0 |
| *10x10* | Measured | 0.990 | 1.021 | 1.043 |
| | CadPlan | 0.988 | 0.994 | 0.999 |
| | Error (%) | -0.2 | -2.6 | -4.2 |
| *6x14* | Measured | 0.953 | 1.007 | 1.039 |
| | CadPlan | 0.975 | 0.973 | 0.989 |
| | Error (%) | 2.3 | -3.4 | -4.8 |

**Table 6-4:** Comparison of output factors derived from measurements and those calculated by CadPlan for a variety of applicator sizes and energies. Conditions included an SSD of 100 cm and a non-angled gantry.

CadPlan is able to predict cut-out factors with greater accuracy since jaw position remains constant; different field sizes are created by placing various masks in the same applicator. Ding et al. found agreement to within 2% between measured and calculated cut-out factors for energies in the clinical range[10]. They used cut-outs of size 3x6 $cm^2$ to 8x8 $cm^2$ in a 10x10 $cm^2$ Elekta SL series applicator. In this work, cut-out factors for masks used with the 10x10 $cm^2$ applicator to create circular fields of diameters 2, 3, 4 and 10 cm were tested. A grid size of 2.5 mm was employed. Results concurred with those of Ding et al. with the exception of the smallest field, for which the calculated cut-out factors deviated from measurement by up to 5 %. The grid was not moved when the cut-out factors for each energy were obtained. Table 6-5 presents typical results.

| Comparison between measured and calculated cut-out factors | | | | |
|---|---|---|---|---|
| | Field Diameter (cm) | | | |
| | *2* | *3* | *4* | *10* |
| Measured | 0.788 | 0.874 | 0.935 | 0.998 |
| CadPlan | 0.814 | 0.882 | 0.923 | 1.000 |
| Error (%) | 3.3 | 0.9 | 1.3 | 0.2 |

**Table 6-5:** Representative discrepancies between measured and CadPlan-calculated cut-out factors for energies in the clinical range. Conditions in this example included an 8 MeV beam and 10x10 $cm^2$ applicator into which masks perforated by circular apertures of various sizes were inserted. A zero gantry angle and an SSD of 100 cm were employed in all cases.

Cut-out factors for the smallest field also appeared more sensitive to grid displacement than those for the larger fields. Changes in grid position forced the cut-

out factors calculated for the smallest field to vary quite significantly. Only reasonable grid positions were tested. A calculation grid of 2.5 mm was repositioned several times. The cut-out factor corresponding to an 8 MeV beam and a circular field of diameter 2 cm, created by a mask inserted into the 10x10 $cm^2$ applicator, was calculated for each grid position. Most positions resulted in cut-out factors ranging from 0.813 to 0.816. However, one position led to a value of 0.831 for this cut-out factor. When a grid size of 1.25 mm was tested for the same cut-out, an even higher value, 0.846, was obtained for one trial. Smaller changes were noted with increasing field diameter. The field of diameter 2 cm probably appeared more sensitive for two reasons: a) a smaller number of pencil beams cover the aperture than for larger fields, making every discontinuity more influential and b) larger fields are characterized by larger output factors, making similar changes less significant. Although calculated cut-out factors for most fields do achieve 2 % accuracy, CadPlan may still not be considered reliable enough to predict cut-out factors for clinical use. More accuracy is required for cut-out factors than for whole distributions and relatively large errors created by grid placement and grid size are too strong a possibility. Ultimately, an electron beam treatment planning system could only be capable of accurately determining output factors if the electron beam pertaining to the specific accelerator concerned, at the base of the applicator, was extensively modeled. Janssen et al. investigated the possibility of such modelling[15].

### 6.7 Verification of CadPlan for a Real Patient

In addition to photon fields, 20 MeV electrons were prescribed as boost irradiation to treat a patient presenting a tumour in the right inguinal region. The tumour was situated between a few millimetres and 1.7 cm from the surface of the patient, depending on the body contour. The ellipsoidal tumour's dimensions were roughly 5 cm in depth and 7 cm in length. An irregularly-shaped cerrobend mask of an approximate diameter of 7.6 cm was designed for the 10x10 $cm^2$ applicator. The gantry was set to zero degrees and an SSD of 100 cm was used. Apart from soft tissue differences, bone was present only several centimetres in depth beyond the 10 % isodose line. No bolus was necessary. The physician desired 90 % dose at 6 cm depth. In order to verify that the prescribed treatment realized this demand, measurements were performed using Solid Water™ and a PTW Markus chamber. The dose was

measured at depths of concern. The dose distribution was calculated in CadPlan and the central axis PDD curve was extracted. CadPlan-calculated values were in reasonable agreement with measurement. Table 6-6 below reports the measured and calculated doses:

| Comparison of Measured and Calculated Doses | | | |
|---|---|---|---|
| Depth (cm) | Measured Dose (%) | CadPlan Dose (%) | Difference (%) |
| 2 | 100 | 98 | -2 |
| 2.3 | 100 | 98.4 | -1.6 |
| 5.7 | 89.5 | 92.0 | -2.5 |
| 6 | 86.5 | 88.5 | 2 |

**Table 6-6:** Comparison of measured and calculated doses around dose maximum and 90 % dose along the central axis in the case of a real patient. The treatment included a 20 MeV beam, a mask of irregular shape, used in the 10x10 $cm^2$ applicator, an SSD of 100 cm and non-angled gantry. No bolus was used.

However, CadPlan's shortcomings were also reiterated in this case. Near the surface, that is, at depths inferior to 0.5 cm, CadPlan calculated doses that were far too low, exemplifying the futility of this model when precision at shallow depths is demanded. Wave-like discontinuities also blemished the build-up region, although their magnitudes were small; within 0.2 %. In this case, CadPlan was able to predict the output factor with reasonable accuracy. The CadPlan-derived value was 0.984 while the measured value was 0.995.

## 6.8 References


1. Huizenga, H., Storchi, P.R.M., *The in-air scattering of clinical electron beams as produced by accelerators with scanning beams and diaphragm collimators*, Phys Med Biol 32, p. 1011-29, 1987.

2. van Battum, L.J., Huizenga, H., *On the initial angular variances of clinical electron beams*, Phys Med Biol 44, p. 2803-20, 1999.

3. van Battum, L.J., van der Zee, W., Huizenga, H., *Scattering from applicators in clinical electron beams,* Phys Med Biol 48(15), p. 2493-2507, 2003.

4. Varian, *CadPlan manual: External beam modelling physics v 6.0*, 1999.

5. International Commission on Radiation Units and Measurement (ICRU), Report No 35, *Radiation Dosimetry: Electron Beams with Energies Between 1 and 50 MeV*, 1984.

6. Vinceller, S., *Validation du système de planification de traitement THERAPLAN Plus pour des faisceaux d'électrons,* mémoire de recherche, maîtrise, Université Paul Sabatier, Toulouse, 1999.

7. Samuelsson, A., Hyödynmaa, S., Johansson, K.A., *Dose accuracy check of the 3D electron beam algorithm in a treatment planning system*, Phys Med Biol 43(6), p. 1529-1544, 1998.

8. Brahme, A., Lax, I., *Absorbed dose distribution of electron beams in uniform and inhomogeneous media*, Acta Radiol Suppl 364, p. 61-72, 1983.

9. Klevenhagen, S.C., *Physics of Electron Beam Therapy*, Adam Hilger, Ltd., Bristol, 1985.

10. Ding, G.X. et al., *Evaluation of a commercial three-dimensional electron beam treatment planning system*, Med Phys 26(12), p. 2571-80, 1999.

11. Shiu, A.S., Hogstrom, K.R., *Pencil-beam redefinition algorithm for electron dose distributions*, Med Phys 18(1), p. 7-18, 1991.

12. Yu, C.X., Ge, W.S., Wong, J.W., *A multiray model for calculating electron pencil beam distribution*, Med Phys 15(5), p. 662-671, 1988.

13. Hogstrom, K.R., Starkschall, G., Shiu, A.S., *Dose calculation algorithms for electron beams*, AAPM Advances in Radiation Oncology Physics, Medical Physics Monograph No. 19, p. 900-924, 1992.

14. Jette, D., Bielajew, A., *Electron dose calculation using multiple-scattering theory: Second-order multiple scattering theory*, Med Phys 16(5), p. 698-711, 1989.

15. Janssen, J.J., et al., *A model to determine the initial phase space of a clinical electron beam from measured beam data*, Phys Med Biol 46(2), p. 269-286, 2001.

# Chapter 7

# Conclusions and Future Work

## 7.1 Summary of Results and Suggestions

CadPlan functioned in an extremely satisfactory manner with regard to homogeneous media and a non-angled gantry. Discrepancies generally lay within the limits of the set tolerances. Of course, at depths shallower than 0.5 cm, CadPlan proved to be completely unreliable, as expected, since the algorithm sets the values of all the pixels in the first row of its calculation matrix to zero. In addition, discontinuities induced by pencil beam size and the calculation grid were more apparent around the build-up region. CadPlan successfully calculated distributions for non-standard SSDs in the range of common clinical use (98-102 cm). When asked to tackle distributions involving an angled gantry, CadPlan failed to satisfy the acceptance criteria. Large field, small gantry angle distributions were generally adequate. Increased error was found in cases of small fields obliquely incident at larger angles. Overestimations of up to 2.5 mm in high gradient regions and up to 7 % in areas of lower gradient were observed. These deviations were typically situated on the side of the distribution at which the applicator was farther from the surface. More dramatic discontinuities were also observed in profiles describing fields of oblique incidence. The instance and magnitude of discontinuities rose with gantry angle. Interestingly, most central axis PDD curves produced by CadPlan were in good accordance with measurement. When computing central axis PDD curves for slab phantoms, CadPlan performed in a fair manner but exceeded the set tolerances. CadPlan is incapable of predicting output factors with any reasonable accuracy.

Ultimately, CadPlan electron beam treatment planning is not exact enough to be relied upon clinically in the same fashion as its photon beam counterpart. Nonetheless, its level of accuracy is such that it is suitable to play a larger role in the clinic. Electron beam treatments are most often verified by central axis measurements around the prescription isodose with a non-angled gantry and ignorance of heterogeneities. Effects of oblique incidence are often verified in a rough way by performing one or two measurements at critical depths. CadPlan-calculated central

axis depth dose curves, even in cases of oblique incidence, demonstrated sufficient accuracy to be useful either by supplying additional information or as an independent check. Although CadPlan did not satisfy the acceptance criteria pertaining to inhomogeneities, it functions well enough to provide a good sketch of how a distribution will be altered by the presence of heterogeneities. As heterogeneities are typically not accounted for at all in the clinic, information provided by CadPlan, though not extremely accurate, will provide a better picture of the true dose distribution than ignoring heterogeneities altogether. CadPlan may also supply the user with information on the dose distribution as a whole, which may prove to be useful since the central axis PDD curve is generally the focus of measurements. It was demonstrated that CadPlan is quite accurate, satisfying acceptance criteria, in cases of uniform medium and perpendicular incidence. Thus, predicted distributions may be especially useful for patient cases fulfilling these criteria, such as the example presented in Section 6.7. Calculated distributions particular to cases involving large gantry angles should be considered with caution. However, they may still be used to provide a rough estimate of how dose will be distributed in the patient, especially if the user is aware of and considers regions of known overestimation. Essentially, CadPlan is not fit to replace measurement, particularly of output factors, nor may it be relied on absolutely. It is accurate enough to act as a source of supplementary information or as an extra verification.

The majority of CadPlan's inaccuracy appears to stem, not from the algorithm itself, but from its computer implementation. Problems seen in cases of oblique incidence and non-uniform media, in addition to the discontinuities seen in general, could be alleviated by altering pencil beam and grid size. Pencil beams of dimension 2.5 mm are far too large to attain the high accuracy necessitated for a treatment planning system to assume clinical responsibility. Pencil beam dimensions should be perhaps ten times smaller. This change would not be problematic, considering today's computer power. Furthermore, additional error could be avoided by providing a wide selection of pencil beam and calculation grid sizes which the user could mix and match to minimize discontinuity. Interpolation between points in stored tables would also remove some discontinuity. Errors in cases of heterogeneous media could be diminished by more frequent evaluation of electron density by the algorithm. This practice would reduce errors induced by misevaluation of the depth at which

heterogeneities lie. CadPlan's performance in cases of heterogeneities involving complex bone structures could be ameliorated by incorporating electron back scattering factors in the algorithm. Such an addition would account for amplified doses at interfaces, which become especially important when bone contours are intricate. Most of the CadPlan input parameters were user-friendly, easily determined for a given energy and fitting for the entire range of desired field sizes. Unfortunately, this was not the case for one of the most critical parameters, the mean square scattering angle. Firstly, a value for this parameter that generated acceptable distributions for all applicator sizes ranging from 6x6 $cm^2$ to 25x25 $cm^2$, for a given energy, was unattainable. For most energies, with the exception of those at the high end of the clinical range, one mean square scattering angle value was found to be adequate for applicators up to 20x20 $cm^2$. Nevertheless, greater accuracy could certainly have been achieved if more than one value for this parameter could be entered per energy. Of course, the user could create several virtual machines of the same energy with various mean square scattering angles to be employed with different applicator sizes but this solution would be impractical for users. Both accuracy and usability could be improved if CadPlan allowed at least three mean square scattering angles to be entered per energy. The user could easily determine these values from penumbra measurements for different applicator sizes and would save time trying to determine what one value is most globally satisfactory.

### 7.2 Reflection

Electron beams occupy a unique niche in the radiotherapy clinic and now represent a very common treatment option. While photon beam treatment planning has long been a staple clinical tool, electron beam planning is still too unreliable to be used routinely without reservations. The emergence of the electron pencil beam algorithm, like that employed by CadPlan, arose in the early eighties. This family of algorithms is based on Fermi-Eyges theory; the multiple scattering behaviour of the electron beam approximates a Gaussian distribution. It was thought that by the twenty-first century electron beam algorithms would be fully functional and constitute an integral part of the clinical process. Unfortunately, the goal of 3 % accuracy under all conditions has remained elusive.

CadPlan is clinically acceptable in cases involving homogeneous media and perpendicular beam incidence. However, when the gantry is positioned at larger angles, serious discrepancies were noted between calculated and measured distributions. Interestingly, PDD curves, even for the worst case scenarios essentially remained satisfactory. CadPlan was able to predict PDD curves for phantoms involving simple heterogeneity with some success, within 1.5 mm. Nevertheless, this type of error would be considered less than optimal in the clinic. All CadPlan-calculated curves demonstrate some discontinuity. More severe discontinuities were seen under non-standard conditions. Many of the errors incorporated in the calculated distribution stem from these discontinuity problems and could be assuaged by implementing interpolation between values in the tables stored in CadPlan, allowing more options for pencil beam and calculation grid size and, in cases of heterogeneities, more frequent evaluation of electron density. CadPlan was completely unable to reasonably predict output factors. In order for this task to be accurately performed, some description of the initial phase space particular to the linac concerned would be required. Some investigators are examining this possibility. In most clinical cases treated with electron beams, photon fields are also prescribed. Head and neck cancers, for example, sometimes require adjoining photon and electron fields. It would therefore be interesting to investigate the degree of exactness to CadPlan describes the junction between fields of different type.

Ultimately, CadPlan is not reliable enough to be used in the same manner clinically as its photon counterpart. It is, however, accurate enough to provide supplementary information and a general idea of how dose will be distributed in a given case. Nonetheless, with Monte Carlo treatment planning on the horizon, the electron pencil beam algorithm will soon become extinct.

## Index of References


Abou Mandour, M., Nüsslin, F., Harder, D., *Characteristic functions of point monodirectional electron beams*, Acta Radiol Suppl 364, 1983. *52*

Almond, P.R.et al., *AAPM's TG-51 protocol for clinical reference dosimetry of high-energy photon and electron beams*, Med Phys 26(9), 1999. *65, 67*

Bjarngard, B.E., Piontek, R.W., Svensson, G.K., *Electron scattering and collimation system for a 12-MeV linear accelerator*, Med. Phys. 3(3), 1976. *10*

Brahme, A., Lax, I., *Absorbed dose distribution of electron beams in uniform and inhomogeneous media*, Acta Radiol Suppl 364, 1983. *54, 126, 127*

Brahme, A., Lax, I., Andreo, P., *Electron beam dose planning using discrete Gaussian beams: Mathematical background*, Acta Radiol Oncol, 20(2), 1981. *47*

Brahme, Anders, *Geometric parameters of clinical electron beams*, Acta Radiol Suppl 364, 1983. *15*

Brahme, Anders, Svensson, Hans, *Specification of electron beam quality from the central-axis depth absorbed-dose distribution*, Med Phys 3(2), 1976. *16, 17, 19, 20, 21*

British Journal of Radiology (BJR), Supplement 25, *Central Axis Depth Dose Data for Use in Radiotherapy: 1996. 17, 21.*

Burns, D.T., Ding, G.X., Rogers, D.W.O., *$R_{50}$ as a beam quality specifier for selecting stopping-p ratios and reference depths for electron dosimetry*, Med Phys 23(3), 1996. *67*

Ding, G.X. et al., *Evaluation of a commercial three-dimensional electron beam treatment planning system*, Med Phys 26(12), 1999. *92, 129, 131*

Ding, G.X., Rogers, D.W.O., Mackie, T.R., *Mean energy, energy-range relationships and depth-scaling factors for clinical electron beams*, Med Phys 23(3), 1996. *69*

Ding, G.X., Yu, C.W., *Determination of percentage depth-dose curves for electron beams using different types of detectors*, Med Phys 28(3), 2001. *85*

Dosetek, *NACP chamber*, serial number : 1479. *65*

Ekstrand, K. E., Dixon, R.L., *The problem of obliquely incident beams in electron-beam treatment planning*, Med Phys 9(2), 1982. *25*

Eleckta Users Manual 1994. *6, 7, 8, 9, 11, 13.*

Eyges, L., *Multiple scattering with energy loss*, Phys Rev, 74, 1948. *47*

Fermi, as quoted by Rossi, B., Greisen, K., *Cosmic ray theory*, Rev Mod Phys 13, 262-309, 1941. *46*

Grusell, E., Rikner, G., *Radiation damage induced dose rate non-linearity in an n-type silicon detector*, Acta Radiol Oncol 23, 1984. *84*

Hogstrom, K.R., Starkschall, G., Shiu, A.S., *Dose calculation algorithms for electron beams*, AAPM Advances in Radiation Oncology Physics, Medical Physics Monograph No. 19, 1992. *129*

Huizenga, H., Storchi, P.R., *The in-air scattering of clincal electron beams as produced by accelerators with scanning beams and diaphragm collimators*, Phys Med Biol 32(8), 1987. *55, 97, 101*

International Commission on Radiation Units and Measurement (ICRU), Report No 35, *Radiation Dosimetry: Electron Beams with Energies Between 1 and 50 MeV*, 1984. *10, 16, 18, 19, 21, 23, 25, 39, 41, 42, 43, 44, 45, 46, 47, 68, 99, 100*

International Commission on Radiation Units and Measurement (ICRU), Report No 50, *Prescribing, Recording, and Reporting Photon Beam Therapy*, 1993. *20*

Janssen, J.J., et al., *A model to determine the initial phase space of a clinical electron beam from measured beam data*, Phys Med Biol 46(2), 2001. *132*

Jatinder, R., Palta, Inder K., Daftari, K., M. Ayyangar, N. Suntharalingham, *Electron beam characteristics on a Philips SL 25*, Med. Phys. 17(1) 1990. *10*

Jette, D., Bielajew, A., *Electron dose calculation using multiple-scattering theory: Second-order multiple scattering theory*, Med Phys 16(5), 1989. *129*

Karzmark, C.J., Nunan, Craig S., Tanabe, Eiji, *Medical Electron Accelerators*, McGraw-Hill, Inc., New York, 1993. *4, 6, 7, 11*

Keithley, *35040 Therapy Dosimeter*, serial number : 68396. *67*

Khan, Faiz M, *The Physics of Radiation Therapy*, Williams & Wilkins, Baltimore, 1994. *17, 24, 26, 27, 72*

Khan, Faiz M. et al., *Clinical electron beam dosimetry: Report of the AAPM Radiation Therapy Committee Task Group No. 25*, Med Phys 18(1), 1991. *17, 18, 19, 23, 24, 26, 27, 68*

Klevenhagen, S.C., *Physics and Dosimetry of Therapy Electron Beams*, Medical Physics Publishing, Madison, 1993. *81, 82, 83, 93*

Klevenhagen, S.C., *Physics of Electron Beam Therapy*, Adam Hilger, Ltd., Bristol, 1985. *7, 10, 13, 14, 15, 16, 17, 20, 23, 26,35, 38, 43, 45, 46, 81, 82, 83, 92, 128*

Knoll, G.F., *Radiation Detection and Measurement*, John Wilely & Sons, New York, 1989. *83, 84*

Lax, I., Brahme, A., Andreo, P., *Electron beam dose planning using Gaussian beams : Improved radial dose profiles*, Acta Radiol Suppl 364, 1983. *52, 53, 54, 57*

Mott, N.F., Massey, H.S.W., *The theory of atomic* collisions, Claredon Press, Oxford, 1965. *32, 36*

Pfalzner, P.M., Clarke, H.C., *Radiation parameters of 6 to 20 MeV scanning electron beams from the Saturne linear accelerator*, Med. Phys. 9(1), 1982. *10*

PTW-Freiburg, *Markus chamber*, serial number : N23343-1569. *65*

Rikner, G., *Characteristics of a p-Si detector in high energy electron fields*, Acta Radiol Oncol 24, 1985. *84*

RMI, *Solid Water™*, water, lung, bone substitutes. *67*

Rossi, Bruno, *High energy particles*, Prentice-Hall, New York, 1952. *33, 34, 35, 43*

Samuelsson, A., Hyödynmaa, S., Johansson, K.A., *Dose accuracy check of the 3D electron beam algorithm in a treatment planning system*, Phys Med Biol 43(6), 1998. *60, 119*

Scanditronix, *GR-p BS p-type diodes for electron beams and corresponding reference diodes*, serial numbers : F1934, F1940. *65*

Schmidt, R., *Medizinische Strahlenphysik V: Dosimetrie mit Ionisationskammern*, http://www.uke.uni-hamburg.de *19*

Scott, W.T., *The theory of small angle multiple scattering of fast charged particles*, Rev. Mod. Phys. 35, 1963. *33*

Shiu, A.S., Hogstrom, K.R., *Pencil-beam redefinition algorithm for electron dose distributions*, Med Phys 18(1), 1991. *129*

Sorcini, B.B., Hyödynmaa, S., Brahme, A., *Quantification of mean energy and photon contamination for accurate dosimetry of high-energy electron beams*, Phys Med Biol 42 (10), 1997. *59, 60*

Taumann, L., *The treatment head design for medical linear accelerators*, IEEE trans. Nuc. Sci., NS-328, 1981. *10*

Thomas, R.L., Shaw, J.E., *Radiation measurements with diode detectors*, Phys Med Biol 23(3), 1978. *84, 85, 90*

van Battum, L.J., Huizenga, H., *On the initial angular variances of clinical electron beams*, Phys Med Biol 44(11), 1999. *56, 98, 99, 100*

van Battum, L.J., van der Zee, W., Huizenga, H., *Scattering from applicators in clinical electron beams,* Phys Med Biol 48(15), 2003. *99, 100*

Van Dyk, J. et al., *Commissioning and quality assurance of treatment planning computers*, Int J Radiation Oncology Biol Phys 26, 1993. *64, 78*

Van Dyk, Jacob, editor, *The Modern Technology of Radiation Oncology*, Chapter 11, Medical Physics Publishing, Madison, WI, 1999. *6, 7, 8, 9, 10, 11.*

Varian, *CadPlan manual: External beam modelling physics v 6.0*, 1999. *52, 53, 54, 55, 58, 60, 61, 92, 99*

Vinceller, S., *Validation du système de planification de traitement THERAPLAN Plus pour des faisceaux d'électrons,* mémoire de recherche, maîtrise, Université Paul Sabatier, Toulouse, 1999. *112*

Wellhöfer Dosimetrie, *IC10 chambers*, serial numbers : 2073, 2217. *65*

Wellhöfer Dosimetrie, *WP700, CU 500 E electrometer. 65*

Wu, A., Kalend, A., Zickler, R.D., Sternick, E.S., *Comments on the method of energy determination for electron beams in the TG-21 protocol*, Med Phys 11(6), p. 871-874, 1984. *19*

Yu, C.X., Ge, W.S., Wong, J.W., *A multiray model for calculating electron pencil beam distribution*, Med Phys 15(5), 1988. *129*

Zhu, T.C., Das, I.J., Bjarngard, B.E., *Characteristics of bremsstrahlung in electron beams*, Med Phys 28(7), 2001. *59, 60*